Max-Planck-Institut
für Meteorologie

MAX-PLANCK-GESELLSCHAFT

International Max Planck Research School
on Earth System Modelling

Snowball Earth – Initiation and Hadley Cell Dynamics

Aiko Voigt

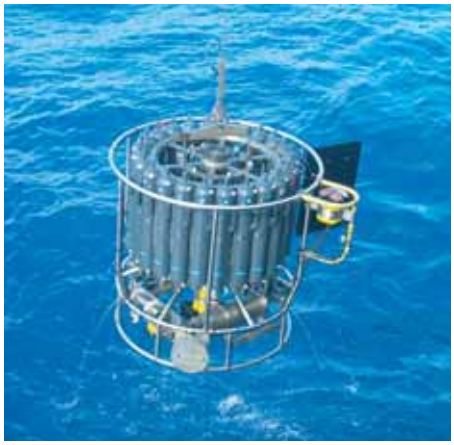

Berichte zur Erdsystemforschung 83/2010

Reports on Earth System Science

Hinweis

Die Berichte zur Erdsystemforschung werden vom Max-Planck-Institut für Meteorologie in Hamburg in unregelmäßiger Abfolge herausgegeben.

Sie enthalten wissenschaftliche und technische Beiträge, inklusive Dissertationen.

Die Beiträge geben nicht notwendigerweise die Auffassung des Instituts wieder.

Die "Berichte zur Erdsystemforschung" führen die vorherigen Reihen "Reports" und "Examensarbeiten" weiter.

Notice

The Reports on Earth System Science are published by the Max Planck Institute for Meteorology in Hamburg. They appear in irregular intervals.

They contain scientific and technical contributions, including Ph. D. theses.

The Reports do not necessarily reflect the opinion of the Institute.

The "Reports on Earth System Science" continue the former "Reports" and "Examensarbeiten" of the Max Planck Institute.

Anschrift / Address

Max-Planck-Institut für Meteorologie
Bundesstrasse 53
20146 Hamburg
Deutschland

Tel.: +49-(0)40-4 11 73-0
Fax: +49-(0)40-4 11 73-298
Web: www.mpimet.mpg.de

Layout:

Bettina Diallo, PR & Grafik

Titelfotos:
vorne:
Christian Klepp - Jochem Marotzke - Christian Klepp
hinten:
Clotilde Dubois - Christian Klepp - Katsumasa Tanaka

Berichte zur Erdsystemforschung 83/2010

Snowball Earth – Initiation and Hadley Cell Dynamics

Aiko Voigt

aus Berlin

Hamburg 2010

Reports on Earth System Science 83/2010

ISSN 1614-1199

Aiko Voigt
Max-Planck-Institut für Meteorologie
Bundesstrasse 53
20146 Hamburg
Germany

Als Dissertation angenommen
vom Department Geowissenschaften der Universität Hamburg

auf Grund der Gutachten von
Prof. Dr. Jochem Marotzke
und
Dr. Erich Roeckner

Hamburg, den 9. Juli 2010
Prof. Dr. Jürgen Oßenbrügge
Leiter des Departments für Geowissenschaften

ISSN 1614-1199

Snowball Earth – Initiation and Hadley Cell Dynamics

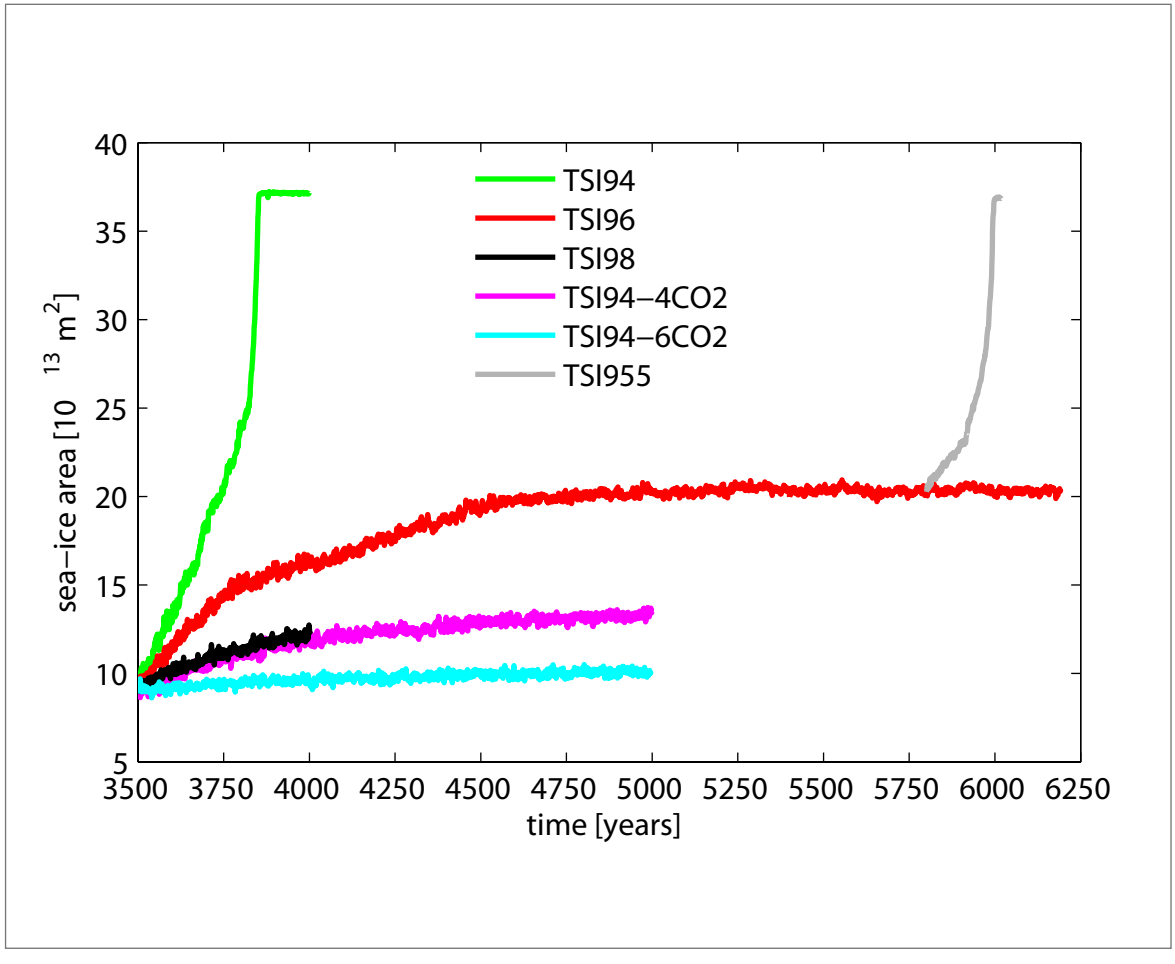

Aiko Voigt

Hamburg 2010

Abstract

I use climate model simulations to investigate the initiation of a Snowball Earth for present-day as well as Marinoan ($\sim$ 635 million years before present) surface boundary conditions, and to study the dynamics of the Hadley cell in a Snowball Earth atmosphere.

Using the coupled atmosphere-ocean general circulation model ECHAM5/MPI-OM in a present-day setup, I find that the modern Snowball Earth bifurcation point is between 91 and 94% of the present-day total solar irradiance (TSI) when atmospheric carbon dioxide is set to its pre-industrial level. The Snowball Earth bifurcation point as well as the transition times are well reproduced by a zero-dimensional energy balance model of the global-mean ocean potential temperature. During the transition, the asymmetric distribution of continents between the Northern and Southern Hemispheres causes heat transports toward the more water-covered Southern Hemisphere. Moreover, stable states can have no greater than 56.6% sea-ice cover.

Using the same model in a Marinoan setup, I show that changing the surface boundary conditions from present-day to Marinoan, which includes a shift of continents to low latitudes, induces a global mean cooling of 4.6 K. The Marinoan Snowball Earth bifurcation point for pre-industrial carbon dioxide is between 95.5 and 96% of the present-day total TSI, illustrating that low-latitude continents facilitate Snowball Earth initiation. A Snowball Earth for TSI reduced to 94% of its present-day value is prevented by quadrupling atmospheric carbon dioxide with respect to its pre-industrial level. The zero-dimensional energy balance model of global-mean ocean potential temperature again successfully predicts the Snowball Earth bifurcation point. States with sea-ice cover above 55% are unstable, akin to what I find for the present-day setup. This shows that ECHAM5/MPI-OM does not exhibit stable states with near-complete sea-ice cover but open equatorial waters. In summary, my results rebut previous conclusions that Snowball Earth initiation would require "extreme" forcings.

Using the atmosphere general circulation model ECHAM5, I investigate the tropical meridional circulation of a Snowball Earth atmosphere. I find that the dynamics of the Snowball Earth Hadley cell differ substantially from the dynamics of the present-day Hadley cell. In the upper branch of the Snowball Earth Hadley cell, mean meridional advection of mean absolute vorticity is not only balanced by eddy momentum flux divergence but also by vertical diffusion. Vertical diffusion also contributes to the meridional momentum balance as it decelerates the Hadley cell by downgradient momentum mixing between its upper and lower branches. I conclude that neither axisymmetric Hadley cell models based on angular momentum conservation nor eddy-permitting Hadley cell models that neglect vertical diffusion of momentum are applicable to a Snowball Earth

atmosphere since both assume an inviscid upper Hadley cell branch. Because vertical diffusion is important for the Hadley cell of a virtually dry Snowball Earth atmosphere, dry atmospheres in general should not be considered as a-priori simpler testcases for Hadley cell theories than moist atmospheres.

Contents

Chapter 1

Introduction

1.1 Setting the scene

Today's Earth comes as a comfortable place in the universe with moderate temperatures and liquid water at the surface, the latter being vital to the existence of life on Earth as we know it. Despite repeated excursions to warmer and colder climates, these conditions have prevailed for longer than the last 500 million years. Nevertheless, if we look only a bit further back in Earth's history, to the Neoproterozoic (1000 - 542 million years before present, Ma), we encounter evidence that Earth might have spent millions of years in a fundamentally different climate state (Kirschvink 1992; Hoffman et al. 1998; Hoffman and Schrag 2002). In this state, surface temperatures would be far below freezing even at the equator, implying that hardly any liquid surface water would be present, and oceans would be completely covered by sea ice. Earth would appear as a white planet from space, which is why this state is commonly dubbed "Snowball Earth."

To arrive at the Snowball Earth hypothesis requires one to combine geology and climate physics. On the one hand, glacial deposits strongly support the existence of wide-spread sea-level land glaciers in the tropics during two Neoproterozoic periods, the Sturtian ($\sim$ 710 Ma) and the Marinoan ($\sim$ 635 Ma) (Evans 2000; Trindade and Macouin 2007; Macdonald et al. 2010). On the other hand, simple enery balance models (Budyko 1969; Sellers 1969) suggest that once ice passes 30 degrees latitude, a runaway ice-albedo feedback leads to global ice cover. Kirschvink (1992) combined both pieces and came up with the idea that low-latitude glaciers by virtue of the runaway ice-albedo feedback require the entire Earth to be in deep freeze, the Snowball Earth.

In its complete form, the Snowball Earth hypothesis encompasses Snowball Earth initiation triggered by a drawdown of atmospheric greenhouse gases, residence in deep freeze for millions of years with slow but continous build-up of atmospheric carbon dioxide, and rapid deglaciation by massive carbon dioxide levels followed by a super-greenhouse. While the geological community continues a passionate debate whether the sedimentary record is compatible with the Snowball Earth hypothesis, the latter has also stimulated climate modellers to investigate its compatibility with climate physics.

This task clearly calls for models that are far more complex and comprehensive than the energy balance models that Kirshvink relied on. It is commonly accepted that Earth exhibits both the present-day like climate with only little sea-ice cover and the Snowball Earth climate with global sea-ice cover for present-day total solar irradiance (Marotzke and Botzet 2007). The role of climate modelling is hence to investigate if Snowball Earth initiation as well as Snowball Earth deglaciation are possible for values of total solar irradiance and/or atmospheric carbon dioxide that one thinks have prevailed during the Sturtian and Marinoan Snowball periods. Deglaciation long seemed to be the more difficult problem of the two (Pierrehumbert 2005), but recent studies have shown that dust makes deglaciation possible at carbon dioxide levels compatible with proxy data (Abbot and Pierrehumbert 2010; Abbot and Halevy 2010; Le Hir et al. 2010). In the case of initiation, recent years have seen an increasing number of climate modelling studies concluding that completely frozen oceans require "extreme" forcings (Chandler and Sohl 2000; Poulsen et al. 2001; Poulsen 2003; Poulsen and Jacob 2004) that might be considered unrealistic for the Neoproterozoic. At the same time, Hyde et al. (2000) and Peltier et al. (2004) found so-called "Slushball Earth" solutions that permit tropical land glaciers and open equatorial water simultaneously. Despite severe limitations of this model, including the disregard of atmosphere and ocean dynamics, these solutions have been supported in an atmospheric general circulation model coupled to a slab ocean and prescribed full continental glaciation (Hyde et al. 2000; Baum and Crowley 2001). Moreover, Chandler and Sohl (2000) and Micheels and Montenari (2008) found, also using atmosphere general circulation models coupled to slab oceans, solutions with equatorial land masses below freezing in conjunction with almost but not completely frozen oceans. As a result, the apparent difficulties in freezing the entire ocean combined with the possibility that equatorial land glaciers might not require completely frozen oceans evoked the impression that the Snowball Earth hypothesis seems implausible from the perspective of climate modelling. As a consequence, attention shifted to the Slushball Earth hypothesis (Lubick 2002; Kaufman 2007; Kerr 2010). In this thesis, I revisit Snowball Earth initiation with the hitherto best climate model applied to this problem. This model includes all physics found to be essential for Snowball Earth initiation, namely ocean dynamics, sea-ice dynamics, and interactive clouds.

Apart from using climate models to test the plausibility of the Snowball Earth hypothesis, the Snowball Earth offers a potentially fruitful testbed for atmospheric dynamicists. Its atmosphere is characterized by cold temperatures, and as a consequence water is largely eliminated from the atmosphere. The influence of moisture on the large-scale circulation, an issue that without doubt ranks among the most challenging topics in atmospheric science today, is hence virtually removed. This turns the Snowball Earth into an example of a dry atmosphere As the challenge of atmospheric dynamics is not in ascertaining the underlying dynamical equations, which are essentially known, but in distilling the primal processes and in neglecting the others, a dry atmosphere is

commonly thought of as a convenient starting point if one seeks to develop theories for atmospheric dynamics.

One of the most prominent examples for this approach is the Hadley circulation, a synonym for the tropical overturning circulation in the troposphere (see Lorenz (1967) for a historic review, and Schneider (2006) for a summary of recent progress). Pioneered by Schneider (1977) and Held and Hou (1980), important understanding has been gained by considering axisymmetric atmospheres. Thanks to increasing access to computing resources and progress in atmospheric modelling, however, one now seems in good position to study Hadley cell dynamics including the effect of non-axisymmetric motions, i.e. eddies, over a wide range of external parameters that one believes ultimately should control Hadley cell strength and extent. Recent years have seen considerable progress in this direction (Walker and Schneider 2005, 2006), largely by using the idealized general circulation model introduced in Schneider and Walker (2006). This model does resolve the large-scale circulation but only crudely accounts for subgrid physical processes. It is therefore essential to verify these results in a general circulation model with comprehensive physics but, surprisingly, this has not been done yet. By studying the Hadley cell in a Snowball Earth atmosphere with a state-of-the-art general circulation model, we hope to take a first step towards closing this gap.

1.2 Thesis objective

My thesis aims at answering the following research questions brought up in the previous section.

1. Initiation of a Snowball Earth
I apply the atmosphere-ocean general circulation model ECHAM5/MPI-OM to tackle the following issues:

- How much reduction of radiative forcing, in particular how much reduction of total solar irradiance, is needed to trigger Snowball Earth initiation? How much increase of atmospheric carbon dioxide is needed to prevent a Snowball Earth?
- How does the climate system behave during the transition to a Snowball Earth? In particular, how do atmosphere and ocean heat transports change?
- How close can sea ice invade the tropics before global sea-ice cover is triggered?
- Is the location of continents important for Snowball Earth initiation?
- Can we use simpler models to understand certain aspects of Snowball Earth initiation?

2. Atmospheric dynamics of a Snowball Earth
Using the atmosphere general circulation model ECHAM5, I focus on:

- What characterizes the Hadley cell of a Snowball Earth atmosphere?
- How does this compare to dry Hadley cell theories?

1.3 Thesis outline

My thesis contains three chapters written in the style of journal publications. One chapter has already been published while the other two are currently being prepared for submission. As a consequence, they contain their own introduction, model description, and conclusions, and can be read largely on their own. Two chapters are devoted to Snowball Earth initiation for present-day (Chapter 2) and Marinoan surface boundary conditions (Chapter 3), one chapter to the Snowball Earth Hadley cell (Chapter 4).

- **Chapter 2** investigates the sensitivity of the present-day climate to abrupt reductions of total solar irradiance. I estimate the transition time to a modern Snowball Earth and the Snowball Earth bifurcation point. Both are compared to a zero-dimensional energy balance of global-mean ocean potential temperature. I moreover analyze atmosphere and ocean heat transports during the entire transition from the present-day climate to a Snowball Earth and study how close sea ice can invade the tropics before the climate system becomes unstable. This chapter has been published in *Climate Dynamics*[1], and is reproduced here with editorial adjustments.

- In **Chapter 3**, I study if the location of continents influences what I found in **Chapter 2**. To this end, I change the surface boundary conditions to be representative of the Marinoan period, which includes a shift of continents to low latitudes, and generate a Marinoan control climate for present-day total solar irradiance and pre-industrial greenhouse gas concentrations using the same model as in Chapter 2. The climatic consequences of the change in surface boundary conditions are quantified by means of a one-dimensional energy balance model of zonal mean surface temperature. I reinvestigate the Snowball Earth bifurcation point and maximum stable sea-ice cover for the Marinoan setup. This allows me to contribute to the debate if a Snowball Earth hypothesis is compliant with the current knowledge of climate modelling. This chapter is in preparation for submission to *Journal of Geophysical Research*[2].

[1] Voigt, A. and J. Marotzke, 2009: The transition from the present-day climate to a modern Snowball Earth. *Clim. Dyn.*, doi:0.1007/s00382-009-0633-5.
[2] Voigt, A., D. S. Abbot, R. T. Pierrehumbert, and J. Marotzke, 2010: Initiation of a Marinoan

- **Chapter 4** deals with the dynamics of a Snowball Earth Hadley cell. I analyze the zonal and meridional momentum balances and investigate the role of vertical momentum diffusion for the Hadley cell using thought experiments and simulations. I compare my results to Hadley cell theories and discuss the implications of my simulations on the latter. This chapter is in preparation for submission to *Journal of Atmospheric Sciences*[3].

The thesis closes with a summary of my main findings in **Chapter 5**, in which I also propose directions of future research.

Snowball Earth in a state-of-the-art atmosphere-ocean general circulation model, *J. Geophys. Res.*, in preparation.

[3]Voigt, A., I. M. Held, and J. Marotzke, 2010: Equinox Hadley cell dynamics in a Snowball Earth atmosphere, *J. Atmos. Sci.*, in preparation.

Chapter 2

The transition from the present-day climate to a modern Snowball Earth

We use the coupled atmosphere-ocean general circulation model ECHAM5/MPI-OM to investigate the transition from the present-day climate to a modern Snowball Earth, defined as the Earth in modern geography with complete sea-ice cover. Starting from the present-day climate and applying an abrupt decrease of total solar irradiance (TSI) we find that the critical TSI marking the Snowball Earth bifurcation point is between 91 and 94% of the present-day TSI. The Snowball Earth bifurcation point as well as the transition times are well reproduced by a zero-dimensional energy balance model of the mean ocean potential temperature. During the transition, the asymmetric distribution of continents between the Northern and Southern Hemispheres causes heat transports toward the more water-covered Southern Hemisphere. This is accompanied by an intensification of the southern Hadley cell and the wind-driven subtropical ocean cells by a factor of 4. If we set back TSI to 100% shortly before the transition to a modern Snowball Earth is completed, a narrow band of open equatorial water is sufficient for rapid melting. This implies that for 100% TSI the point of unstoppable glaciation separating partial from complete sea-ice cover is much closer to complete sea-ice cover than in classical energy balance models. Stable states can have no greater than 56.6% sea-ice cover implying that ECHAM5/MPI-OM does not exhibit stable states with near-complete sea-ice cover but open equatorial waters.

2.1 Introduction

Earth's climate can exhibit at least two entirely different modes as suggested by climate models (Budyko 1969; Sellers 1969; Poulsen and Jacob 2004; Marotzke and Botzet 2007). One is the present-day climate with ice-cover only in the polar regions, the second is the so-called Snowball Earth climate with completely sea-ice covered oceans, potentially accompanied by glaciers on land. Below a certain level of atmospheric carbon dioxide or total solar irradiance (TSI), respectively, the present-day like mode disappears and the Snowball Earth mode is the only stable equilibrium (Budyko 1969;

Sellers 1969). We will refer to this critical threshold as the Snowball Earth bifurcation point. Here, we use the state-of-the-art climate model ECHAM5/MPI-OM to study the transition from the present-day climate to a hypothetical modern Snowball Earth, which we define as the Earth in modern geography with complete sea-ice cover.

The Snowball Earth is of interest both from a geological as well as a climate modelling perspective. On the one hand, based on glacial deposits in Neoproterozoic ($\sim$ 750-550 Ma) rock sequences it has been argued that several Snowball Earth events might have occurred during Earth's history (Kirschvink 1992; Hoffman et al. 1998). On the other hand, the Snowball Earth challenges climate modellers to confront their models and understanding of the climate system with the extreme climate of a Snowball Earth. Indeed, the work of Budyko (1969) and Sellers (1969), who used one-dimensional energy balance models and a temperature-dependent albedo parametrization to show that the entire Earth might become ice-covered if TSI was decreased by a few percent, stimulated a whole series of Snowball Earth modelling studies using the whole hierarchy of climate models, ranging from energy balance models (e.g., Held and Suarez 1974; North 1975), over Earth system models of intermediate complexity (e.g., Stone and Yao 2004; Donnadieu et al. 2004b; Romanova et al. 2006; Lewis et al. 2007), and atmosphere general circulation models with simplified ocean models (e.g., Jenkins and Frakes 1998; Chandler and Sohl 2000), to fully coupled atmosphere-ocean general circulation models (e.g., Poulsen et al. 2001; Poulsen and Jacob 2004). Some studies even incorporated dynamic ice sheet models (Hyde et al. 2000; Crowley et al. 2001; Peltier et al. 2004). Most studies attempted to estimate the Snowball Earth bifurcation point of the applied climate model by simulating the equilibrium climates for reduced values of TSI (justified by the "faint young sun" phenomenon) and/or reduced levels of atmospheric carbon dioxide. Several studies addressed the importance of various elements of the climate system such as ocean dynamics (Poulsen et al. 2001), surface winds (Poulsen and Jacob 2004), sea-ice dynamics (Lewis et al. 2007), sea-ice glaciers (Goodman and Pierrehumbert 2003; Pollard and Kasting 2005), and clouds (Le Hir et al. 2007; Poulsen and Jacob 2004), including their representation in the models.

However, except for the work of Donnadieu et al. (2004b), who used an Earth system model of intermediate complexity, previous studies focussed on whether a distinct combination of reduction in TSI and atmospheric carbon dioxide triggered a Snowball Earth, and they did not attempt to model the entire transition between the present-day like mode and the Snowball Earth mode. Instead of initializing the models from the present-day like mode, initial ocean temperatures were chosen to reduce the time required to reach equilibrium (e.g., Poulsen and Jacob 2004). In contrast, we here start our simulations from the pre-industrial control climate of our climate model and apply an abrupt decrease of total solar irradiance or atmospheric CO_2 to trigger the transition to a modern Snowball Earth. We thereby follow the same experimental strategy as Marotzke and Botzet (2007), but we apply a wide range of TSI reductions instead

of a single reduction of TSI to 0.01% of its today's value. In this study, we assess the following three issues.

First, we estimate both the Snowball Earth bifurcation point of the climate model ECHAM5/MPI-OM and the time needed to complete the transition from the present-day climate to a Snowball Earth. To our knowledge, there is only one study, with a simple energy balance model climate model, that estimates the transition time after a time-dependent reduction of TSI by 30% (Walsh and Sellers 1993).

Second, we analyze the response of the atmosphere and ocean heat transports and mean meridional circulations during the transition, with a focus on the Hadley cell and the Atlantic meridional overturning circulation. We compare our findings to the study of Donnadieu et al. (2004b) and find important differences.

Third, we study the degree of sea-ice cover that guarantees an unstoppable glaciation. This allows us to assess which extent of open equatorial water is possible, that is, whether our climate model exhibits solutions with near-complete sea-ice cover but open equatorial waters.

The paper is organized as follows. Section 2 describes the climate model, and Sect. 3 the setup of the ECHAM5/MPI-OM simulations. Section 4 investigates the Snowball Earth bifurcation point. Section 5 presents a zero-dimensional energy balance model of the mean ocean potential temperature and compares the results of the climate model ECHAM5/MPI-OM with this zero-dimensional model. Section 6 analyzes the atmosphere and ocean meridional circulations and heat transports, followed in Sect. 7 by an investigation of the degree of sea-ice cover needed for an unstoppable glaciation. Section 8 gives a general discussion of the results, Sect. 9 follows with conclusions.

2.2 Model

We use the the Max Planck Institute for Meteorology coupled atmosphere-ocean general circulation model ECHAM5.3.02p2/MPI-OM-1.2.3p2 (labelled by ECHAM5/MPI-OM in the following). The atmosphere component ECHAM5 is the fifth generation of the ECHAM model series that originally evolved from the weather prediction model of the European Centre for Medium Range Weather Forecasts. The details of ECHAM5 are comprehensively described in Roeckner et al. (2003). ECHAM5 employs a dynamical spectral core with vorticity, divergence, temperature, and the logarithm of surface pressure being represented in the horizontal by a truncated series of spherical harmonics. In the vertical a hybrid sigma-pressure coordinate system is applied. The shortwave radiation scheme (Fouquart and Bonnel 1980) uses 4 spectral bands. For longwave radiation ECHAM5 employs the Rapid Radiative Transfer Model (RRTM) developed by Mlawer et al. (1997) with 16 spectral bands. ECHAM5 uses a stratiform cloud scheme including a cloud microphysical scheme and prognostic equations for the vapour, liquid, and ice phase, respectively. Snow at the surface and the inception of snow at

the canopy are modeled explicitly. Most important for our study is the treatment of surface albedo. The grid-mean surface albedo depends on a prescribed background albedo. Snow on land changes this background albedo according to the fractional snow cover of the grid cell. The fractional snow cover itself is a function of the snow depth measured in metres of water equivalent, but also of the orographic standard deviation so that sloping terrains require a larger snow depth than flat terrains to reach the same fractional snow cover. The albedo of snow on land depends on the land surface temperature and ranges from 0.3 at 0° C to 0.8 at or below −5° C. Moreover, the shielding effect of forests is accounted for in the surface albedo. In forest areas the surface albedo is further modified by snow cover on the canopy and the resulting canopy albedo.

The ocean component MPI-OM employs the primitive equations on an orthogonal curvilinear C-grid (Arakawa and Lamb 1977), with the North Pole shifted to Greenland to avoid a singularity at the geographical North Pole. The grid South Pole is located over Antarctica. In the vertical, the model employs unevenly spaced z-levels with the bottom topography being resolved by way of partial grid cells (Wolff et al. 1997). Technical details of MPI-OM can be found in Marsland et al. (2003). We here only give a short description of the embedded sea-ice model, which follows the dynamics of Hibler (Hibler 1979) while the thermodynamics are incorporated by a zero-layer Semtner model relating changes in sea-ice thickness to a balance of radiant, turbulent, and oceanic heat fluxes (Semtner 1976). The freezing point of sea water is fixed to −1.9° C independent of salinity. Snow on ice is explicitly modeled, including snow/ice transformation when the snow/ice interface sinks below the sea level because of snow loading. The effect of ice formation and melting is accounted for by assuming a sea-ice salinity of 5. The albedo of bare sea ice depends on the ice surface temperature and ranges from 0.55 at 0° C to 0.75 at or below −1° C. Snow on sea ice leads to a significant albedo increase: if the water equivalent of snow depth is larger than 0.01 m, the sea ice is treated as being snow-covered. The albedo of snow-covered sea ice depends on the snow surface temperature and ranges from 0.65 at 0° C to 0.8 at or below −1° C. Sea ice thickness is limited to about 8 m, 75% of the thickness of the top layer of MPI-OM, to avoid the problem of dry model levels.

The atmosphere model ECHAM5 is coupled to the ocean model MPI-OM via the OASIS3 coupler (Valcke et al. 2003) with a coupling time step of one day. The ocean passes the sea surface temperature, sea-ice concentration and thickness, snow depth on ice, and ocean surface velocities to the atmosphere. The atmosphere provides the wind stress, heat flux, freshwater flux including river runoff and glacier calving, and 10 m wind speed to the ocean model. In the presence of sea ice the fluxes are calculated separately for sea-ice covered and open water parts of the grid cells. No flux adjustments are applied.

ECHAM5/MPI-OM has been extensively and successfully evaluated against obser-

vations (Hagemann et al. 2004; Jungclaus et al. 2006; Roeckner et al. 2006; Wild and Roeckner 2006) and was used for the integrations for the fourth assessment report of the Intergovernmental Panel on Climate Change (Brasseur and Roeckner 2005; Bengtsson et al. 2006; Landerer et al. 2007). Here, we use the low-resolution version of ECHAM5/MPI-OM to perform long simulations of up to 1000 years length. The atmosphere component uses 19 vertical levels and has a horizontal resolution of T31 (~ 3.75 degrees). The ocean model uses 40 vertical levels and has a horizontal resolution varying between 30 km near Greenland and 390 km in the tropical Pacific.

In contrast to most Snowball Earth model simulations, the location of continents, the mountain topography and the ocean bathymetry are all kept at their present-day values. Orbital parameters have modern values. Ozone follows the 1980-1991 climatology of Fortuin and Kelder (1998). Vegetation is prescribed according to a present-day climatology with monthly varying vegetation cover and leaf area indices for each surface grid cell. Land glaciers are fixed to their present-day extent. While the choice of modern boundary conditions inhibits the simulation of a Neoproterozoic Snowball Earth, it enables us to start our simulations from the present-day control climate and hence to simulate the entire transition from the present-day climate to a modern Snowball Earth. Atmospheric greenhouse gases are kept at pre-industrial levels ($CO_2 = 286.2$ ppm, CH_4=805.6 ppb, N_2O=276.7 ppb, no cfc), except for one simulation where we set the atmospheric CO_2 concentration to 0.1% of its pre-industrial value, i.e., 0.2862 ppm. This will then be stated explicitly.

2.3 Setup of ECHAM5/MPI-OM simulations

We conduct two different sets of ECHAM5/MPI-OM simulations. In the first set, we estimate the Snowball Earth bifurcation point by starting from the present-day control climate of ECHAM5/MPI-OM (simulation CTRL with today's TSI, $TSI_0 = 1367\,Wm^{-2}$, and pre-industrial greenhouse gas levels) but decreasing TSI with respect to TSI_0. The model is run until it reaches a new equilibrium, which is either a modern Snowball Earth characterized by complete sea-ice cover or a climate with extended but not complete sea-ice cover. As a byproduct we also obtain the transition times to a modern Snowball Earth as a function of the reductions in TSI as well as the atmospheric and oceanic dynamics and heat transports during the entire transition. We also conduct one experiment where we keep TSI at its present-day value but reduce atmospheric CO_2 to 0.1% of its pre-industrial value (simulation noCO2). All simulations of this first set are summarised in Table 2.1.

In the second set of simulations, we investigate which degree of sea-ice cover guarantees an unstoppable glaciation. When the climate model is on the way to a modern Snowball Earth due to a decrease of TSI below the Snowball Earth bifurcation point, we increase TSI abruptly at different stages of sea-ice cover before the transition to a

Table 2.1: Summary of the first set of ECHAM5/MPI-OM simulations to study the response of the present-day climate to reductions in TSI. The applied total solar irradiance is given in percentage of the present-day value $1367\,\mathrm{Wm}^{-2}$, the atmospheric carbon dioxide concentrations in percentage of its pre-industrial level 286.2 ppm. SE abbreviates Snowball Earth.

simulation	TSI	CO_2	simulated years	result
CTRL	100%	100%	100	pre-industrial control simulation
TSI00	0.01%	100%	16	SE within 14 a
TSI25	25%	100%	24	SE within 20 a
TSI38	38%	100%	28	SE within 26 a
TSI44	44%	100%	31	SE within 31 a
TSI50	50%	100%	51	SE within 37 a
TSI75	75%	100%	151	SE within 109 a
TSI87	87%	100%	301	SE within 285 a
TSI91	91%	100%	501	SE within 480 a
TSI94	94%	100%	1000	sea-ice line at 40° N/S after 1000 a
noCO2	100%	0.1%	331	SE within 240 a

modern Snowball Earth is completed. This allows us to study the point of unstoppable glaciation that separates the present-day like states with partial sea-ice cover from Snowball Earth states with complete sea-ice cover. The different degrees of sea-ice cover are provided by simulation TSI91 (cf., Table 2.1). The simulations of the second set are summarised in Table 2.2, with the letter "R" indicating that these simulations are restarted from simulation TSI91 of the first set. Climate variables other than sea-ice cover, such as sea-ice thickness and mean ocean potential temperature, certainly also influence the response of the climate system to an increase of TSI. To account for this we also conduct two simulations where we set TSI back to 100% 1 and 2 years, respectively, before global sea-ice cover is completed in the simulation R2-TSI94. These two simulations marked by "RR" are included in Table 2.2.

2.4 Snowball Earth bifurcation point and transition time

We now describe the response of sea-ice cover to an abrupt decrease of total solar irradiance (cf., Fig. 2.1 and Table 2.1). Setting TSI close to zero triggers global sea-ice cover within 14 years. All TSI values smaller than or equal to 91% TSI_0 lead to a modern Snowball Earth, but the transition time increases with TSI coming closer to

Table 2.2: Summary of the second set of ECHAM5/MPI-OM to investigate the point of unstoppable glaciation. The applied total solar irradiance is given in percentage of the present-day value 1367 Wm^{-2}, sea-ice cover in percentage of the global ocean area. All simulations use the pre-industrial concentration of carbon dioxide. SE abbreviates Snowball Earth.

simulation	TSI	restart from	sea-ice cover at restart (Dec. mean)	sim. years	result
R1-TSI100	100%	TSI91, year 478	87.7%	72	melting
R2-TSI94	94%	TSI91, year 460	56.6%	400	SE within 393 a
R3-TSI94	94%	TSI91, year 340	34.1%	100	melting
R4-TSI93	93%	TSI91, year 460	56.6%	60	SE within 52 a
RR1-TSI100	100%	R2-TSI94, year 850	81.7%	60	melting
RR2-TSI100	100%	R2-TSI94, year 851	87.7%	20	SE within 2 a

TSI_0. For example, decreasing TSI to 50% leads to a modern Snowball Earth within 37 years, decreasing TSI to 75% leads to a modern Snowball Earth within 109 years, and decreasing TSI to 91% leads to a modern Snowball Earth within 480 years. The increase in global sea-ice cover accelerates strongly in time. In the simulation with 91% TSI_0, for example, freezing of the last 50% of the ocean only takes 45 years whereas freezing of the first 50% takes 435 years. Note that a modern Snowball Earth is also obtained by keeping TSI at 100% TSI_0 but setting the atmospheric CO_2 concentration to 0.1% of its pre-industrial level. The transition time for this virtually CO_2-free atmosphere is 240 years and hence between the transition times for TSI set to 75% and 87% TSI_0 with the atmospheric CO_2 kept at 100%.

In contrast, a reduction of TSI to 94% TSI_0 does not lead to global sea-ice cover within 1000 years, but the sea-ice line shifts to 40° N/S with a very slow trend to increase. Given that 91% TSI_0 triggers a modern Snowball Earth but 94% does not, we find that the Snowball Earth bifurcation point in ECHAM5/MPI-OM is between 91% and 94% of the present-day total solar irradiance TSI_0.

Immediately after the reduction of TSI sea ice in the Southern Hemisphere decreases while the Northern Hemisphere sea ice does not show any initial dip. For TSI reductions below or equal to 50% TSI_0, sea ice then grows faster in the Northern Hemisphere than in the Southern Hemisphere due to a deeper ocean bathymetry in the Southern Hemisphere. In contrast, for TSI reductions between 75% and 91% TSI_0, sea ice then grows faster in the Southern Hemisphere than in the Northern Hemisphere (not shown). An explanation for this will be given in Sect. 2.8. The Atlantic freezes over faster than

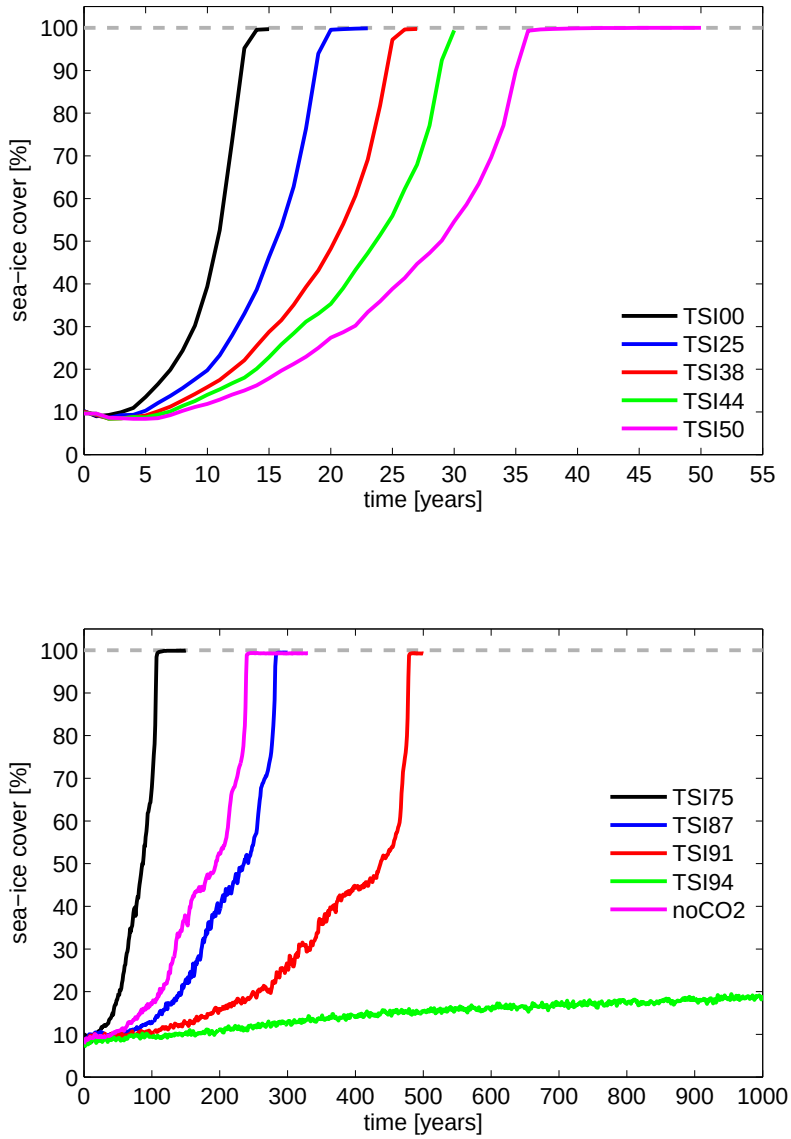

Figure 2.1: Time evolution of sea-ice cover in percentage of global ocean area as a response to an abrupt decrease of TSI to 0.01% to 50% of its present-day value TSI_0 (upper panel) and 75% to 94% of the present-day TSI_0 (lower panel). The applied TSI value in percentage of the present-day TSI_0 is indicated by the last two digits in the simulation labels. The lower panel includes the simulation noCO2 for a virtually CO_2-free atmosphere. The dashed gray lines depict complete sea-ice cover and hence a Snowball Earth.

the Pacific, with the time lag increasing from 3 months for the simulation TSI00 to 10 years for the simulation TSI91. Sea ice quickly becomes covered with snow, causing an albedo increase compared to bare sea ice by up to 0.1 in all simulations. In contrast, the formation of snow on land depends strongly on the TSI reduction. For simulations with drastic TSI reductions and hence shorter transition times, land snow cover is more spatially homogeneous but reaches lower maximum values. For example, land snow cover at the end of simulation TSI00 exceeds 0.2 m water equivalent everywhere except in the the tropical regions of Africa, South America and China, whereas at the end of simulation TSI91, most land areas show no or only little snow cover (below 0.05 m water equivalent), and heavy snow cover of water equivalents of 1 m or more is restricted to the Himalaya, the Rocky Mountains, the Andes, and tropical Africa.

We now analyze the role of clouds and water vapor during the transition to a modern Snowball Earth as modelled in simulation TSI91. In the case of longwave radiation we can disentangle the radiative effect of clouds from the effect of water vapor by means of the all-sky and clear-sky radiation fluxes at the top of the atmosphere. These are simultaneously calculated in ECHAM5. During the transition the effective surface emissivity ϵ, defined as the ratio of outgoing all-sky longwave radiation at the top of atmosphere and the upward longwave radiation emitted by the Earth's surface, increases from 0.6 to 0.86, meaning a strong decline of the greenhouse effect, $g = 1 - \epsilon$, with the cooling of the Earth. The longwave effect of water vapour ($\epsilon_{\text{clearsky}}$) can be disentangled from the effect of clouds (ϵ_{clouds}) by

$$\epsilon = \epsilon_{\text{clearsky}} + \epsilon_{\text{clouds}} = \text{LW}_{\text{TOA}}^{\text{allsky}} / \text{LW}_{\uparrow,\text{surface}} \tag{2.1}$$

with

$$\epsilon_{\text{clearsky}} = \text{LW}_{\text{TOA}}^{\text{clearsky}} / \text{LW}_{\uparrow,\text{surface}}. \tag{2.2}$$

Here, LW_{TOA} denotes the globally averaged annual longwave radiation at the top of the atmosphere with the superscripts marking the all-sky and the clear-sky fluxes. $\text{LW}_{\uparrow,\text{surface}}$ labels the globally averaged annual upward longwave radiation at the Earth's surface. Fig. 2.2 shows that the effect of clouds on the effective surface emissivity stays constant during the entire transition to a modern Snowball Earth. The increase in the effective surface emissivity is indeed entirely caused by the increase in the clear-sky surface emissivity itself resulting from the decrease in atmospheric water vapour content (see Fig. 2.3). We also find the logarithmic dependence of the clear-sky greenhouse effect $g_{\text{clearsky}} = 1 - \epsilon_{\text{clearsky}}$ on the atmospheric water vapour content (Raval and Ramanathan 1989) over the whole range of water vapour content from 0.3 to 18 kgm^{-2} (not shown).

In the case of shortwave radiation the effect of clouds can be characterized by the difference of the all-sky planetary albedo $\alpha_{\text{allsky}} = \text{SW}_{\uparrow,\text{TOA}}^{\text{allsky}} / \text{SW}_{\downarrow,\text{TOA}}$ and the clear-sky planetary albedo $\alpha_{\text{clearsky}} = \text{SW}_{\uparrow,\text{TOA}}^{\text{clearsky}} / \text{SW}_{\downarrow,\text{TOA}}$, with the indices having the same meaning as in (2.1) and (2.2). Note that this difference is not equal to the albedo of

clouds (Pierrehumbert 2002) although it quantifies the effect of clouds on the planetary albedo. During the transition to a modern Snowball Earth, clouds become less and less important for the reflection of shortwave radiation (see Fig. 2.4). This is a consequence of the strong increase in surface albedo with the advancement of sea ice, making the reflection of shortwave radiation by clouds dispensable.

In terms of cloud radiative forcing CRF = $(\mathrm{LW}_{\mathrm{TOA}}^{\mathrm{clearsky}} - \mathrm{LW}_{\mathrm{TOA}}^{\mathrm{allsky}}) + (\mathrm{SW}_{\mathrm{TOA}}^{\mathrm{allsky}} - \mathrm{SW}_{\mathrm{TOA}}^{\mathrm{clearsky}})$, clouds cool the Earth during the entire transition by $-18\,\mathrm{Wm}^{-2}$ during the first 300 years (see Fig. 2.5). From year 300 to the completion of sea-ice cover in year 480, the cloud radiative forcing declines to zero in year 480. The forcing over land increases from -10 Wm^{-2} during the first 190 years to 5 Wm^{-2} at year 480 when the transition to a Snowball Earth is completed. Over sea-ice free ocean areas, clouds have a large cooling effect that even increases during the transition. Shortly before sea-ice cover is complete the cloud forcing over open ocean areas declines to zero as no year-round sea-ice free ocean areas are left at this point. Ocean areas with more than 95% annual mean sea-ice cover experience an almost zero cloud radiative forcing. In contrast to the expectation of a small shortwave contribution but presumably still significant longwave contribution over sea ice, clouds over sea ice only exert a rather weak longwave forcing of about 8 Wm^{-2} in ECHAM5/MPI-OM. Also note that after the transition, the cloud radiative forcing is slightly negative (-0.5 Wm^{-2}) due to negative cloud radiative forcing over sea ice.

The analysis of the ocean heat flux for simulations with TSI set to 87%, 91%, and 94% TSI_0 shows a strong ocean heat loss directly after the TSI decrease (see Fig. 2.6). Then, the ocean continues losing heat in all three simulations, but the rate of ocean heat loss decreases with time. For 87% TSI_0 it is still larger than 2 PW after 220 years. For 91% TSI_0, the ocean heat loss almost stabilizes near 1.5 PW, and its 15-year running mean never falls below 1 PW. The final freezing-over of the ocean is preceded by a strong pulse in ocean heat loss. In contrast, the simulation with 94% TSI_0 shows a monotonic decrease of ocean heat loss, which comes to close to zero after 1000 years.

The ocean eventually "decides" whether a given decrease of TSI triggers the transition to a modern Snowball Earth, since complete sea-ice cover requires not only the surface layers of the ocean to cool to close to the freezing point but also large parts of the underlying water column. For salinities greater than 24.7 the density maximum of sea water is at its freezing point and the formation of sea ice at the surface must therefore be preceded by convection due to stability reasons (e.g., Washington and Parkinson 2005). This cooling of the ocean to close to the freezing point of sea water before the accomplishment of complete sea-ice cover is also seen in ECHAM5/MPI-OM (Fig. 2.7). That the freezing point in MPI-OM does not depend on the salinity but is fixed to $-1.9°\mathrm{C}$ is not a problem for the above mechanism as the vast majority of ocean areas have salinities greater than 24.7.

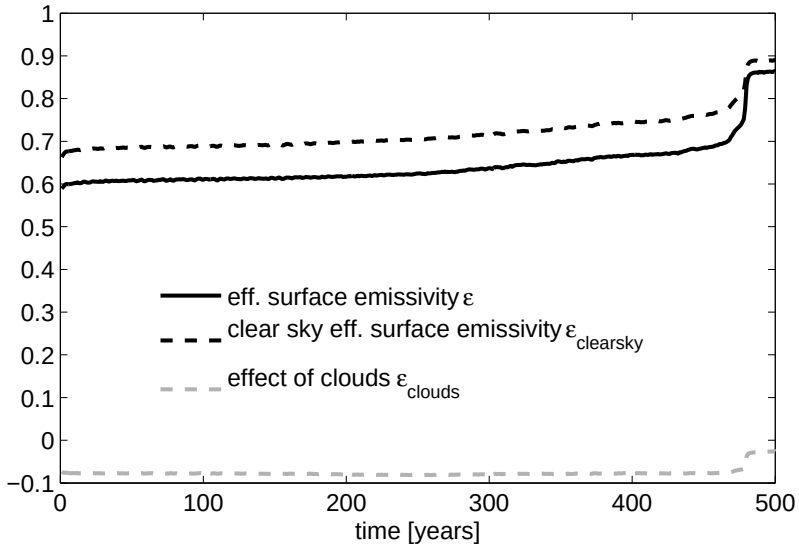

Figure 2.2: Time evolution of the effective surface emissivity ϵ (black solid), the clear-sky effective surface emissivity $\epsilon_{\text{clearsky}}$ (black dashed), and the effect of clouds (gray dashed) on the effective surface emissivity for a decrease of TSI to 91% of its present-day value (simulation TSI91).

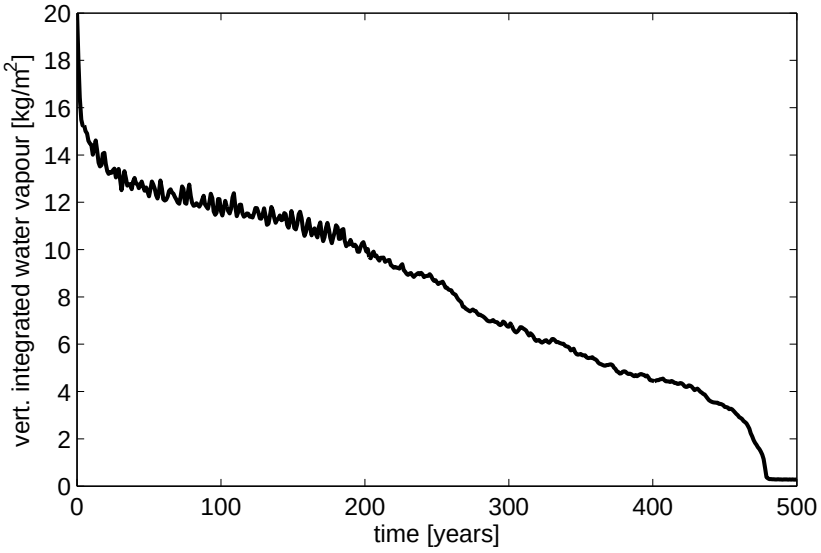

Figure 2.3: Time evolution of the vertically integrated atmospheric water vapour for a decrease of TSI to 91% of its present-day value (simulation TSI91). Sea-ice cover is completed by year 480.

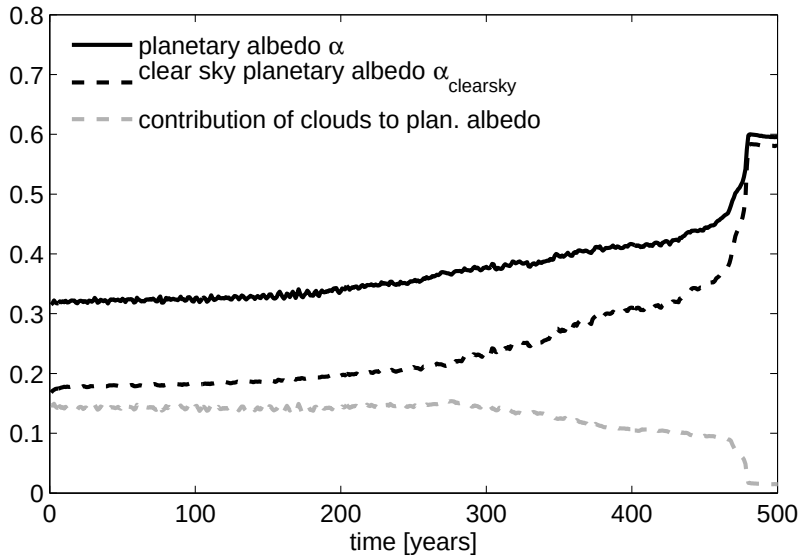

Figure 2.4: Time evolution of planetary albedo (black solid), clear-sky planetary albedo (black dashed), and the effect of clouds on the planetary albedo as characterized by the difference of the planetary albedo and the clear-sky planetary albedo (gray dashed), for a decrease of TSI to 91% of its present-day value (simulation TSI91).

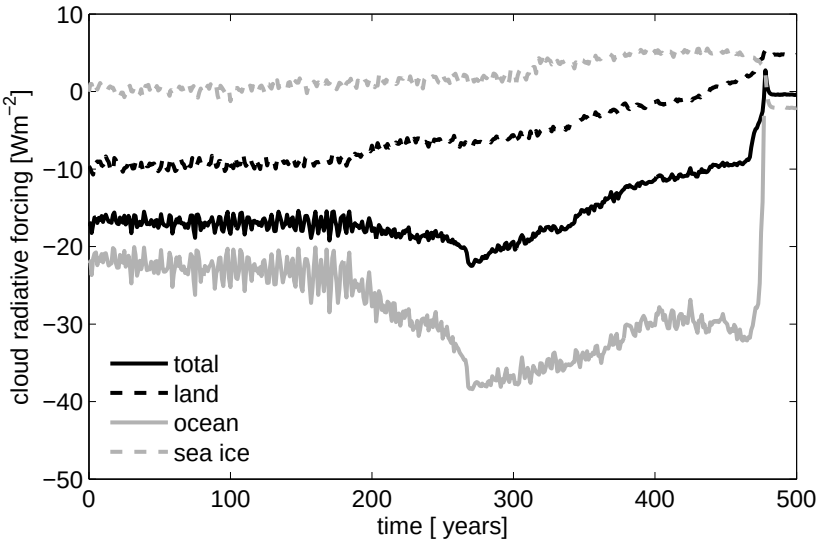

Figure 2.5: Time evolution of the cloud radiative forcing for a decrease of TSI to 91% of its present-day value (simulation TSI91). Sea-ice cover is completed by year 480. When calculating the individual contribution of land, ocean and sea-ice areas, we dismissed "mixed" land-ocean cells. For the cloud radiative forcing over ocean areas, we only considered ocean cells with zero annual mean sea-ice cover. For the cloud radiative forcing over sea-ice areas, we only considered ocean cells with annual mean sea-ice cover greater than 95%.

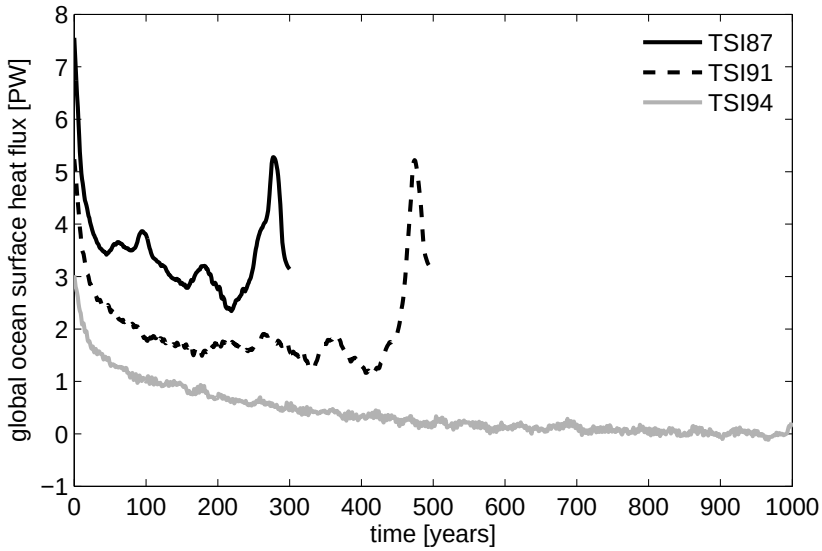

Figure 2.6: Time evolution of global ocean heat loss for reductions of TSI to 87% (black), 91% (black dashed) and 94% (grey) of the present-day TSI_0. Positive values correspond to heat loss of the ocean, negative values to heat gain. A 15-year running mean is applied.

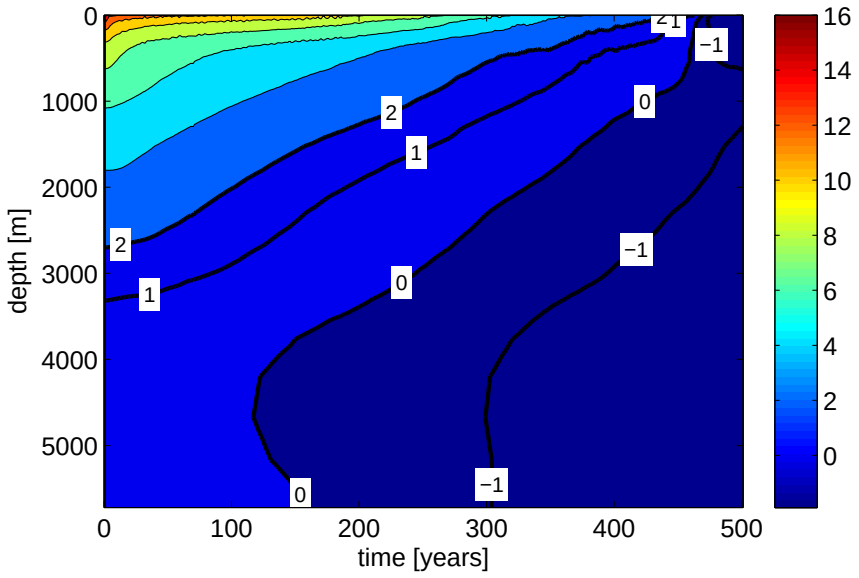

Figure 2.7: Time evolution of horizontally averaged global ocean potential temperature in ° C for a reduction of TSI to 91% of its present-day value (simulation TSI91). Contour intervals are 2° C for temperatures above 2° C and 1° C for temperatures below 2° C. The low-temperature region is highlighted with contour labels and thicker contour lines.

2.5 Comparison to a zero-dimensional energy balance model of mean ocean potential temperature

The ocean is by far the largest heat reservoir of the climate system and has to cool down to close to the freezing point before a modern Snowball Earth is possible. In the light of this outstanding role of the ocean, we devise a zero-dimensional energy balance model of the mean ocean potential temperature (shortly called energy balance model in the following). By modelling the response of the mean ocean potential temperature to a decrease in total solar irradiance, this energy balance model will allow us to estimate the transition time from the present-day climate to a modern Snowball Earth as well as the Snowball Earth bifurcation point.

We assume that the ocean is perfectly mixed in both the horizontal and the vertical directions. While this assumption is clearly daring for the present-day ocean, it becomes more and more reasonable as the Earth's climate approaches the Snowball Earth as described at the end of the preceding section. The energy balance model neglects the heat stored in the atmosphere and land components of the climate system.

In the energy balance model the heat flux at the ocean's surface is described by the (im)balance of shortwave and longwave radiation, and the mean ocean potential temperature (referred to as ocean temperature in the following), θ, consequently obeys the budget equation

$$c\frac{d\theta}{dt} = \frac{(1-\alpha)}{4}\mathrm{TSI} - \epsilon\sigma\theta^4, \tag{2.3}$$

with c denoting the specific heat capacity of the ocean per unit area. Based on the MPI-OM parameters for the specific heat capacity of sea water, the density of sea water, and the global ocean volume and surface area, we obtain $c = 1.53 \cdot 10^{10}\,\mathrm{JK^{-1}m^{-2}}$. The exact value of c is not at all crucial for the results of the energy balance model though it ensures that the two tuning parameters α and ϵ take reasonable values. The parameter α models the reflection of solar radiation by clouds and by the ocean's surface and hence can be thought of as the planetary albedo. The parameter ϵ can be thought of as the effective surface emissivity and hence the efficiency of ocean heat loss by longwave radiation.

We use this energy balance model to predict the time evolution of the ocean temperature θ after an abrupt decrease of TSI. The model is only valid for ocean temperatures above the freezing temperature of sea water $\theta_f = -1.9^\circ$ C. This is enough for our purposes here since we are only interested in the transition to a modern Snowball Earth, which in the energy balance model is defined by $\theta = \theta_f$. The temperature of the present-day ocean is diagnosed from the control simulation CTRL to be $\theta_{\mathrm{pd}} = 4.35^\circ$C and is used as the initial condition to (2.3). Requiring that the present-day ocean is an equilibrium solution of (2.3) for the present-day $\mathrm{TSI}_0 = 1367\ \mathrm{Wm^{-2}}$, the ratio of the

two tuning parameters α and ϵ is fixed to

$$\frac{(1-\alpha)}{\epsilon} = 4\sigma \frac{\theta_{\mathrm{pd}}^4}{\mathrm{TSI}_0} \simeq 0.9838. \tag{2.4}$$

The value of ϵ is determined by demanding that the energy balance model matches the transition time of 14 years found in the ECHAM5/MPI-OM simulation TSI00. In this case, the solar radiation term in (2.3) can be neglected, and in conjunction with the initial condition $\theta = \theta_{\mathrm{pd}}$ and the constraint $\theta = \theta_f$ for $t = 14$ years, we arrive at $\epsilon = 0.6736$. This fitted value of ϵ is taken to be constant for all TSI values. With (2.4) it follows that $\alpha = 0.3373$. In contrast to the energy balance models of Budyko and Sellers the albedo is held constant for all ocean temperatures between the freezing temperature of sea water and the present-day ocean temperature. Although we thus do not allow for an ice-albedo feedback in our energy balance model, this has the advantage that the estimate of the Snowball Earth bifurcation point gained with our energy balance model does not dependent on a chosen albedo parametrization as in the Budyko-Sellers models.

The fitted albedo of the energy balance model is close to the present-day planetary albedo, α_{pd}, which is estimated in the ECHAM5/MPI-OM control simulation CTRL to $\alpha_{\mathrm{pd}} = 0.326$. When comparing the effective surface emissivity of the energy balance model to the present-day effective surface emissivity ϵ_{pd} as modeled in the ECHAM5/MPI-OM control simulation CTRL, we need to include a form factor in ϵ_{pd} to incorporate that the sea surface temperature is larger than the vertically averaged mean ocean potential temperature used in the energy balance model to describe the energy loss by longwave radiation. With a present-day mean sea surface temperature of $\mathrm{SST}_{\mathrm{pd}} = 11.31°\mathrm{C}$, a present-day mean ocean potential temperature $\theta_{\mathrm{pd}} = 4.35°\mathrm{C}$, and a present-day mean effective surface emissivity $\epsilon_{\mathrm{pd}} = 0.583$ as estimated in the ECHAM5/MPI-OM control simulation CTRL, we arrive at a "corrected" value for the present-day effective surface emissivity of $\epsilon_{\mathrm{pd}}^{\mathrm{corr}} = \epsilon_{\mathrm{pd}}(\mathrm{SST}_{\mathrm{pd}}/\theta_{\mathrm{pd}})^4 = 0.644$ (with both $\mathrm{SST}_{\mathrm{pd}}$ and θ_{pd} given in Kelvin). As for the albedo the effective surface emissivity of the energy balance model is thus close to its present-day value though slightly larger.

With these choices for α and ϵ, we use the energy balance model to estimate the transition time to a Snowball Earth as a function of decrease in TSI. This is done by solving (2.3) with the initial condition $\theta = \theta_{\mathrm{pd}}$ and the final condition $\theta = \theta_f$. The resulting transition times are shown in Fig. 2.8 (gray line), which also includes the transition times found by the ECHAM5/MPI-OM simulations (black filled squares). The energy balance model is in good agreement with the ECHAM5/MPI-OM results for TSI values in the range of 0% to 50% TSI_0. This shows that TSI reductions to less than 50% are well described by radiative cooling of the ocean. In contrast, the energy balance model underestimates the transition times for the two TSI values 75% TSI_0 and 87% TSI_0. This underestimation is somewhat surprising since one would expect that

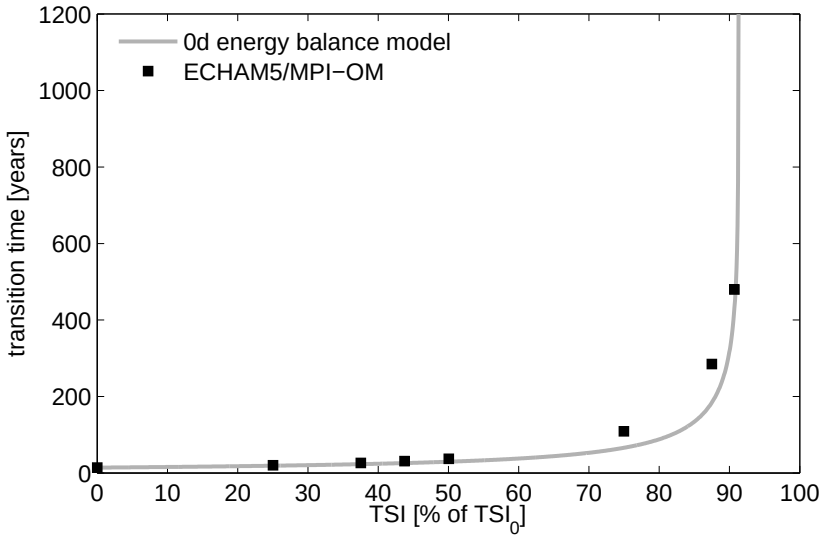

Figure 2.8: Transition time from the present-day climate to a modern Snowball Earth in dependence of TSI given in percentage of its present-day value. Black filled squares denote the results of ECHAM5/MPI-OM simulations, the gray line denotes the transition time as modelled by the zero-dimensional energy balance model of the mean ocean potential temperature.

neglecting the ice-albedo feedback should result in an overestimation of the transition times compared to the ECHAM5/MPI-OM simulations. However, the energy balance model does not only miss the positive ice-albedo feedback, but also other processes that potentially could retard the transition, and these processes are only modelled by the value for ϵ tuned to the ECHAM5/MPI-OM simulation TSI00. The underestimation of the transition times in this range of TSI values might therefore indicate that delaying mechanism such as ocean dynamics as suggested by Poulsen et al. (2001) come into play for less drastic TSI reductions. For 91% TSI_0 the energy balance model is again in agreement with the ECHAM5/MPI-OM simulations. We interpret this agreement for 91% TSI_0 as a zero net effect of neglecting delaying mechanisms as well as the ice-albedo feedback in our energy balance model.

The energy balance model predicts that for TSI greater than 91.3% TSI_0 the ocean temperature never falls below the freezing temperature of sea water. This is expressed by the transition times becoming infinite above 91.3% TSI_0 (see Fig. 2.8). Although the energy balance model (EBM) itself does not experience a bifurcation at 91.3% TSI_0, we interpret this value as the EBM estimate of the Snowball Earth bifurcation point. This estimate is consistent with ECHAM5/MPI-OM giving a range of 91% to 94% TSI_0. We stress that the EBM estimate of the Snowball Earth bifurcation point does not depend

on the individual values for α and ϵ, but only on their ratio in (2.4). On the one hand, this means that we could also tune α and ϵ to any ECHAM5/MPI-OM simulation with a TSI reduction below or equal to 91% TSI_0 without changing the EBM estimate of the Snowball Earth bifurcation point. On the other hand, if we chose a larger ratio, or equivalently a larger present-day ocean temperature θ_{pd}, the EBM estimate of the Snowball Earth bifurcation point would shift towards lower TSI. Therefore the present-day climate, represented in the energy balance model by the present-day ocean temperature, entirely controls the EBM estimate of the Snowball Earth bifurcation point through (2.4).

2.6 Atmosphere and ocean circulations and heat transports

We now study the atmosphere and ocean circulations both for a climate with extended but not complete sea-ice cover and for the entire transition period to a modern Snowball Earth. The focus will be on the Hadley cell in the atmosphere and the Atlantic meridional overturning circulation (AMOC). We also investigate atmosphere and ocean meridional heat transports and analyze how they are related to changes in the mean meridional circulations. For the atmosphere, we analyze the total advective heat transport and its decomposition in mean meridional and eddy transports. We use six-hourly instantaneous data and define the eddy terms as the deviation from the monthly and zonal mean. For the ocean, we report on the total ocean heat transport (calculated as the implied ocean heat transport based on monthly data of the heat and water fluxes at the ocean surface as well as monthly data of the ocean potential temperature) and the contribution of the meridional overturning circulation (calculated by monthly data of the horizontal velocity field and the ocean potential temperature). Moreover, we study the transport of latent heat due to sea-ice dynamics, which we calculate as the product of the transported sea-ice volume times the melting enthalpy of sea-ice of $320 \cdot 10^6\,\mathrm{Jm}^{-3}$.

We here analyze two simulations. First, we investigate the last 50 years of the simulation TSI94 as representative for an equilibrium climate with extended but not complete sea-ice cover. Second, we study the transient simulation TSI91 from the abrupt decrease of TSI to 91% until completion of sea-ice cover after 480 years.

We start with the analysis of the last 50 years of the simulation TSI94. The total advective atmospheric heat transport shown in Fig. 2.9 decreases in the Southern as well as the Northern Hemisphere with a decrease of the maximum heat transport around 35° N/S by 0.8 PW. This decrease is mainly due to a decrease of eddy transport around 35° N/S, which is caused by a decrease of eddy latent heat transport while the eddy dry static heat transport is virtually unchanged compared to the control simulation (not shown). The total heat transport by the mean meridional circulation changes very little, but this is a zero net effect of strong decreases in the magnitudes of the dry static heat transport and latent heat transport by the mean meridional circulation, which are

opposite to each other. We see a weakening of the Hadley cell in the Southern Hemisphere and a break-down of the Ferrel cell in the Northern Hemisphere (not shown); however, the primary reason for the decrease in advective atmospheric heat transport are not changes in the atmospheric circulation but the strong decrease of atmospheric water vapour content by 55% compared to CTRL.

Global ocean heat transport decreases in TSI94 throughout the Northern Hemisphere, but stays constant in the Southern Hemisphere subtropical region and even increases in Southern Hemisphere midlatitudes (see Fig. 2.10). These changes in total ocean heat transport are mainly due to changes in the ocean heat transport due to the meridional overturning circulation (MOC, Fig. 2.10). The gyre transport comes close to zero polewards of 40° N/50° S due to the expansion of sea ice and intensifies slightly around the equator. The hemisphere-dependent behaviour of total ocean heat transport can be traced back to the Atlantic while the total ocean heat transport in the Indo-Pacific Ocean shows a small decrease of its peak values around 15° N/S in both hemispheres. Indeed, the present-day asymmetry of the AMOC, which in CTRL leads to northward ocean heat transport even in the Southern Hemisphere, is much weaker at the end of the simulation TSI94, and we even see a slight southward heat transport in the Southern Hemisphere. The AMOC shows a North Atlantic Deep Water (NADW) cell shallower and weaker by 7 Sv. In contrast the Antarctic Bottom Water (AABW) cell strengthens by 6 Sv and now extends up to 2200 m instead of 2700 m in CTRL. In the surface layers the wind-driven subtropical cells increase by 8-10 Sv in both hemispheres. At the end of the simulation TSI94 sea-ice transport contributes about 0.2 PW to the meridional transport of heat at 50° N/60° S, which is five times more than its maximum in CTRL (see Fig. 2.11).

Simulation TSI91 accomplishes a modern Snowball Earth within 480 years. Total advective atmospheric heat transport initially decreases slightly in both hemispheres, then increases slowly in the Southern Hemisphere after 200 years (Fig. 2.12). After 280 years, the peak value of heat transport in the Southern Hemisphere starts to shift northwards. In contrast, the total advective atmospheric heat transport in the Northern Hemisphere continues to decline and hardly alters its meridional shape. This dominance of southward heat transport is due to large changes in the heat transport by the mean meridional circulation after year 300. At this moment the annual-mean heat transport by the mean meridional circulation resembles strongly the mean meridional heat transport during boreal summer (June, July, August) of CTRL. The changes in the heat transport by the mean meridional circulation are associated with substantial changes in the shape and magnitude of the Hadley cell. While the Hadley cell decreases in strength during the first 280 years in both hemispheres, its southern branch strongly intensifies after year 280 reaching a maximum strength of $41 \cdot 10^{10}\,\mathrm{kgs}^{-1}$ at year 467 and weakening shortly before the accomplishment of complete sea-ice cover (see Fig. 2.13). The eddy heat transport in TSI91 after 280 years exhibits a slight

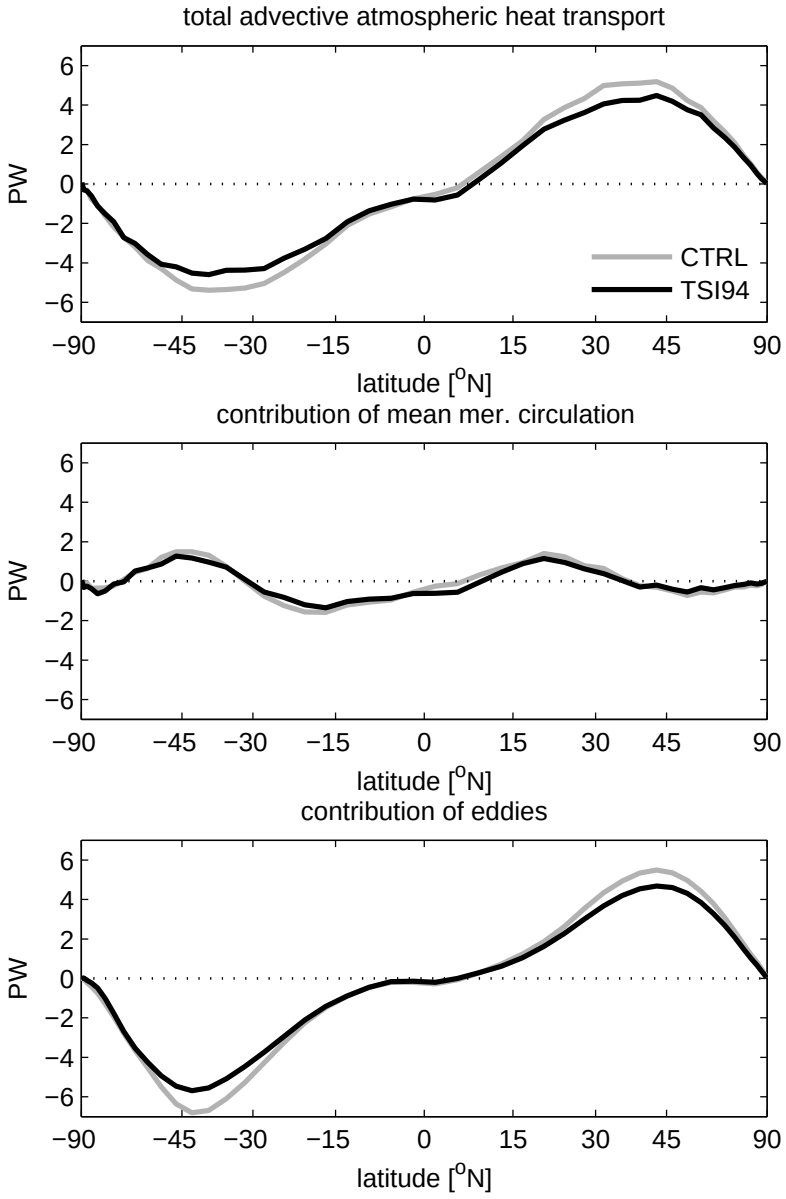

Figure 2.9: Total advective atmospheric heat transport (top), contribution of the mean meridional circulation (middle), and contribution of eddies (bottom); for the control simulation CTRL (gray) and averaged over the last 50 years of the simulation TSI94 (black).

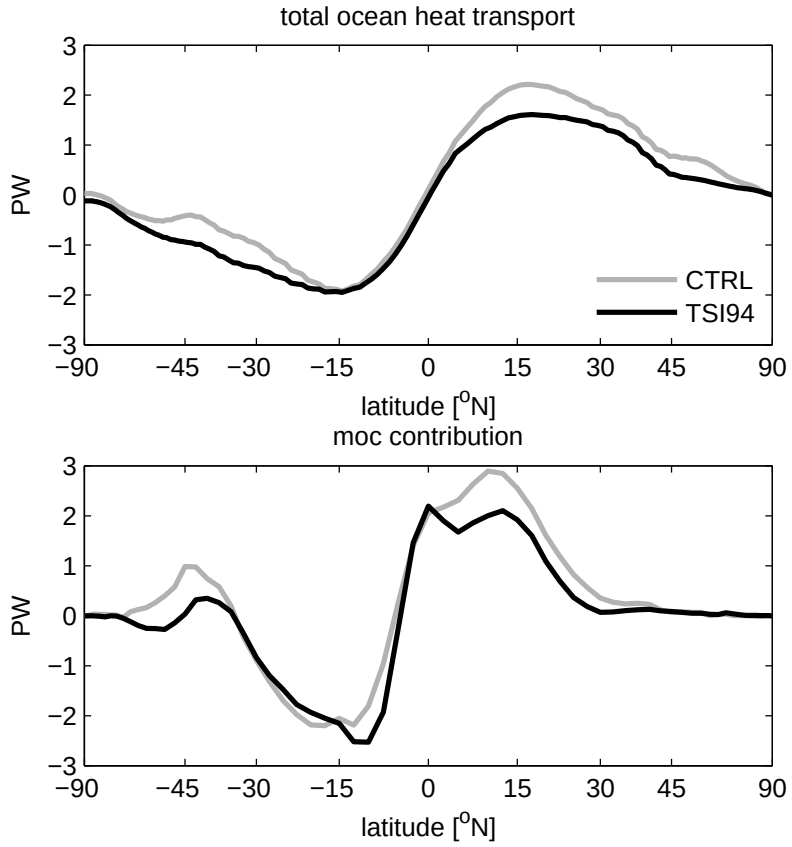

Figure 2.10: Total global ocean heat transport (top), and contribution of the meridional overturning circulation (bottom); for the control simulation CTRL (gray) and averaged over the last 50 years of the simulation TSI94 (black).

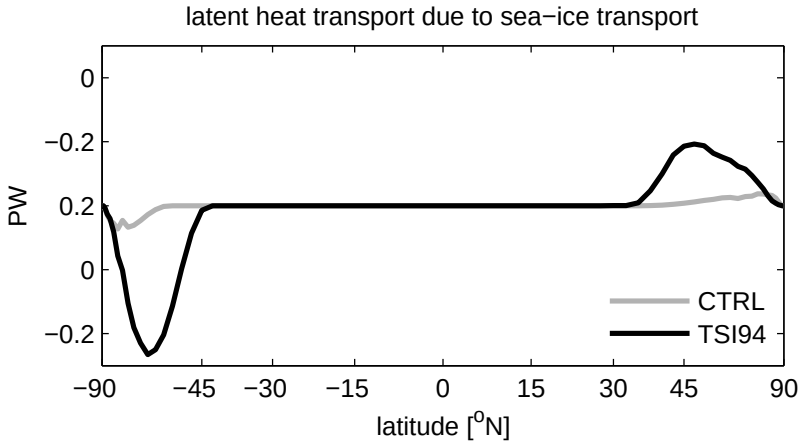

Figure 2.11: Global ocean latent heat transport due to sea-ice transport in the control simulation CTRL (gray) and averaged over the last 50 years of the simulation TSI94 (black).

increase in the Southern Hemisphere and a decrease in the Northern Hemisphere but hardly changes its meridional shape with the advancement of sea ice.

The total heat transport by the global ocean first increases after the abrupt decrease of TSI in TSI91 but shows a strengthening of southward heat transport in the Southern Hemisphere and a decrease of northward transport in the Northern Hemisphere after 200 years (see Fig. 2.14). This is also reflected in the contribution of the meridional overturning circulation showing a strong intensification of southward heat transport close to the equator after 250 years. The initial increase of northward heat transport in the Northern Hemisphere is related to an intensification of the NADW cell in the Atlantic. Fig. 2.15 illustrates the time evolution of the peak values of the NADW cell and the AABW cell, which we define as the maximum (NADW) and minimum (AABW) values of the meridional overturning below 600m, respectively. After the abrupt decrease of TSI, the NADW cell increases by 18 Sv in the first 50 years but then declines until the Atlantic becomes completely sea-ice covered in year 470. The AABW cell strengthens in the course of the simulation TSI91 until both cells decline after the completion of sea-ice cover in year 470 (upper panel of Fig. 2.15). The strength of the NADW and AABW cells are negatively correlated with a regime shift between year 290 and 312: the circulation changes from a strong NADW and weak AABW cell to a weak NADW and strong AABW cell (lower panel of Fig. 2.15). The regime shift in the NADW and AABW cells coincides with the increase of the southern branch of the Hadley cell. The wind-driven subtropical cells in the Atlantic do not show any immediate response to the abrupt decrease of TSI but slowly increase during the simulation and eventually are up to four times stronger than in CTRL (see Fig. 2.16). The strength of the clockwise northern cell and the anticlockwise southern cell are correlated although the southern cell intensifies by a factor of 4 while the northern cell only strengthens by a factor of less than two compared to CTRL. The regime shift from NADW to AABW as dominating AMOC cell is connected to the above-mentioned increase of southward ocean heat transport at this stage of the simulation TSI91. After 400 years the wind-driven subtropical cells in the Atlantic decline rapidly with the advancement of sea-ice to the tropical Atlantic. In the Indo-Pacific the subtropical cells similarly intensify during the simulation with the southern cell even strengthening by a factor of 6 compared to CTRL around year 450 (not shown).

Poleward latent heat transport by sea-ice transport increases significantly after 250 years and reaches a peak value of 1 PW in the Southern Hemisphere (see Fig. 2.17). However, the maximum sea-ice transport is not close to the equatorward edge of the sea-ice extent but centered around 40° S.

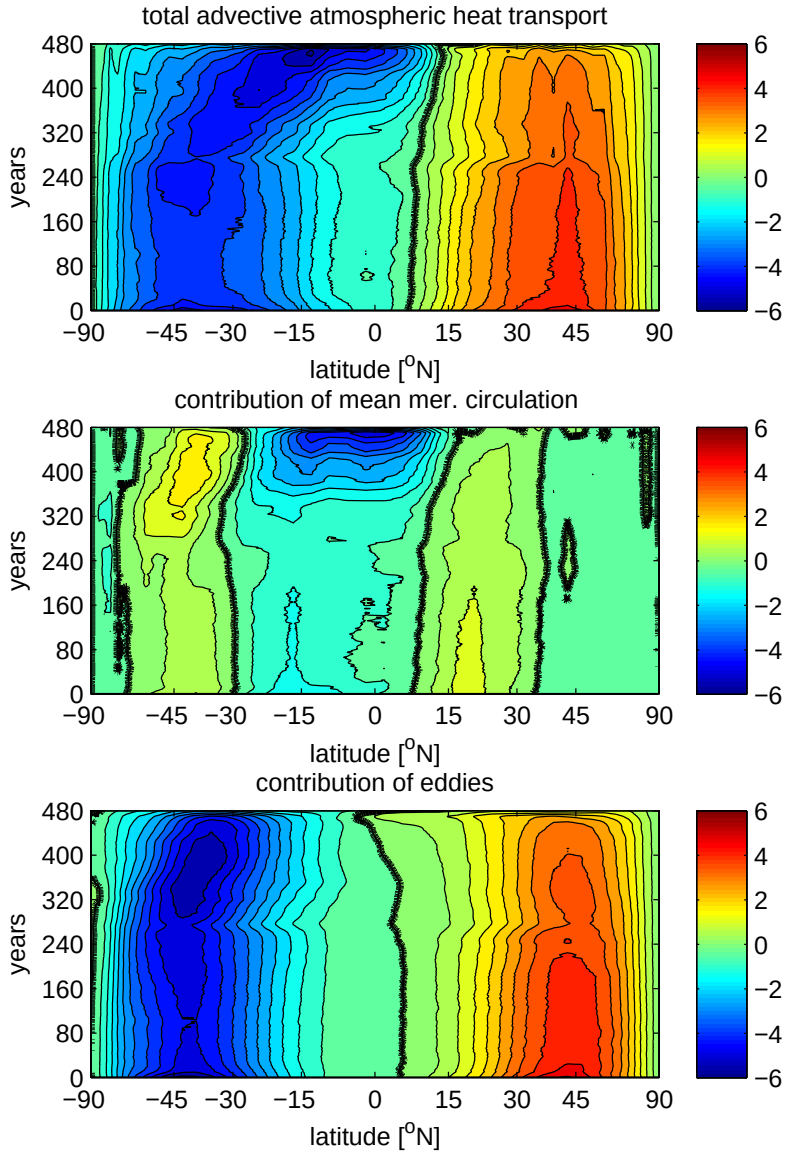

Figure 2.12: Hovmoeller plot of the total advective atmospheric heat transport (top), the contribution of the mean meridional circulation (bottom), and the contribution of eddies (bottom), all given in PW; for a reduction of TSI to 91% of its present-day value (simulation TSI91). The thick black lines display the zero contour level. Contour intervals are 0.5 PW. A 15-year running mean is applied. Sea-ice cover is completed by year 480.

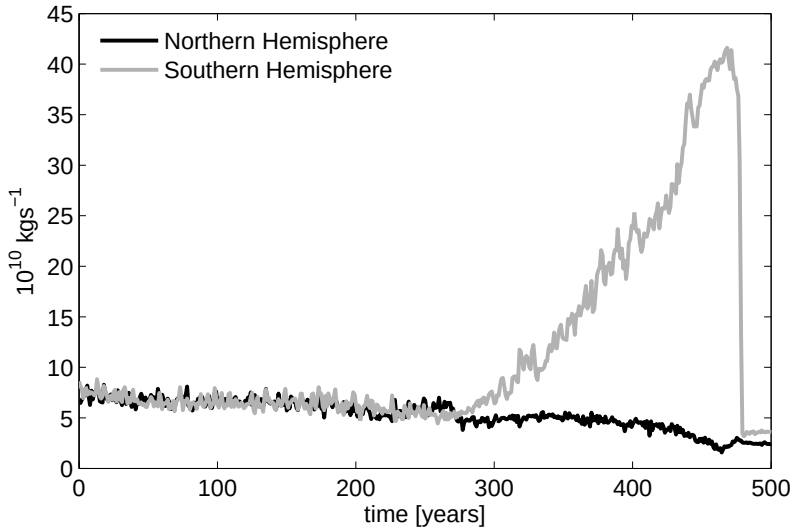

Figure 2.13: Annual mean absolute maximum values of the Hadley cell branch in the Northern Hemisphere (black) and the Southern Hemisphere (gray) for a reduction of TSI to 91% of its present-day value (simulation TSI91).

2.7 Point of unstoppable glaciation

We will now turn to the second set of our experiments summarized in Table 2.2. At different stages of sea-ice cover of the simulation TSI91 we increase TSI to investigate which degree of sea-ice cover guarantees an unstoppable transition to a modern Snowball Earth, even if TSI is increased at this point (see Fig. 2.18). Setting TSI to 100% causes rapid melting of sea ice even for an almost completely frozen ocean with 87.7% sea-ice cover (simulation R1-TSI100). Although the Atlantic and the Indian Ocean are already completely covered with sea ice and only a narrow band of open water is left in the equatorial Pacific, sea-ice cover decreases rapidly after the increase of TSI to 100%. This picture is different if TSI is increased to less than 100%. Even if we start from simulation TSI91 with only 56.6% sea-ice cover, a TSI increase to 94% does not prevent a Snowball Earth but complete sea-ice cover is realized within 393 years (simulation R2-TSI94). The intermediate state with constant sea-ice cover of 55% during 300 years but slow cooling of the ocean by a rate of 0.3 PW (corresponding to 0.8 Wm^{-2}) has a very sharp sea-ice edge at 10° S showing almost no seasonal or interannual variability. In the Northern Hemisphere, the sea-ice edge is less uniform and shows more interannual and seasonal variability with sea ice reaching 30° N in March and retreating to 55° N in September in the North Pacific. That this intermediate state for 94% TSI_0 eventually freezes over implies that also for TSI values below 94% TSI_0, sea-ice cover above 56.6% is unstable and results in a modern Snowball Earth. This is confirmed by simulation

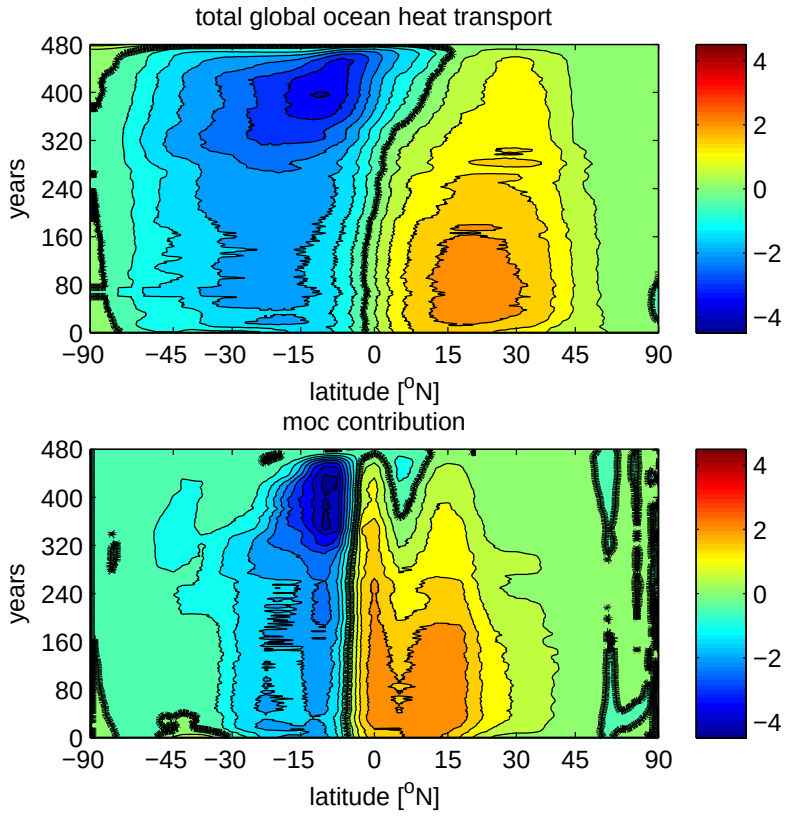

Figure 2.14: Hovmoeller plot of the total global ocean heat transport (top), and the contribution by the MOC (bottom), both given in PW; for a reduction of TSI to 91% of its present-day value (simulation TSI91). The thick black lines display the zero contour level. Contour intervals are 0.5 PW. A 15-year running mean is applied. Sea-ice cover is completed by year 480.

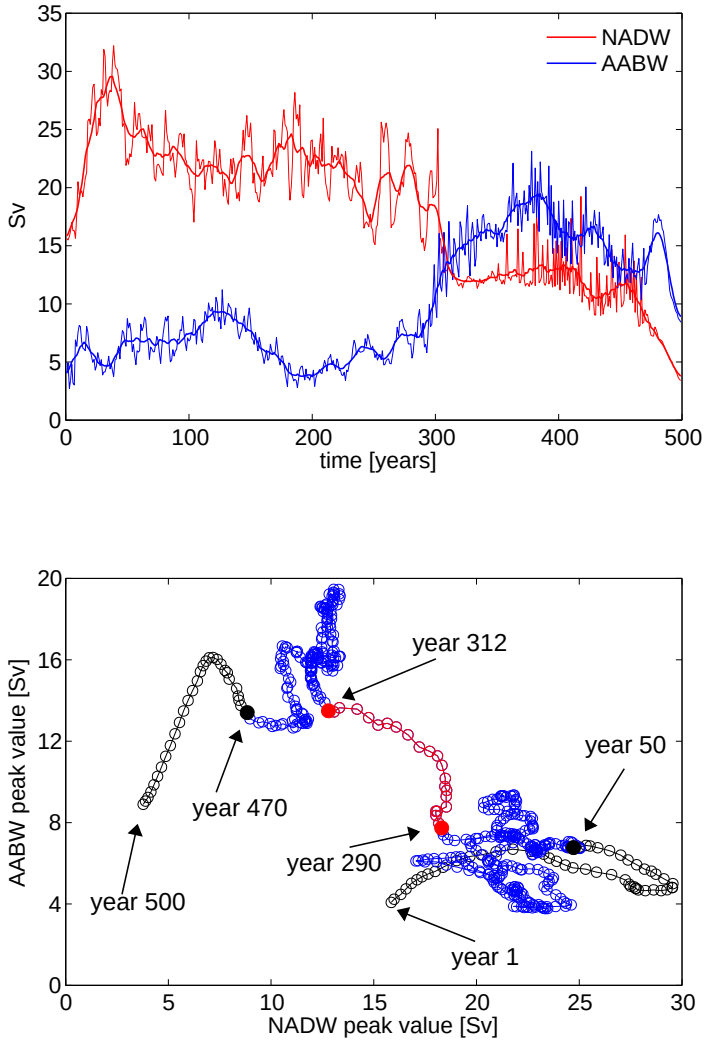

Figure 2.15: Top: time series of the absolute peak values of the NADW and AABW cells in the Atlantic for a reduction of TSI to 91% of its present-day value (simulation TSI91). The thick lines depict the 15-year running means. Bottom: phase-space trajectory of the 15-year running means. Sea ice in the Atlantic is completed by year 470.

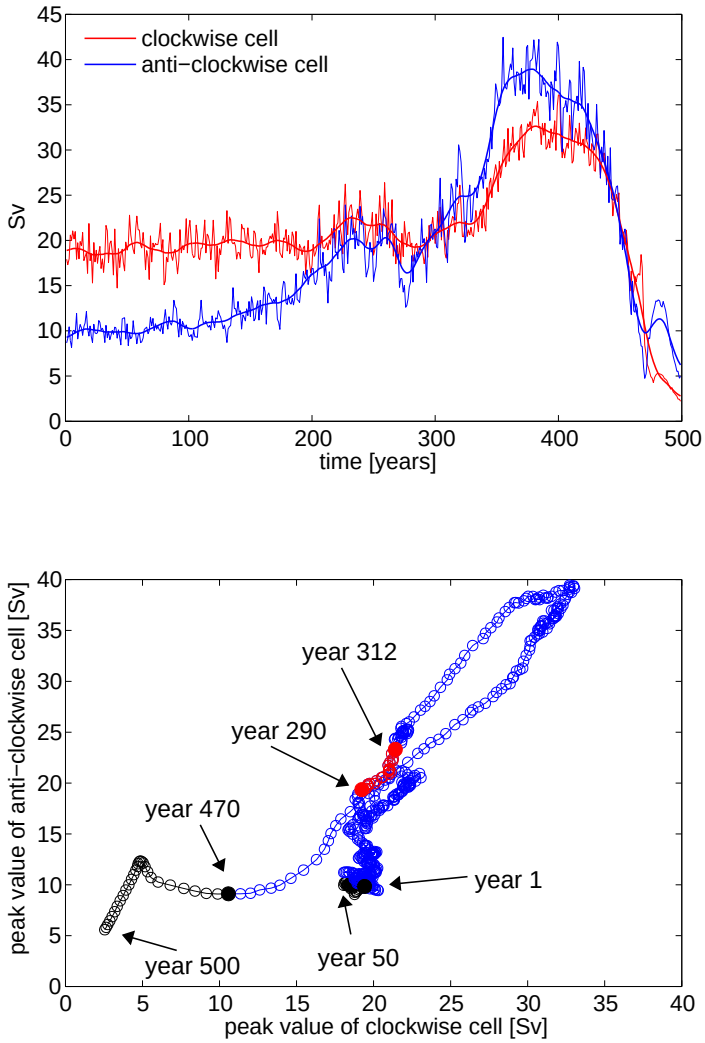

Figure 2.16: Top: time series of the absolute peak values of the wind-driven subtropical ocean overturning cells of the Atlantic for a reduction of TSI to 91% of its present-day value (simulation TSI91). The thick lines depict the 15-year running means. Bottom: phase-space trajectory of the 15-year running means. Sea ice in the Atlantic is completed by year 470.

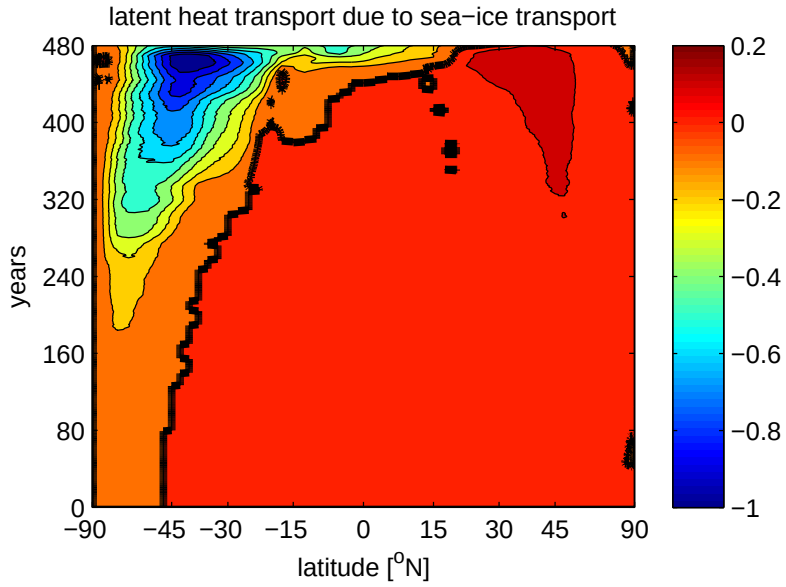

Figure 2.17: Hovmoeller plot of the latent heat transport due to sea-ice transport in PW for a reduction of TSI to 91% of its present-day value (simulation TSI91). Contour intervals are 0.1 PW. A 15-year running mean is applied.

R4-TSI93. Increasing TSI to 94% at 34.1% sea-ice cover in the simulation TSI91 leads to melting of sea ice with sea-ice cover after 100 years being close to that at the end of simulation TSI94. This implies that if we start from the present-day control climate and reduce TSI to values between 94% and 100% TSI_0, sea-ice cover will not exceed 34.1% in ECHAM5/MPI-OM. Assuming that ECHAM5/MPI-OM does not exhibit an additional stable mode between the present-day like and the Snowball Earth mode, we conclude that stable states can have no greater than 56.6% sea-ice cover.

To study the extent to which the point of unstoppable glaciation for 100% TSI_0 depends on sea-ice thickness and mean ocean potential temperature, we conduct the simulations RR1-TSI100 and RR2-TSI100 where we set TSI back to 100% shortly before global sea-ice cover is realized in the simulation R2-TSI94. Increasing TSI to 100% prevents the transition to a Snowball Earth for a sea-ice cover of 81.7% (simulation RR1-TSI100) but does not inhibit complete sea-ice cover for a slightly higher sea-ice cover of 87.7% (simulation RR2-TSI100). The simulation RR2-TSI100 starts from the same degree of sea-ice cover as the simulation R1-TSI100, but sea ice is 0.5 m thicker and the ocean is 0.42 K colder than for the experiment R1-TSI100 (see Table 2.3). While it is not surprising that the point of unstoppable glaciation is shifted to smaller degrees of sea-ice cover with lower ocean temperatures and thicker sea ice, we can estimate a lower bound for the point of unstoppable glaciation for 100% TSI_0. As

ECHAM5/MPI-OM at the beginning of the simulation RR1-TSI100 is already close to the maximum value of sea-ice thickness of 8 m and minimum value of mean ocean potential temperature of $-1.9°$ C, the point of unstoppable glaciation for 100% TSI_0 should be above 80% sea-ice cover, independent of the explicit state chosen to set TSI back to 100%. Together with the simulations R2-TSI94 and R3-TSI94 showing that the point of unstoppable glaciation for 94% TSI_0 is below 56.6% sea-ice cover, this demonstrates a strong dependence of the point of unstoppable glaciation on TSI.

The classical energy balance models of Budyko (1969) and Sellers (1969) describe the climate only in terms of sea-ice cover and neglect other variables of the climate system. This is certainly an oversimplification of the ECHAM5/MPI-OM model as well as the "true" climate system. We now analyze how strong this simplification is in the case of ECHAM5/MPI-OM, by investigating the correlation of mean ocean potential temperature and sea-ice cover for various ECHAM5/MPI-OM simulations (see Fig. 2.19). If the energy balance models, and hence the Budyko-Sellers diagram, were a complete description of the ECHAM5/MPI-OM model, all simulations would give exactly the same mean ocean potential temperature for the same sea-ice cover indicating that sea-ice cover completely describes the state of the climate system. Indeed, all simulations of the transition from the present-day climate to a modern Snowball Earth triggered by an abrupt decrease of TSI (cf. Tab. 2.1) roughly show the same dependence of mean ocean potential temperature on sea-ice cover. Note that simulations of the first set not included in Fig. 2.19 fall in the region covered by the selected simulations shown in Fig. 2.19. This shows that sea-ice cover is a sufficient description of the climate state of ECHAM5/MPI-OM when the climate model evolves from the present-day climate into a modern Snowball Earth. The physical reason here is that the formation of sea ice requires that most parts of the underlying water column are cooled to close to the freezing point (see Sect. 2.4). In contrast, the simulation R1-TSI100 (cf. Tab. 2.2) is not in accordance with the above correlation of mean ocean potential temperature and sea-ice cover, because melting of sea ice only requires to warm the ocean surface layers and hence leaves the mean ocean potential temperature largely unaffected.

2.8 Discussion

In the coupled atmosphere-ocean general circulation model ECHAM5/MPI-OM, the Snowball Earth bifurcation point for the transition to a Snowball Earth is in the range of 91% to 94% of today's total solar irradiance (TSI). This is in agreement with the FOAM atmosphere-ocean general circulation model despite differences in the applied geography (Poulsen and Jacob 2004).

The transition times to a Snowball Earth have only been studied with a simple climate model (Walsh and Sellers 1993); a time-dependent decrease of total solar irradiance by 30% over 90 years resulted in a Snowball Earth within 81 years. This is broadly

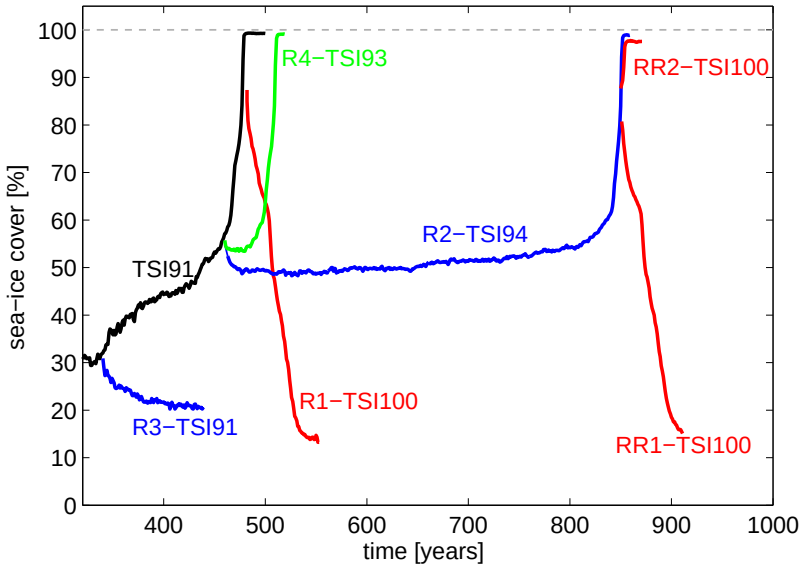

Figure 2.18: Response of sea-ice cover in percentage of ocean area after an increase of TSI at different stages of the simulation TSI91 (black). Green means an increase of TSI to 93%, blue an increase of TSI to 94%, and red an increase of TSI to 100% of its present-day value. The plot also includes two simulations where we set TSI back to 100% one year before complete sea-ice cover is accomplished in the simulation R2-TSI94. The simulations can be identified by the labels attached to the lines of sea-ice cover evolution (cf. Tab. 2.1 and 2.2).

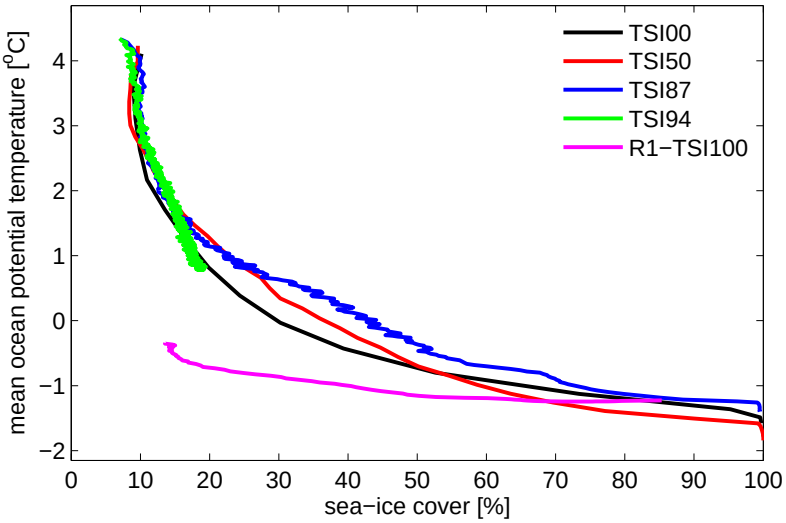

Figure 2.19: Annual mean ocean potential temperature in dependence of sea-ice cover for four simulations applying an abrupt decrease of TSI (black, red, blue, green) and one simulation where we increased TSI to 100% shortly before sea-ice cover is complete (magenta).

Table 2.3: Summary of sea-ice cover in percentage of the total ocean area, mean sea-ice thickness and mean ocean potential temperature before the increase of total solar irradiance to 100% for three simulations of the second set of ECHAM5/MPI-OM simulations. SE abbreviates Snowball Earth.

simulation	sea-ice cover at restart (Dec. mean)	sea-ice thickness at restart (Dec. mean)	ocean temperature at restart (annual mean)	result
R1-TSI100	87.7%	5.98 m	271.94 K	melting
RR1-TSI100	81.7%	6.12 m	271.54 K	melting
RR2-TSI100	87.7%	6.48 m	271.52 K	SE within 2 a

consistent with our simulation with 75% TSI_0 giving a transition times of 109 years, although the simplicity of this earlier model and the different strategy of TSI decrease render a comparison difficult.

In contrast to a previous study with the Earth system model of intermediate complexity PUMA (Romanova et al. 2006), our model ECHAM5/MPI-OM is very sensitive to a decrease in atmospheric carbon dioxide. When we remove virtually all carbon dioxide from the atmosphere, the Earth freezes over even with 100% TSI_0. While the sole radiative effect of CO_2 is too small to trigger a Snowball Earth, removing CO_2 activates the ice-albedo and water-vapor feedbacks. In contrast to the Snowball Earth literature, which almost exclusively focuses on the ice-albedo feedback alone, we find that the water-vapor feedback is also key to the initiation of a Snowball Earth, as seen by the strong increase in the clear-sky emissivity (see also Pierrehumbert (2002) and Fraedrich (1979)). We speculate that ECHAM5/MPI-OM has less difficulties generating a Snowball Earth partly due to a strong water-vapor feedback in our model, consistent with ECHAM5/MPI-OM simulations of the Paleocene-Eocene (55 Ma before present) presented in Heinemann et al. (2009). There, strong reductions in the clear-sky surface emissivity are key to explain the high climate sensitivity of those simulations, and the water-vapor feedback is thought to be one of the main reason for the simulated reduction in clear-sky surface emissivity. Clouds in ECHAM5/MPI-OM always exert a negative radiative forcing. This is in contrast to the results of Poulsen and Jacob (2004) and makes clear that clouds are an important point of discrepancy between models (see also Le Hir et al. (2007) for the influence of clouds on the deglaciation threshold of a Snobwall Earth).

Our analysis of the climate with sea ice extended to 40° N/S due to a decrease of TSI to 94% shows a decrease of atmospheric heat transport compared to the present-day control simulation CTRL. In the literature, there is only a single study that systemati-

cally investigates the response of atmospheric heat transport to sea-ice expansion. Using the CLIMBER-2 model with a Neoproterozoic continental reconstruction, Donnadieu et al. (2004b) found that a decrease of atmospheric carbon dioxide from 3500 ppm to 500 ppm caused an expansion of sea ice from 60° N/S to 40° N/S. These simulations should therefore be comparable to our present-day control simulation CTRL and our simulation TSI94 with 94% TSI_0. While in CLIMBER-2 sea-ice expansion lead to an increase of atmospheric heat transport in both its mean meridional and eddy components, our simulations suggest the completely opposite. We find a decrease in atmospheric heat transport, which is entirely due to a decrease of atmospheric eddy heat transport. This questions the conclusion in Donnadieu et al. (2004b) that atmospheric heat transport represents a negative feedback working against sea-ice advance, and illustrates that the role of atmospheric heat transport during the transition to a Snowball Earth is still unclear. Concerning the ocean heat transport, we find similar hemisphere-dependent changes as in Donnadieu et al. (2004b).

Why do we see an intensification of southward and a decline of northward atmospheric and oceanic heat transports as sea ice comes close towards the equator? The answer lies in the present-day asymmetric distribution of the continents. In ECHAM5/MPI-OM, sea-ice covered ocean areas have a substantially higher albedo than frozen land areas because of two reasons. First, the albedo of snow-free land largely depends on the assumed background albedo, which is in the range of 0.1 to 0.3 for most land areas. This is much lower than the albedo of sea ice. Second, snow causes less albedo increase on land than on sea ice, since snow on land has a lower minimum albedo than snow on sea ice, and the albedo effect of snow on land is further diminished by the shielding effect of forests as well as the effect of decrease in fractional snow cover as a consequence of sloping terrain. This difference in the albedo of sea-ice areas and frozen land areas results in a larger surface albedo in the Southern than the Northern Hemisphere after year 240 for a reduction of TSI to 91% of its present-day value (see Fig. 2.20). Consequently, the Southern Hemisphere receives less shortwave radiation than the Northern Hemisphere, and this deficit must be balanced by anomalous southward heat transport, compared to the present-day climate. This also explains the faster expansion of sea ice in the Southern Hemisphere seen for the simulations with 75% to 91% TSI_0 (cf., Sect. 2.4).

How do our simulations then help us understand the role of atmosphere and ocean heat transports and dynamics? First, we can say with confidence that the wind-driven meridional overturning circulation intensifies strongly during the transition and hence becomes more and more important for meridional ocean heat transport as sea ice spreads towards the equator. This is in agreement with a previous sensitivity study with an atmosphere-ocean general circulation model that showed that the wind-driven ocean circulation is an important factor to make global glaciation more difficult (Poulsen and Jacob 2004). Second, we also see the importance of sea-ice dynamics in our simulations,

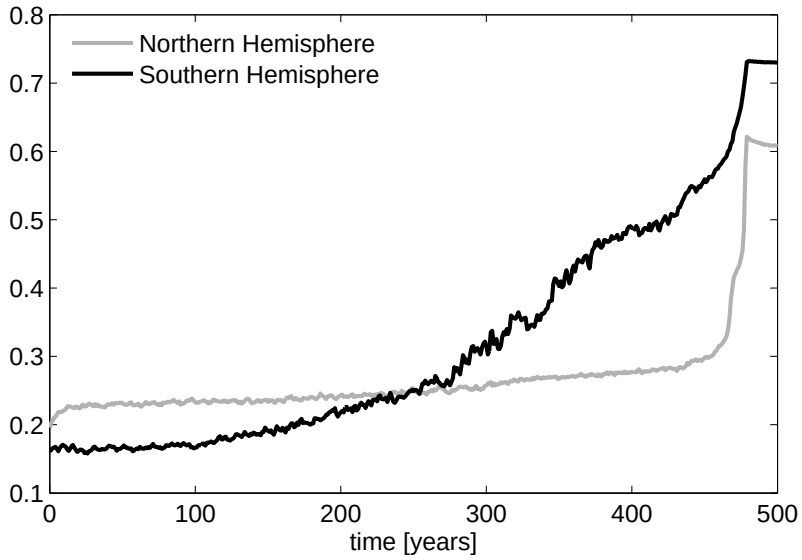

Figure 2.20: Surface albedo of the Northern and Southern Hemisphere during the transition to a modern Snowball Earth triggered by a reduction of TSI to 91% (simulation TSI91). Sea-ice cover is completed by year 480.

in accordance with Lewis et al. (2003, 2007). Meridional sea-ice transport not only leads to poleward latent heat transport and hence a cooling of the open water regions, but it also cools the preciously open water regions by the high albedo of the exported sea ice. Third, we see a strong intensification of the Hadley cell when sea ice enters the tropical region, and a weakening of the Hadley cell just prior to the accomplishment of final glaciation, again in accordance with Poulsen and Jacob (2004). The simultaneous increase of southward heat transport in the tropics by the mean meridional circulations in the atmosphere and the ocean reflects the strong coupling between both mechanisms (cf., Held 2001). A stronger Hadley cell means stronger surface winds and consequently an increase in the wind-driven subtropical ocean cells. This confirms the peculiar role of surface winds that has also been recognized in previous studies (Poulsen and Jacob 2004; Lewis et al. 2003, 2007).

While the existence of the point of unstoppable glaciation and hence a runaway ice-albedo feedback is inevitable as soon as the meridional heat transport is nonzero (Held and Suarez 1974), it is a-priori unknown where this point is located. For 100% TSI, we find that this point should be above 80% sea-ice cover, which is much closer to complete sea-ice cover than the position of the unstable branch in classical energy balance models (e.g., North 1975). The melting of a near-Snowball Earth in Poulsen (2003) is consistent with our simulations for an increase of TSI to 100% TSI_0. However, this alone does not justify the conclusion of a weak runaway ice-albedo feedback for Neoproterozoic

boundary conditions drawn in Poulsen (2003) due to the strong dependence of the point of unstoppable glaciation on TSI found in our study.

In ECHAM5/MPI-OM there is no TSI value resulting in stable climates with sea-ice cover above 56.6%, i.e. we do not find stable states with near-complete sea-ice cover but open equatorial waters. This is in contrast to Poulsen and Jacob (2004) who find that 65% sea-ice cover is stable in the FOAM model. Obvious reasons for this discrepancy are differences in the cloud radiative forcing above sea ice (close to zero in ECHAM5/MPI-OM, but about 30 Wm^{-2} in FOAM) and missing sea-ice dynamics in FOAM. Differences in the strength of the water-vapor feedback and different values for sea-ice albedo might also be important, but a comparison is hindered as Poulsen and Jacob (2004) do not provide data for these variables. To judge whether differences in the applied geography (modern in our study, but equatorial supercontinent in Poulsen and Jacob (2004)) are important for the differences in the stability threshold would require to repeat our simulations with Neoproterozoic continents, which is beyond the scope of this study. There are nonetheless two interesting issues regarding the location of continents. First, the strong southward heat transport seen in our study clearly is a consequence of choosing modern continents due to the vastly different albedo of ocean, sea ice, and land. Second, it recently has been demonstrated that ocean heat transport plays a major role in setting the latitude of the sea-ice edge (Rose and Marshall 2009; Ferreira et al. 2009) as sea ice tends to rest at minima of ocean heat transport, and that the structure of meridional ocean heat transport itself is sensitive to continental boundaries (Enderton and Marshall 2009). Altogether, this proposes a new and yet unexplored mechanism of how the location of continents might influence the stability threshold.

ECHAM5/MPI-OM neither includes a dynamic vegetation nor an ice sheet model. The use of a vegetation mask fixed to the present-day climate results in too low land albedos for regions with present-day forest cover like Siberia or the tropical rain forest regions due to the shielding effect of forests. The same is true for the lack of a dynamic ice sheet model although we consider it to be less important for our study as most of our simulations are rather short. Finally, the restriction of sea-ice thickness to about 8 m in MPI-OM to avoid dry model layers introduces an artificial heating source below the sea ice. Altogether, these three deficits bias our model results to an overestimation of the transition times. Similarly, the estimated range of the Snowball Earth bifurcation point would shift to higher TSI values if these three deficits were removed. They should be addressed when one attempts to simulate the equilibrium climate of a Snowball Earth, but we here consider them not to be of first order for modelling the transition from the present-day climate to a Snowball Earth. Apart from the transition to a modern Snowball Earth, including an ice sheet model would allow us to test the existence of "oasis" solutions in an atmosphere-ocean general circulation model. These "oasis" solutions, found in an energy balance model coupled to an ice sheet model (Crowley et al. 2001;

Peltier et al. 2004, 2007), exhibit tropical land glaciers while tropical oceans remain sea-ice free and are located in between the present-day like mode and the Snowball Earth mode in plots of global surface temperature vs. total solar irradiance or longwave CO_2 forcing.

We have only modelled the physical climate system comprising atmosphere, ocean, and sea ice. Atmospheric carbon dioxide levels are fixed in our study. It is certainly interesting to include the interactions of climate and carbon dioxide in Snowball Earth simulations. For example, the continental break-up of Rodinia was shown to trigger a Snowball Earth due to an increase in runoff and due to basaltic traps in the GEOCLIM model (Donnadieu et al. 2004a; Godderis et al. 2007). Moreover, it has been suggested that including the Neoproterozoic carbon cycle proposed by Rothman et al. (2003) may inhibit global glaciations (Peltier et al. 2007) though this is still a matter of debate (Godderis and Donnadieu 2008; Hoffman et al. 2008; Peltier and Liu 2008). We leave these issues for future research.

2.9 Conclusions

Based on our simulations with the coupled atmosphere-ocean general circulation model ECHAM5/MPI-OM to study the transition from the present-day climate to a modern Snowball Earth, we conclude the following:

1. The Snowball Earth bifurcation point of ECHAM5/MPI-OM is between 91% and 94% of the present-day total solar irradiance (TSI), in agreement with the FOAM atmosphere ocean general circulation model (Poulsen and Jacob 2004). The transition time from the present-day climate to a modern Snowball Earth increases from 14 years for virtually switching off the sun to 480 years for decreasing TSI to 91% of its present-day value.

2. The Snowball Earth bifurcation point and the transition time found with ECHAM5/MPI-OM are well reproduced with a zero-dimensional energy balance model of the mean ocean potential temperature.

3. The asymmetric distribution of continents between the Northern and Southern Hemispheres causes strong heat transports toward the more water-covered Southern Hemisphere as sea ice spreads towards the equator. The southern Hadley cell and the wind-driven subtropical ocean cells strengthen by a factor of 4 as sea ice approaches the equator.

4. For 100% TSI the point of unstoppable glaciation is much closer to complete sea-ice cover than in classical energy balance models. Stable states have no greater than 56.6% sea-ice cover implying that ECHAM5/MPI-OM does not exhibit stable states with near-complete sea-ice cover but open equatorial waters.

Chapter 3

Initiation of a Marinoan Snowball Earth in a state-of-the-art atmosphere-ocean general circulation model

We use the state-of-the-art atmosphere-ocean general circulation model ECHAM5/MPI-OM to revisit the initiation of a Snowball Earth for Marinoan surface boundary conditions (635 million years before present). The comparison with a pre-industrial control climate shows that the change of surface boundary conditions from present-day to Marinoan, including a shift of continents to low latitudes, induces a global-mean cooling of 4.6 K. Two thirds of this cooling can be attributed to increased planetary albedo, the remaining one third to increased effective emissivity, i.e. a weaker greenhouse effect. The Marinoan Snowball Earth bifurcation point for pre-industrial atmospheric carbon dioxide is between 95.5 and 96% of the present-day total solar irradiance (TSI), implying that Snowball Earth initiation is much easier for Marinoan than present-day surface boundary conditions. A Snowball Earth for TSI set to its Marinoan value (94% of the present-day TSI), is prevented by quadrupling carbon dioxide with respect to its pre-industrial level. A zero-dimensional energy balance model successfully predicts the Snowball Earth bifurcation point by only knowing the equilibrium global-mean ocean potential temperature for the present-day value of TSI. Sea-ice cover above 55% is unstable, akin to what was found for present-day surface boundary conditions. ECHAM5/MPI-OM hence does not exhibit states with near-complete sea-ice cover but open equatorial waters. In summary, Snowball Earth initiation in a state-of-the-art coupled climate model is possible for Marinoan surface boundary conditions and Marinoan TSI by reducing atmospheric carbon dioxide to its pre-industrial level. This contradicts previous conclusions that Snowball Earth initiation would require "extreme" forcings.

3.1 Introduction

The apparent existence of low-latitude land glaciers at sea level during at least two episodes of the Neoproterozoic era, the Sturtian ($\sim$ 710 million years before present,

Ma) and the Marinoan($\sim$ 635 Ma) (Evans 2000; Trindade and Macouin 2007; Macdonald et al. 2010), has led to the proposal that these glaciations must have been accompanied by completely frozen oceans. This so-called "Snowball Earth" hypothesis (Kirschvink 1992; Hoffman et al. 1998) has not only attracted the attention of geologists, but also of climate modellers, who have tested if the Snowball Earth hypothesis is compatible with climate physics. In this study, we use the state-of-the-art atmosphere-ocean general circulation model ECHAM5/MPI-OM to revisit the initiation of a Snowball Earth for Marinoan surface boundary conditions, a main feature of the latter being the preponderance of continents in low latitudes. In particular, we investigate the Snowball Earth bifurcation point and the maximum stable sea-ice cover.

We are by far not the first to confront the Snowball Earth hypothesis with climate models. Indeed, the Snowball Earth hypothesis itself relies on a runaway ice-albedo feedback first reported in energy balance models (e.g., Budyko 1969; Sellers 1969). After the initial perception that the Snowball Earth hypothesis is, in principle, compatible with climate physics, the last decade has seen the full hierarchy of climate models being applied to Snowball Earth initiation. While we do not know of any climate model that excludes Snowball Earth solutions categorically, various climate modelling studies concluded that completely frozen oceans require "extreme" forcings (Chandler and Sohl 2000; Poulsen et al. 2001; Poulsen 2003; Poulsen and Jacob 2004) that might be considered unrealistic for the Neoproterozoic. At the same time, Hyde et al. (2000) and Peltier et al. (2004), using an energy balance model with interactive ice sheets, found so-called "Slushball Earth" or "oasis" solutions that are characterized by tropical land glaciation but open equatorial water. Despite severe limitations of their model, including the disregard of atmosphere and ocean dynamics, these solutions have been supported by an atmospheric general circulation model coupled to a slab ocean and prescribed full continental glaciation (Hyde et al. 2000; Baum and Crowley 2001). Moreover, Chandler and Sohl (2000) and Micheels and Montenari (2008) found, also using atmospheric general circulation models coupled to slab oceans, solutions with equatorial land masses below freezing in conjunction with almost but not completely frozen oceans. As a result, the apparent difficulties in freezing the entire ocean combined with the possibility that equatorial land glaciers might not require completely frozen oceans evoked the impression that the Snowball Earth hypothesis was implausible from the perspective of climate modelling, and attention shifted to the Slushball Earth hypothesis (Lubick 2002; Kaufman 2007; Kerr 2010).

We here study the initiation of a Marinoan Snowball Earth in the state-of-the art atmosphere-ocean general circulation model ECHAM5/MPI-OM. This model incorporates physics found to be essential for Snowball Earth initiation but neglected in models supporting the Slushball Earth hypothesis, including ocean dynamics (Poulsen et al. 2001; Poulsen and Jacob 2004), sea-ice dynamics (Lewis et al. 2003, 2007) and clouds (Poulsen and Jacob 2004). By comparing the simulations to a previous study of two of

us with this model for present-day surface boundary conditions (Voigt and Marotzke 2009), we also can reevaluate if low-latitude continents favor Snowball Earth initiation as suggested by Kirschvink (1992), something that was rebutted by Poulsen et al. (2002).

This study addresses two issues. First, we investigate the climatic effect of changing surface boundary conditions from present-day to Marinoan. To this end, we generate a Marinoan control climate for present-day total solar irradiance (TSI) and pre-industrial greenhouse gas concentrations by integrating the model to equilibrium ($\sim$ 3500 years) for Marinoan surface boundary conditions. We compare the Marinoan control climate to the pre-industrial control climate by means of a one-dimensional energy balance model. This allows us to identify and quantify the mechanisms responsible for the surface temperature change induced by the change of surface boundary conditions.

Second, we estimate the Snowball Earth bifurcation point and the maximum stable sea-ice cover of the model for Marinoan surface boundary conditions. For this, we start the model from the Marinoan control climate and abruptly decrease TSI, in some cases combined with an simultaneous increase of carbon dioxide. This is the same experimental strategy as in Voigt and Marotzke (2009).

The paper is organised as follows. Section 2 describes the climate model, the Marinoan surface boundary conditions, and the setup of the ECHAM5/MPI-OM simulations, including the spinup of the Marinoan control climate. Section 3 analyzes the Marinoan control climate and compares it to a pre-industrial control simulation by means of a one-dimensional energy balance model of zonal mean surface temperature. Section 4 investigates the Snowball Earth bifurcation point and maximum stable sea-ice cover. A zero-dimensional energy balance model of the diagnosed global-mean ocean potential temperature is used to predict the Snowball Earth bifurcation point in Section 5. Section 6 points at an imbalance of the global-mean top of atmosphere and surface energy fluxes. Section 7 gives a general discussion of the results, Sect. 8 follows with conclusions.

3.2 Model and simulation setup

3.2.1 Model setup

We apply the state-of-the-art atmosphere-ocean general circulation model ECHAM5/MPI-OM. This is the same model that was used to study the transition to a modern Snowball Earth (Voigt and Marotzke 2009), apart from technical changes to adapt the model to the new supercomputer of the German Climate Computing Center (DKRZ). ECHAM5/MPI-OM ranks among the world's top climate models and has been used for a variety of applications, ranging from climate projections for the Intergovernmental Panel on Climate Change (Solomon et al. 2007), including sea-level rise

(Landerer et al. 2007) and changes of the atmospheric energetics (Hernandez-Deckers and von Storch 2010) under global warming scenarios, to paleo-climate simulations of the Holocene and Eemian (Fischer and Jungclaus 2010) as well as the Paleocene/Eocene (Heinemann et al. 2009). The next two subsections provide details of the atmosphere and ocean model as well as the Marinoan surface boundary conditions used in this study.

Atmosphere general circulation model ECHAM5

The general circulation model ECHAM5, here used in version ECHAM5.3.02p, is the fifth generation of the ECHAM model series, which originally evolved from the weather prediction model of the European Centre for Medium Range Weather Forecasts. The main characteristics of the model, which is comprehensively documented in Roeckner et al. (2003), can be summarized as follows. ECHAM5 employs a spectral dynamical core to prognose vorticity, divergence, temperature, and the logarithm of surface pressure. Moisture variables (water vapor, cloud liquid water and cloud ice) and diabatic tendencies are calculated on a Gaussian grid. Tracer transport, including water transport, follows the flux-form semi-Lagrangian scheme of Lin and Rood (1996). The shortwave radiation scheme (Fouquart and Bonnel 1980) uses four spectral bands and takes into account Rayleigh scattering, absorption by water vapor, ozone, and well mixed gases (carbon dioxide, methane, nitrous oxide, cfc's, oxygen), and absorption and scattering by clouds and aerosols. Longwave radiation is calculated by the RRTM model (Mlawer et al. 1997) in 16 spectral bands. ECHAM5's stratiform cloud scheme includes prognostic equations for the vapor, liquid and ice phase and a cloud microphysical scheme based on Lohmann and Roeckner (1996). Land surface albedo equals a prescribed background albedo for zero snow cover. The presence of snow increases land surface albedo according to the fractional snow cover of the grid cell. Land snow albedo depends on land surface temperature and ranges from 0.3 at 0 °C to 0.8 at or below -5 °C. Ocean surface albedo is set to 0.07. Bare sea-ice albedo depends on sea-ice temperature and ranges from 0.55 at 0 °C to 0.75 at or below -1 °C. Snow on sea ice leads to a significant albedo increase: if the water equivalent of snow depth is larger than 0.01 m, sea-ice is treated as snow-covered. The albedo of snow-covered sea ice depends on snow surface temperature and ranges from 0.65 at 0 °C to 0.8 at or below -1 °C. The surface albedo of mixed grid cells is calculated as a fraction-weighted average of land, ocean, and sea-ice albedo.

Our Marinoan continents follow the reconstruction of M. Macouin (pers. com.) and are similar to, though less dispersed than, the continents used by Le Hir et al. (2009) (Fig. 3.1). In contrast to today, landmasses are largely clustered from 45° S to 30° N with two large equatorial continents separated by a narrow seaway. We will loosely call the continent centered around 60° W Laurasia, and the continent stretching from

0° E to 150° E Gondwana. Zonal mean land fraction from 60° S to 20° N is higher in the Marinoan than today, with the majority of the Marinoan landmasses located in the Southern Hemisphere.

Background surface albedo of land is set to 0.272 globally (see Table 3.1). This value is chosen such that the global mean background surface albedo of the Marinoan setup equals that of the pre-industrial setup when sea-ice and snow on land are set to zero and the temperature-dependent glacial albedo is assumed to be 0.725. This background surface albedo of land is close to the surface albedo of deserts suggested by Hagemann (2002) and is in line with the fact that land vegetation did not yet develop in the Marinoan. Forest ratio, vegetation ratio, and leaf area index consequently are zero. No land glaciers are prescribed. Surface roughness length and soil-water holding capacity are specified to bare desert values of $5 \cdot 10^{-3}$ m and 0.1 m, respectively (Hagemann 2002).

Orbital parameters are constant in time and correspond to year 800 A.D. Ozone follows the 1980 - 1991 climatology of Fortuin and Kelder (1998), aerosols are prescribed according to Tanré et al. (1984). Greenhouse gas concentrations are set to pre-industrial levels (CO_2=278 ppm, CH_4=650 ppb, N_2O=270 ppb, no cfc).

We do not posses any information on Marinoan orography. Land surface elevation is therefore set to 100 m globally, and ECHAM5's parametrization of gravity wave drag due to subgrid-scale orography (Lott and Miller 1997) is inactive in the Marinoan setup. Lateral water flow on continents is directed towards the nearest grid box with non-zero ocean fraction. No rivers or lakes are prescribed.

We stress that we use exactly the same ECHAM5 source code as for the transition to a modern Snowball Earth (Voigt and Marotzke 2009). This, in particular, applies to all tuning parameters of ECHAM5. Horizontal resolution is set to spectral truncation T31 ($\sim 3.75°$). In the vertical, 19 hybrid σ-levels that extend up to 10 hPa are employed. The time step is 2400 s.

Ocean general circulation model MPI-OM

The ocean is modeled by the Max-Planck-Institute Ocean Model MPI-OM, here used in version 1.2.3p2. MPI-OM is a z-coordinate global general circulation model that solves the Boussinesq approximation of the hydrostatic primitive equations (Marsland et al. 2003). In the horizontal, a curvilinear C-grid is applied. MPI-OM comes with a comprehensive suite of parametrizations, including along-isopycnal diffusion following Griffies (1998), horizontal tracer mixing by unresolved eddies according to Gent et al. (1995), and Richardson-number dependent vertical eddy diffusivity and viscosity in the style of Pacanowski and Philander (1981). Wind enhances vertical mixing close to the surface, and the calculation of wind stress takes into account ocean surface currents (Luo et al. 2005). Convection is modelled by greatly enhanced vertical diffusion. The

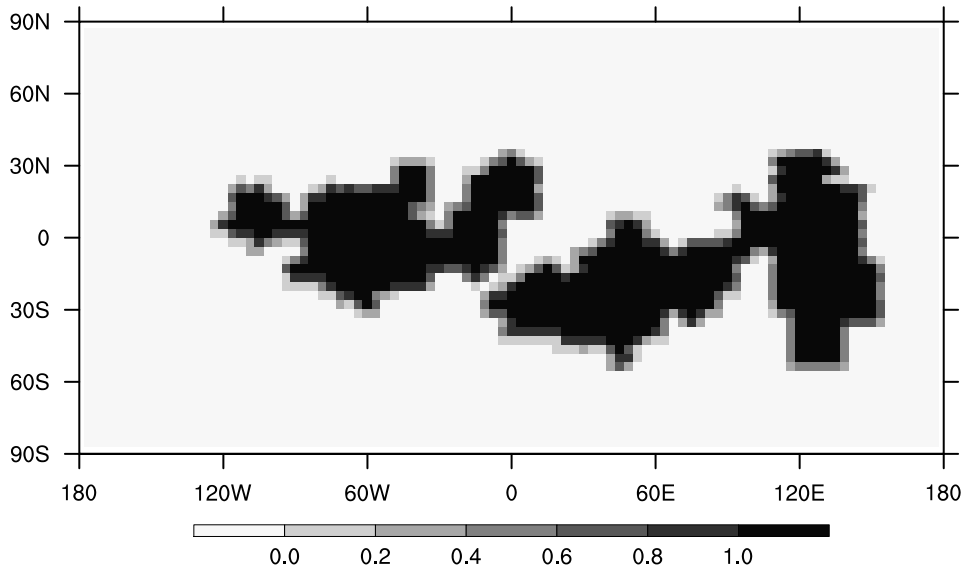

Figure 3.1: Marinoan land-sea mask as seen by the atmosphere model ECHAM5. Values of 1 correspond to pure land points, values of 0 to pure ocean points. Mixed grid boxes with land and ocean cover occur at the continental edges.

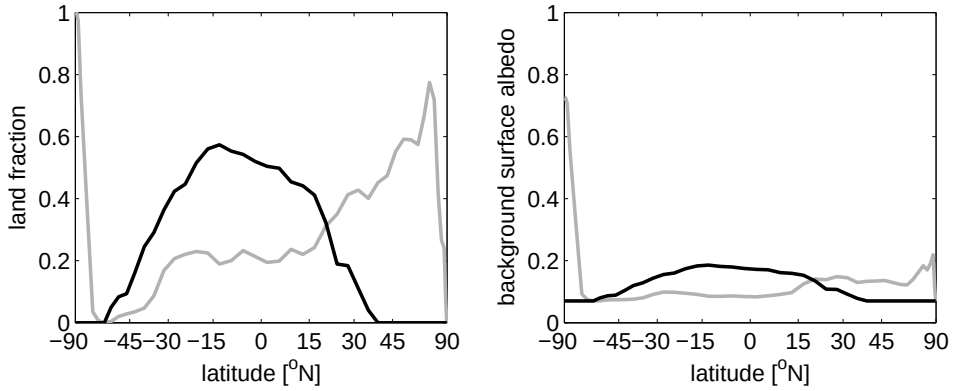

Figure 3.2: Zonal mean land-sea mask (left) and background surface albedo (right) of the Marinoan (black) and pre-industrial (gray) setup. The abscissa is linear in sine of latitude such that the spacing between the latitudes is proportional to the Earth's surface area between them.

Table 3.1: ECHAM5 input parameters for the Marinoan control simulation MAR and the pre-industrial control simulation PI. MAR uses a fixed orbit whose parameters are chosen to match the temporally varying orbital parameters of PI at year 800 A.D. PI uses the VSOP87 orbit (Variations Séculaire des Orbites Planétaires) of Bretagnon and Francou (1988), values given here are for year 800 A.D. according to Berger (1978) and are taken from *http://aom.giss.nasa.gov/srorbpar.html*. Land background surface albedo, soil data and land surface roughness length are globally uniform in MAR but vary spatially in PI; for the latter mean values are given. MAR's FAO soil data flag corresponds to sand. The pre-industrial control simulation is the same as in Voigt and Marotzke (2009).

input parameter	MAR	PI
CO_2	278 ppm	286.2 ppm
CH_4	650 ppb	805.6 ppb
NO_2	270 ppb	276.7 ppb
ozone	present-day	present-day
aerosols	Tanre	Tanre
CFC's	none	none
total solar irradiance	1367 Wm^{-2}	1367 Wm^{-2}
orbit	present-day and fixed in time	present-day and changing in time
eccentricity	0.0172	0.0172
obliquity	23.59°	23.59°
longitude of perihelion	262.4°	262.4°
land fraction	0.259	0.284
land surface background albedo	0.272	0.254
ocean surface albedo	0.07	0.07
vegetation	none	present-day
maximum field capacity of soil	0.1 m	0.6 m
FAO soil data flag	1	2.6
glaciers	none	present-day
surface roughness length over land	0.005 m	1.6 m
land surface elevation	100 m	901 m
gravity wave drag due to subgrid-scale orography	off	on

sea-ice model follows the dynamics of Hibler (1979) while the thermodynamics are incorporated by a zero-layer Semtner model relating changes in sea-ice thickness to a balance of radiative, turbulent, and oceanic heat fluxes (Semtner 1976). The freezing point of sea water is fixed to $-1.9°$ C independent of salinity. Snow on ice is explicitly modeled, including snow/ice transformation when the snow/ice interface sinks below the sea level because of snow loading. The effect of ice formation and melting is accounted for by assuming a sea-ice salinity of 5 psu. Sea-ice thickness is limited to about 8 m.

Atmosphere and ocean model are coupled via the OASIS3 coupler (Valcke et al. 2003) with a coupling time step of one day. The ocean passes sea surface temperature, sea-ice concentration and thickness, snow depth on ice, and ocean surface velocities to the atmosphere. The atmosphere provides wind stress, heat flux, freshwater flux including river runoff and glacier calving, and 10 m wind speed to the ocean model. In the presence of sea ice the fluxes are calculated separately for sea-ice covered and open water parts of the grid cells. No flux adjustments are applied.

Based on the reconstruction provided by M. Macouin (pers. com.), we generate a MPI-OM grid with 114x106 grid points and poles over Laurasia (51° W and 23° N) and Gondwana (128° E and 46° S). This gives high horizontal resolution with grid distances smaller than 50 km near the grid's poles but low resolution with grid distances up to 435 km in parts of the Northern hemisphere (Fig. 3.3). Apart from the spinup of the model (simulation SPINUP, see below), which employs the 40-level vertical grid of Voigt and Marotzke (2009), we use 39 vertical levels. These levels results from the 40-level vertical grid by merging the two uppermost levels. This change was necessary to ensure numerical stability of the ocean model during the transition to global sea-ice cover (cf. simulation TSI94, Table 3.2) and leads to a thickness of the uppermost level of 22 instead of 12 m. The time step is 5760 s. In some simulations, a reduced time step of 3600 s was needed to overcome numerical instabilities (see Table 3.2).

Marinoan ocean bathymetry is set to 5000 m globally. MPI-OM's scheme for bottom boundary layer slope convection is hence inactive in the Marinoan setup.

The MPI-OM source code is the same as in Voigt and Marotzke (2009), apart from technical changes needed to adapt MPI-OM to the new supercomputer of the German Climate Computing Center (DKRZ). We apply the same MPI-OM tuning parameters as in Voigt and Marotzke (2009). The only exception is that the Pacanowski-Philander vertical viscosity and diffusivity parameters (Marsland et al. 2003) are accidentally divided by five compared to the values used for the pre-industrial control run PI and the transition to a modern Snowball Earth (Voigt and Marotzke 2009). In Appendix A, we show that this does not affect our results. Details on how the Pacanowski-Philander vertical viscosity and diffusivity parameters, among other parameters, enter the calculation of vertical viscosity and diffusivity can be found in Marsland et al. (2003).

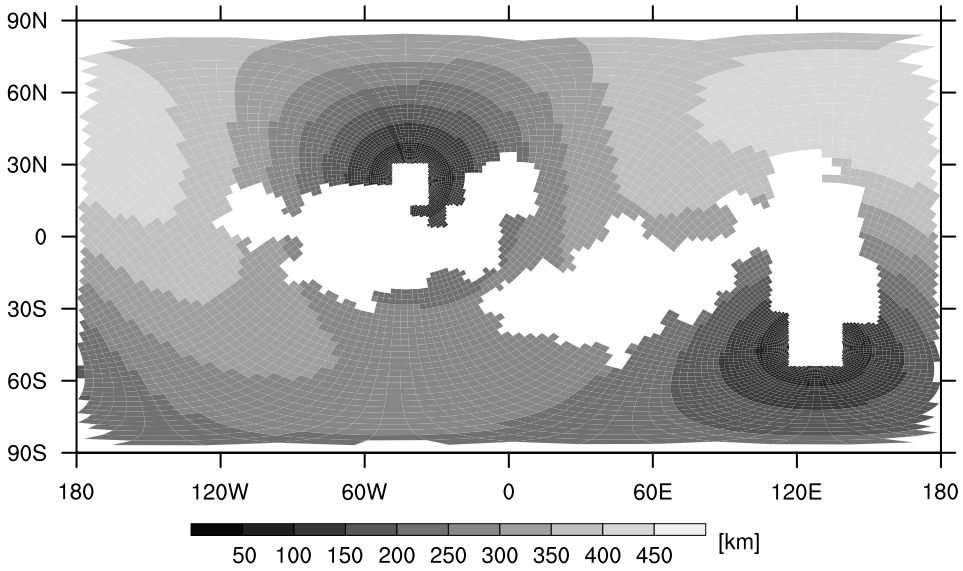

Figure 3.3: Horizontal grid distances of the Marinoan ocean grid as employed by the ocean model MPI-OM. Land points are left white. The white areas at the plot's edges are due to the cylindrical equidistant projection and do not indicate grid errors.

3.2.2 Simulation setup

We initialize ECHAM5/MPI-OM from warm atmospheric conditions and a quiescent homogeneous ocean at a potential temperature of 283 K and a salinity of 34.3 psu. The latter is approximately the salinity we would obtain in the present-day ocean if all glaciers were melted completely (Heinemann et al. 2009). Using the Marinoan surface boundary conditions and 40 vertical levels, the model is integrated for 3500 years (simulation SPINUP). After 3300 years, we branch off the Marinoan control simulation MAR. MAR applies, as all following simulations, 39 vertical levels. The pre-industrial control climate PI is the same as in Voigt and Marotzke (2009) and is obtained from the CERA database (Roeckner 2007). PI applies slightly higher atmospheric concentrations of carbon dioxide, methane and nitrous oxide than MAR (see Table 3.1). Based on Myhre et al. (1998) we estimate that this causes a radiative forcing difference of -0.27 Wm^{-2} between PI and MAR. In what follows, we neglect this small effect and discuss PI and MAR as if they employed the same concentrations of carbon dioxide, methane and nitrous oxide.

Table 3.2: Summary of ECHAM5/MPI-OM simulations. The applied total solar irradiance is given in percentage of the present-day value 1367 Wm^{-2}, the atmospheric carbon dioxide in percentage of its pre-industrial level. SE abbreviates Snowball Earth. Unless otherwise stated, simulations are started from year 3499 of MAR.

simulation	TSI	CO_2	simulated years	result	remark
PI	100%	286.2 ppm	100	pre-industrial control run	
SPINUP	100%	100%	0-3499	Marinoan spinup	40 vertical levels for ocean model
MAR	100%	100%	3300-3799	Marinoan control run	started from year 3299 of SPINUP
TSI00	0.01%	100%	3500-3509	SE at year 3509	
TSI94	94%	100%	3500-3999	SE at year 3854	
TSI96	96%	100%	3500-6199	sea-ice line at 30° N/25° S at year 6199	ocean time step of 3600 s after year 3979
TSI98	98%	100%	3500-3999	sea-ice line at 40° N/S at year 3999	
TSI94-4CO2	94%	400%	3500-4999	sea-ice line at 40° N/S at year 4999	
TSI94-6CO2	94%	600%	3500-4999	sea-ice line at 47° N/S at year 4999	
TSI955	95.5%	100%	5800-6019	SE at year 6000	started from year 5799 of TSI96, ocean time step of 3600 s
TSI100	100%	100%	4000-4099	stable SE	started from year 3999 of TSI94

Simulations with reduced total solar irradiance, in some cases combined with an increase of atmospheric carbon dioxide, are started from year 3499 of MAR (see Table 3.2). An additional simulation with total solar irradiance reduced to 95.5% (TSI955) is started from year 5799 of TSI96. Moreover, we perform one simulation where we TSI set back to 100% after complete sea-ice cover has been accomplished (TSI100). Throughout this study, years are counted with respect to model initialization at year 0.

The simulations performed to demonstrate the robustness of our results with respect to the choice of Pacanowski-Philander vertical viscosity and diffusivity parameters are described in Appendix 3.A.

3.3 Marinoan control climate and comparison to the pre-industrial control climate

In this section, we describe the annual mean Marinoan control climate MAR and compare it to the annual mean pre-industrial control climate PI. We will first focus on temperature and sea-ice extent before analyzing the atmosphere and ocean circulations as well as meridional heat transports. The section closes with a comprehensive analysis of the mechanisms that lead to the cold Marinoan control climate by means of a one-dimensional energy balance. For MAR, years 3400 to 3499 are used throughout this section.

3.3.1 Surface climate

The Marinoan setup results in an annual global mean surface temperature of 283 K (Table 3.3). Annual mean surface temperature is largely symmetric around the equator (Fig. 3.4). Its zonal mean attains 298 K in the tropics and drops to 245 K at the poles, implying an annual mean equator-to-pole temperature contrast of 43 K in both the Northern and Southern Hemispheres. This is slightly higher than the Northern Hemisphere contrast in PI. Close to the South Pole, MAR shows a local surface warming of more than 10 K compared to PI. This is a lapse rate effect caused by replacing the high elevation Antarctic continent of PI by sea-ice covered ocean in MAR. Land surface temperatures tend to be higher than sea-surface temperatures; the maximum annual mean surface temperature is 302 K in the center of Laurasia. Sea ice extends to 47° N/S in the annual mean. Poleward of 70° N/S, the ocean is covered with sea-ice year-round. Sea ice does nowhere grow beyond 3 m equatorward of 70° N/S but gets as thick as 7 m near the poles in the annual mean. Except very close to the annual-mean sea-ice margin, sea ice is covered by snow above 0.01 m water equivalent everywhere. The overwhelming part of the continents is snow-free; land snow-cover is restricted to the southernmost regions of Gondwana where snow depth reaches a water equivalent of 0.07 m at 133° E/50° S and of 0.02 at 60° E/52° S. The formation of snow on sea ice but

Table 3.3: Global mean values of key climate variables for the Marinoan (MAR) and pre-industrial (PI) control simulations. For MAR, years 3400 to 3499 are used. Albedo, effective emissivity, and cloud radiative forcing are calculated by time and global mean radiative fluxes.

	MAR	PI
surface temperature	283.0 K	287.6 K
mean ocean potential temperature	274.3 K	277.5 K
sea-ice area	$8.6 \cdot 10^{13}$ m^2	$2.1 \cdot 10^{13}$ m^2
planetary albedo	0.353	0.321
clear sky planetary albedo	0.210	0.163
surface albedo	0.244	0.170
effective emissivity	0.594	0.583
clear sky effective emissivity	0.675	0.656
vertically integrated water vapour	15.5 kgm^{-2}	25.1 kgm^{-2}
total cloud cover	0.654	0.620
shortwave cloud radiative forcing	-48.8 Wm^{-2}	-53.9 Wm^{-2}
longwave cloud radiative forcing	30.0 Wm^{-2}	28.7 Wm^{-2}
total cloud radiative forcing	-18.8 Wm^{-2}	-25.2 Wm^{-2}

not on land has important implications for surface albedo. While most sea-ice areas have an albedo above the bare sea-ice albedo, the albedo of most land areas remains at the prescribed background value. Consistent with lower surface temperatures, the annual and zonal mean water vapor content is lower in MAR than in PI at all latitudes except close to the South Pole. Cloud cover in MAR increases compared to PI in the tropics and poleward of 30° N/S but decreases in the subtropics.

3.3.2 Meridional circulations and heat transports of atmosphere and ocean

The meridional atmospheric circulation, measured by the Eulerian mass stream function, in each hemisphere exhibits the three-cell structure known from today's Earth (Fig. 3.5). Note that the polar cells are not visible because of the contour spacing. The Hadley circulation intensifies when surface boundary conditions are changed from pre-industrial to Marinoan, with the strength of the northern cell doubling from PI to MAR. The Marinoan Hadley circulation extends up to 150 hPa. This is as high as in PI and suggests that tropical tropopause heights in MAR and PI are similar, which is plausible from the only minor cooling of tropical surface temperatures in MAR though probably also is a consequence of prescribing a modern ozone climatology. The Ferrel

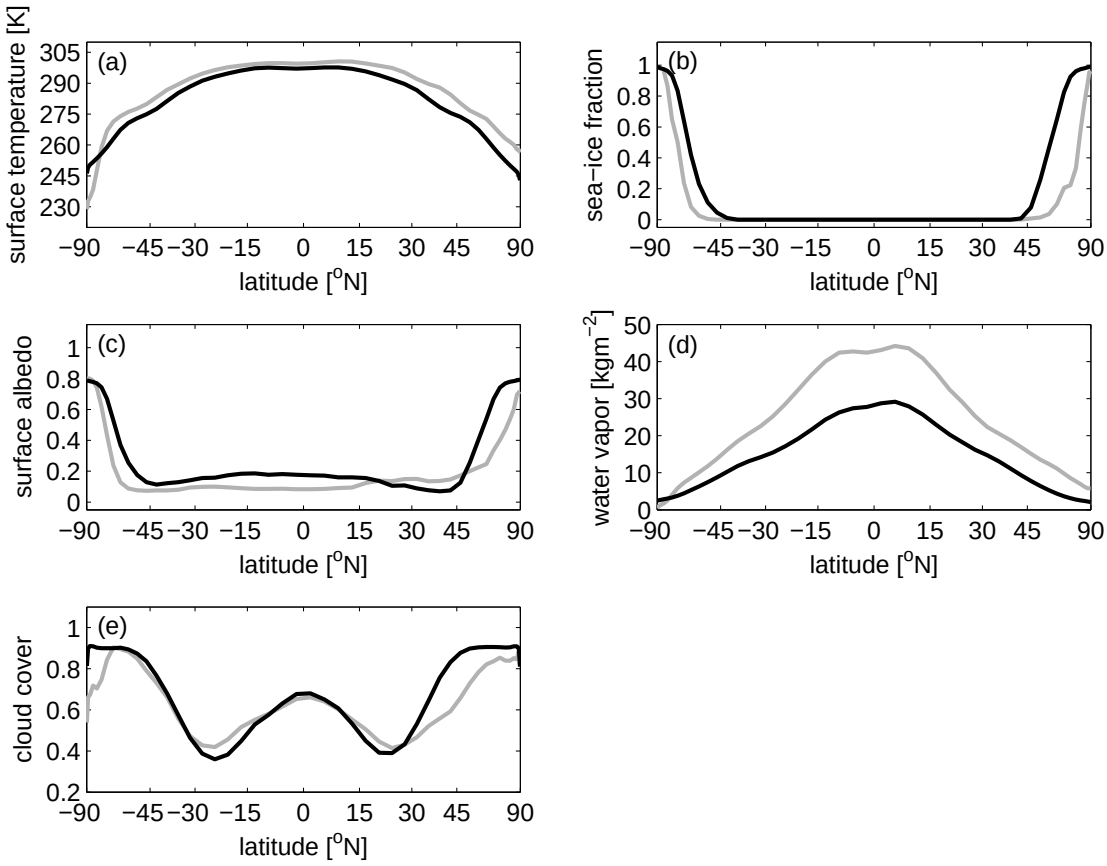

Figure 3.4: Time and zonal mean surface temperature (a), sea-ice fraction (b, only taking into account ocean points), surface albedo (c), vertically integrated water vapor (d), and cloud cover (e) in MAR (black) and PI (gray). For MAR, years 3400 to 3499 are used. The abscissae are linear in sine of latitude.

circulation is also stronger in MAR than in PI, with a now much more active Northern Hemisphere Ferrel cell but only slight acceleration of the Southern Hemisphere Ferrel cell.

The upper ocean meridional overturning circulation in MAR is characterized by a three-cell structure, with poleward surface flow in the Hadley and polar cell region, and equatorward surface flow in the region of the Ferrel cell (Fig. 3.6). The atmospheric wind forcing driving these Ekman cells is more vigorous in MAR than in PI (not shown). At latitudes with zero land-fraction and hence no obstruction to zonal ocean flow, i.e. poleward of 60° S and 35° N, the Ekman cells almost stretch to the ocean floor. Note that deep Ekman cells in the absence of zonal boundaries have been reported in aquaplanet simulations with coupled atmosphere-ocean general circulation models

(Smith et al. 2006; Marshall et al. 2007). They are a consequence of vanishing zonal pressure gradient and largely zonally-symmetric flow such that the return flow to the wind-generated meridional surface flow must be balanced by zonal momentum diffusion in the ocean interior and bottom friction at the ocean floor (Smith et al. 2006). The mid and deep ocean in MAR does not show the present-day structure of clockwise interhemispheric flow between 1 and 3 km and counterclockwise interhemispheric flow below. Instead, MAR exhibits a counterclockwise interhemispheric circulation below 500 m with downward motion between 30 and 50° S and upward motion within the deep Northern Hemisphere Ekman cell centered around 45° N. There is no significant clockwise flow in the deep ocean, i.e. no Marinoan correspondent to today's Antarctic Bottom Water cell. In MAR, vigorous circumpolar currents that reach 750 Sv in the Northern and 250 Sv in the Southern hemisphere develop (Fig. 3.7). They are in geostrophic balance with large meridional sea-level gradients around the sea-ice margin at 47° N/S. These gradients are consistent with strong meridional gradients of ocean potential temperature at these latitudes, a consequence of cooling the water column to close to the freezing point below sea ice. Subtropical ocean gyres with magnitudes larger than 50 Sv and western boundary intensification develop in MAR, similar to PI. Moreover, MAR exhibits weak tropical gyres, again akin to PI.

Compared to PI, total advective atmospheric heat transport in MAR is larger in the tropics but tends to be smaller in the extratropics (Fig. 3.8). The intensification of the mean meridional circulation is associated with an increase of its contribution to the atmospheric heat transport at almost all latitudes, which explains the stronger heat transport in the tropics. Heat transport by eddies increases in the Northern Hemisphere but decreases in the Southern Hemisphere, where it, together with the increased equatorward transport by the Ferrel cell, leads to reduced southward heat transport in MAR. Total implied ocean heat transport is weaker in MAR than in PI, except in Southern Hemisphere extratropics (Fig. 3.9). There, the loss of the northward ocean heat transport of PI around 45° S effects a stronger total ocean heat transport in MAR. The contribution of the meridional overturning circulation (MOC) is smaller in MAR. The MOC contribution around 30° N is northward in MAR, consistent with the strong and deep counterclockwise cell at this latitude. With this, the shape of the MOC contribution in MAR is reversed with respect to the equator compared to PI. The magnitude of the gyre contribution to ocean heat transport is similar in MAR and PI. Due to the changed geography, its latitudinal shape in MAR is however very different from that in PI.

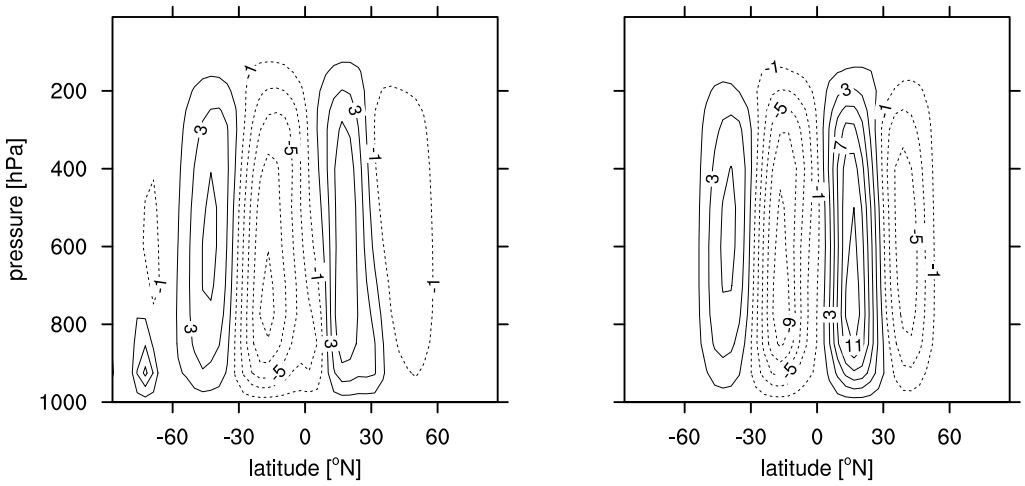

Figure 3.5: Atmospheric mass stream function in $10^{10}\,\mathrm{kgs}^{-1}$ for PI (left) and MAR (right). Contour interval is $2{\cdot}10^{10}\,\mathrm{kgs}^{-1}$, the zero contour line is omitted. Solid contours mean clockwise, dashed contours counterclockwise circulation. For MAR, years 3400 to 3499 are used.

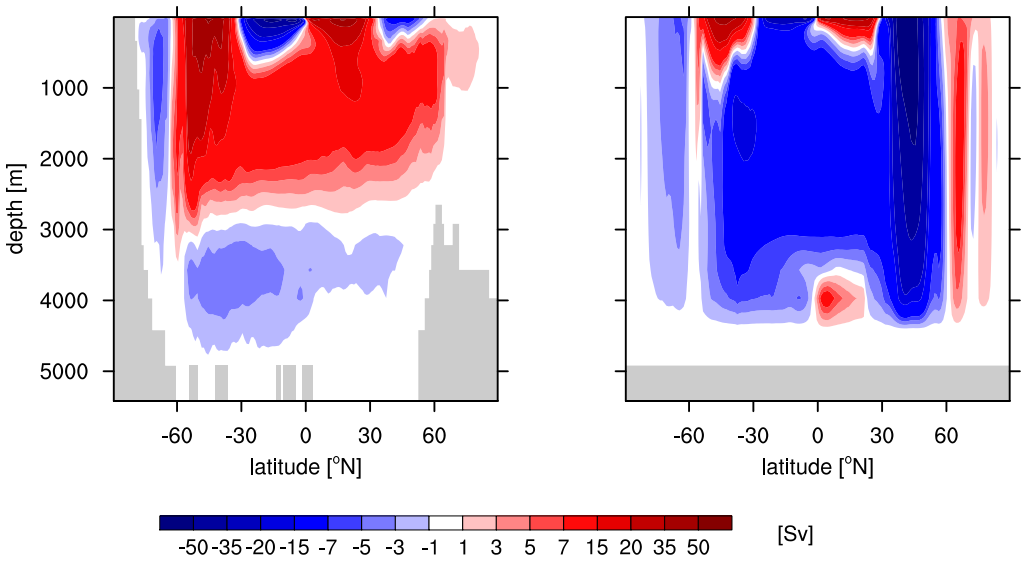

Figure 3.6: Global ocean meridional overturning circulation in Sv for PI (left) and MAR (right). Positive values mean clockwise motion, negative values counterclockwise motion. For MAR, years 3400 to 3499 are used. Note the uneven contour spacing.

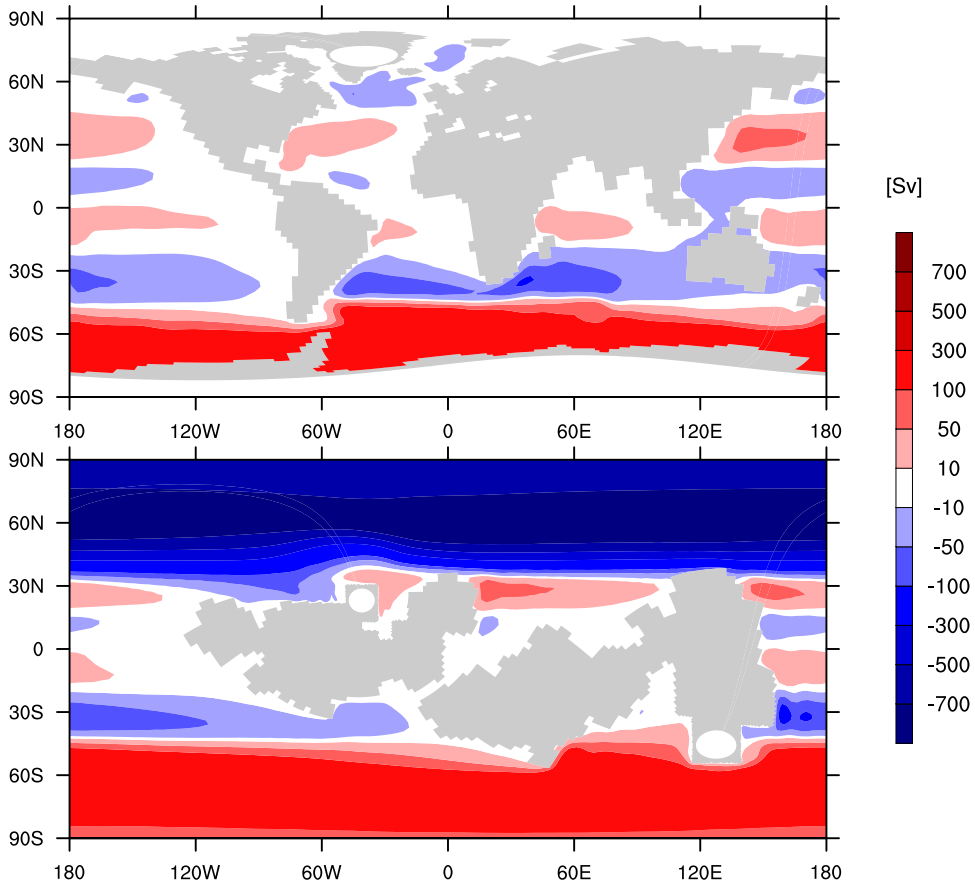

Figure 3.7: Barotropic stream function in Sv for PI (top) and MAR (bottom). A positive stream function difference between the start and end point of a straight line means that the mass transport across this line is to the right when the reader looks from start to end point. A negative stream function difference is to be understood analogously. Note the uneven contour spacing. For MAR, years 3400 to 3499 are used.

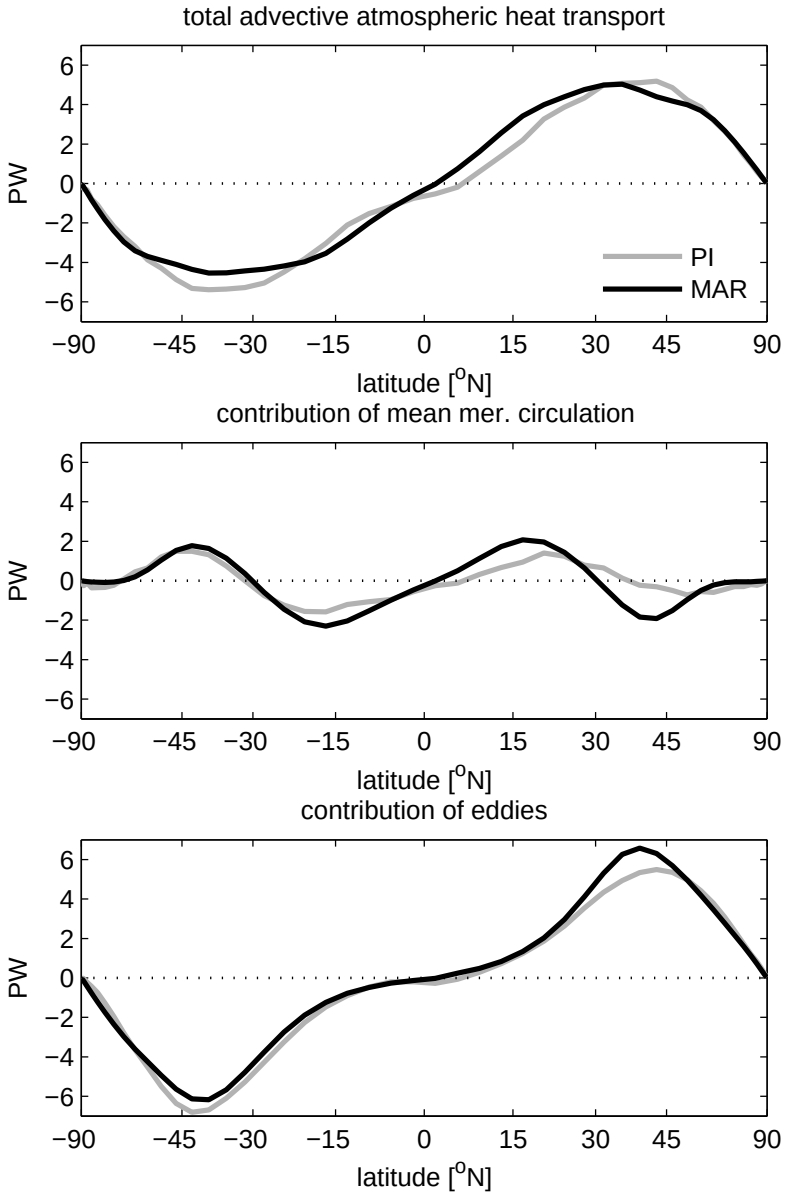

Figure 3.8: Total advective atmosphere heat transport (top) and contribution of the mean meridional circulation (middle) and eddies (bottom) for MAR (black) and PI (gray). For MAR, years 3400 to 3499 are used. The abscissae are linear in sine of latitude.

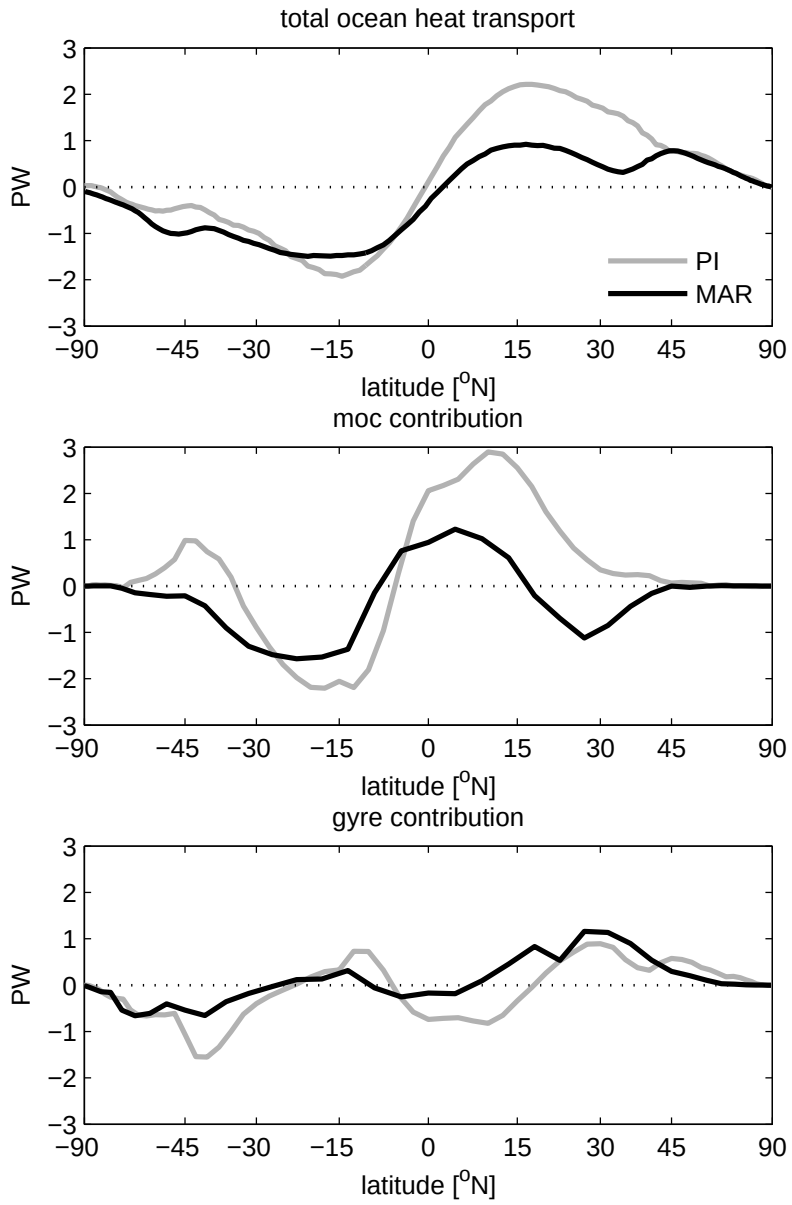

Figure 3.9: Total ocean heat transport (top) and contribution of the meridional overturning (middle) and gyre circulation (bottom) for MAR (black) and PI (gray). For MAR, years 3400 to 3499 are used. The abscissae are linear in sine of latitude.

3.3.3 One-dimensional energy balance model

To gain quantitative insight into how changes in radiation and heat transport contribute to the cold Marinoan control climate, we apply a one-dimensional energy balance model of zonal mean surface temperature. We adapt this technique from Heinemann et al. (2009), who used it to diagnose the causes of their simulated warm Paleocene-Eocene climate.

Assuming equilibrium and taking the zonal mean, net incoming shortwave radiation at the top of atmosphere must be balanced by outgoing longwave radiation and divergence of meridional heat transport at each latitude (Stone 1978), i.e.

$$(1 - \overline{\alpha}(\phi))\overline{Q}(\phi)) = \overline{I}(\phi) + \overline{H}(\phi) \tag{3.1}$$

with

$$\overline{H}(\phi) = \frac{1}{2\pi a^2 \cos\phi} \frac{\partial \overline{F}(\phi)}{\partial \phi}.$$

Here, $\overline{\alpha}$ denotes the planetary albedo, $\overline{Q}$ incoming shortwave radiation at the top of atmosphere, $\overline{I}$ outgoing longwave radiation, $\overline{H}$ divergence of time mean meridional heat transport $\overline{F}$; a is Earth's radius, ϕ is latitude. All quantities are understood as time and zonal mean values as indicated by the overbar. In what follows, we will drop the explicit notation of ϕ to improve readability.

If we parameterize $\overline{I}$ in terms of time and zonal mean effective emissivity $\overline{\epsilon}$ and time and zonal mean surface temperature $\overline{\tau}$,

$$\overline{I} = \sigma \overline{\epsilon} \overline{\tau}$$

with Stefan-Boltzmann constant $\sigma = 5.67 \cdot 10^{-8}\,\mathrm{Wm^{-2}K^{-4}}$, we can rewrite (3.1) as an equation for $\overline{\tau}$, and define this as the time and zonal mean surface temperature calculated by the one-dimensional energy balance model,

$$\overline{\tau}_{\mathrm{ebm}} \equiv \overline{\tau} = \sqrt[4]{\frac{1}{\sigma\overline{\epsilon}} \left\{ (1 - \overline{\alpha})\overline{Q} - \overline{H} \right\}}. \tag{3.2}$$

To use this equation as a diagnostic tool for surface temperature, we need to evaluate effective emissivity, planetary albedo, incoming shortwave radiation, and divergence of meridional heat transport from the general circulation model. This is done by calculating these terms as

$$\begin{aligned} \overline{\epsilon} &= \frac{\overline{I}}{\overline{I}_s^{\uparrow}}, \\ \overline{\alpha} &= \frac{\overline{Q}^{\uparrow}}{\overline{Q}}, \\ \overline{H} &= \overline{Q} - \overline{Q}^{\uparrow} - \overline{I}, \end{aligned} \tag{3.3}$$

where $\overline{I}_s^{\uparrow}$ is time and zonal mean longwave radiation emitted by the surface and $\overline{Q}^{\uparrow}$ the time and zonal mean shortwave radiation reflected by the planet. Both quantities are taken from the general circulation model output. Inserting (3.3) in (3.2) yields the one-dimensional energy balance model estimate for surface temperature, $\overline{\tau}_{\mathrm{ebm}}$.

The resulting surface temperature is very similar to that simulated by the general circulation model (see Fig. 3.10). This comes as no surprise. Inserting (3.3) on the r.h.s. of (3.2) yields

$$\begin{aligned}
\overline{\tau}_{\mathrm{ebm}} &= \sqrt[4]{\frac{1}{\sigma\tilde{\epsilon}}\left\{(1-\overline{\alpha})\overline{Q}-\overline{H}\right\}} \\
&= \sqrt[4]{\frac{\overline{I}_s^{\uparrow}}{\sigma\overline{I}}\left\{(1-\frac{\overline{Q}^{\uparrow}}{\overline{Q}})\overline{Q}-(\overline{Q}-\overline{Q}^{\uparrow}-\overline{I})\right\}} \\
&= \sqrt[4]{\frac{\overline{I}_s^{\uparrow}}{\sigma}}.
\end{aligned}$$

In the general circulation model, surface temperature and longwave radiation emitted by the surface at *each* time step t and grid point (λ,ϕ) are related by

$$I_s^{\uparrow}(t,\lambda,\phi) = \tilde{\epsilon}\sigma\tau_{\mathrm{gcm}}^4(t,\lambda,\phi), \tag{3.4}$$

with the close to unity constant $\tilde{\epsilon}$ taking into account the deviation of Earth's surface from a perfect black body. Note that in (3.4), $I_{\uparrow}^s(t,\lambda,\phi)$ and $\tau_{\mathrm{gcm}}^4(t,\lambda,\phi)$ are *not* time and zonal mean values. The surface temperature calculated by the energy balance model, $\overline{\tau}_{\mathrm{ebm}}$, therefore is related to the actual time and zonal mean surface temperature of the general circulation model via

$$\overline{\tau}_{\mathrm{ebm}} = \sqrt[4]{\tilde{\epsilon}}\sqrt[4]{\overline{\tau_{\mathrm{gcm}}^4(t,\lambda,\phi)}}.$$

The difference between the surface temperature diagnosed by the energy balance model and the time and zonal mean surface temperature of the general circulation model, $\overline{\tau}_{\mathrm{ebm}} - \overline{\tau}_{\mathrm{gcm}}$, consequently is, apart from the small and globally constant offset by $\sqrt[4]{\tilde{\epsilon}} \simeq 1$, only due to the non-permutability of taking the fourth root and taking the time and zonal mean,

$$\overline{\tau}_{\mathrm{ebm}} - \overline{\tau}_{\mathrm{gcm}} = \sqrt[4]{\tilde{\epsilon}}\sqrt[4]{\overline{\tau_{\mathrm{gcm}}^4(t,\lambda,\phi)}} - \overline{\tau_{\mathrm{gcm}}(t,\lambda,\phi)}.$$

In other words, the difference between the one-dimensional energy balance model and the general circulation model is only caused by time and zonal variations of surface temperature.

The one-dimensional energy balance barely helps to understand why a particular simulated climate is as warm or cold as it is. Its power lies in analyzing the reasons for

the surface temperature difference *between* two climate simulations by separating how much change of surface temperature is caused by changes in planetary albedo, effective emissivity, and meridional heat transport (for simplicity we here assume that incoming shortwave radiation at the top of atmosphere is the same in the two climate simulations; for MAR and PI this condition is fulfilled). This is done in the following way. Given PI and MAR, we calculate (3.3) for each simulation separately. Each simulation satisfies (3.2) with its respective set of diagnosed radiation and heat transport parameters,

$$\begin{aligned}\overline{\tau}_{\mathrm{ebm}}^{\mathrm{PI}} &= \sqrt[4]{\frac{1}{\sigma\overline{\epsilon}_{\mathrm{PI}}}\left\{(1-\overline{\alpha}_{\mathrm{PI}})\overline{Q}-\overline{H}_{\mathrm{PI}}\right\}},\\ \overline{\tau}_{\mathrm{ebm}}^{\mathrm{MAR}} &= \sqrt[4]{\frac{1}{\sigma\overline{\epsilon}_{\mathrm{MAR}}}\left\{(1-\overline{\alpha}_{\mathrm{MAR}})\overline{Q}-\overline{H}_{\mathrm{MAR}}\right\}}.\end{aligned}$$

Following Heinemann et al. (2009), we estimate the surface temperature change from PI to MAR caused by changes in planetary albedo by

$$\triangle\overline{\tau}\Big|_{\overline{\alpha}} = \sqrt[4]{\frac{1}{\sigma\overline{\epsilon}_{\mathrm{PI}}}\left\{(1-\overline{\alpha}_{\mathrm{MAR}})\overline{Q}-\overline{H}_{\mathrm{PI}}\right\}} - \overline{\tau}_{\mathrm{ebm}}^{\mathrm{PI}}.$$

The effect of changes in effective emissivity and divergence of meridional heat transport are given analogously by

$$\triangle\overline{\tau}\Big|_{\overline{\epsilon}} = \sqrt[4]{\frac{1}{\sigma\overline{\epsilon}_{\mathrm{MAR}}}\left\{(1-\overline{\alpha}_{\mathrm{PI}})\overline{Q}-\overline{H}_{PI}\right\}} - \overline{\tau}_{\mathrm{ebm}}^{\mathrm{PI}}$$

and

$$\triangle\overline{\tau}\Big|_{\overline{H}} = \sqrt[4]{\frac{1}{\sigma\overline{\epsilon}_{\mathrm{PI}}}\left\{(1-\overline{\alpha}_{\mathrm{PI}})\overline{Q}-\overline{H}_{\mathrm{MAR}}\right\}} - \overline{\tau}_{\mathrm{ebm}}^{\mathrm{PI}}.$$

This approach is justified by the fact that the sum of the individual estimates (see below) does nowhere deviate from the total temperature change by more than 0.2 K.

According to Fig. 3.10, the increased planetary albedo in MAR leads to a cooling compared to PI at all latitudes. The only exception is the South Pole region where the replacement of the Antarctic glacier by sea ice results in a slight decrease of surface albedo, which translates to a small planetary albedo warming effect. The sign of MAR - PI surface temperature changes induced by effective emissivity and meridional heat transport depend on latitude. In the tropics, reduced divergence of meridional heat transport and reduced effective emissivity have a warming effect in MAR compared to PI and offset a significant bit of the albedo induced cooling. In midlatitudes, planetary albedo, effective emissivity and meridional heat transport all contribute to the simulated cooling in MAR, with nearly equal partitioning between the three in the Southern Hemisphere. In Northern Hemisphere polar latitudes, the cooling in MAR is equally

generated by higher planetary albedo and higher effective emissivity with heat transport changes only becoming important close to the North Pole. This picture is similar for Southern Hemisphere polar latitudes north of today's Antarctic continent. Close to the South Pole, increased effective emissivity and convergence of meridional heat transport result in a warming, similar to planetary albedo.

The global cooling effect of planetary albedo changes is consistent with what one expects from clustering continents with comparably high surface albedo in the tropics and increasing sea-ice cover in the extratropics. The tropical warming effect of effective emissivity changes is counter to the expected effect of the strong reduction of water vapor in MAR and hence must be related to clouds. Moreover, it is unclear from this analysis whether, for example, the tropical warming effect of heat transport changes is due to changes in atmosphere or ocean (including sea-ice) heat transport. To answer these issues, the above diagnostics are expanded to separate cloud and clear-sky radiative effects as well as the effects of atmosphere and ocean heat transports.

The temperature effect of cloud changes is isolated from that of surface albedo changes, in the case of planetary albedo, and water vapor changes, in the case of effective emissivity, by virtue of full-sky and clear-sky radiative fluxes. The time and zonal mean planetary albedo can be decomposed into the clear-sky planetary albedo $\overline{\alpha}_{cs}$, which to good approximation equals surface albedo, and the contribution of clouds to planetary albedo, $\overline{\alpha}_{cl}$,

$$\overline{\alpha} = \overline{\alpha}_{cs} + \overline{\alpha}_{cl}.$$

Note that $\overline{\alpha}_{cl}$ does not equal the cloud albedo but measures the importance of clouds for planetary albedo. In an analogous manner, effective emissivity is split into clear-sky emissivity, $\overline{\epsilon}_{cs}$, mainly depending on water vapor content, and again cloud contribution, $\overline{\epsilon}_{cl}$,

$$\overline{\epsilon} = \overline{\epsilon}_{cs} + \overline{\epsilon}_{cl}.$$

Clear-sky albedo and effective emissivity are diagnosed from the general circulation model as

$$\begin{aligned} \overline{\epsilon}_{cs} &= \frac{\overline{I}_{cs}}{\overline{I}_s^{\uparrow}}, \\ \overline{\alpha}_{cs} &= \frac{\overline{Q}_{cs}^{\uparrow}}{\overline{Q}}, \end{aligned}$$

with subscript *cs* meaning that now clear-sky radiative fluxes are used. The cloud contributions are calculated as residuals between full-sky and clear-sky values. Atmosphere and ocean meridional heat transport divergences are separated by means of the the time and zonal mean surface heat flux $\overline{V}_s$, which is computed from the general circulation model as the time and zonal mean sum of surface shortwave and longwave radiation

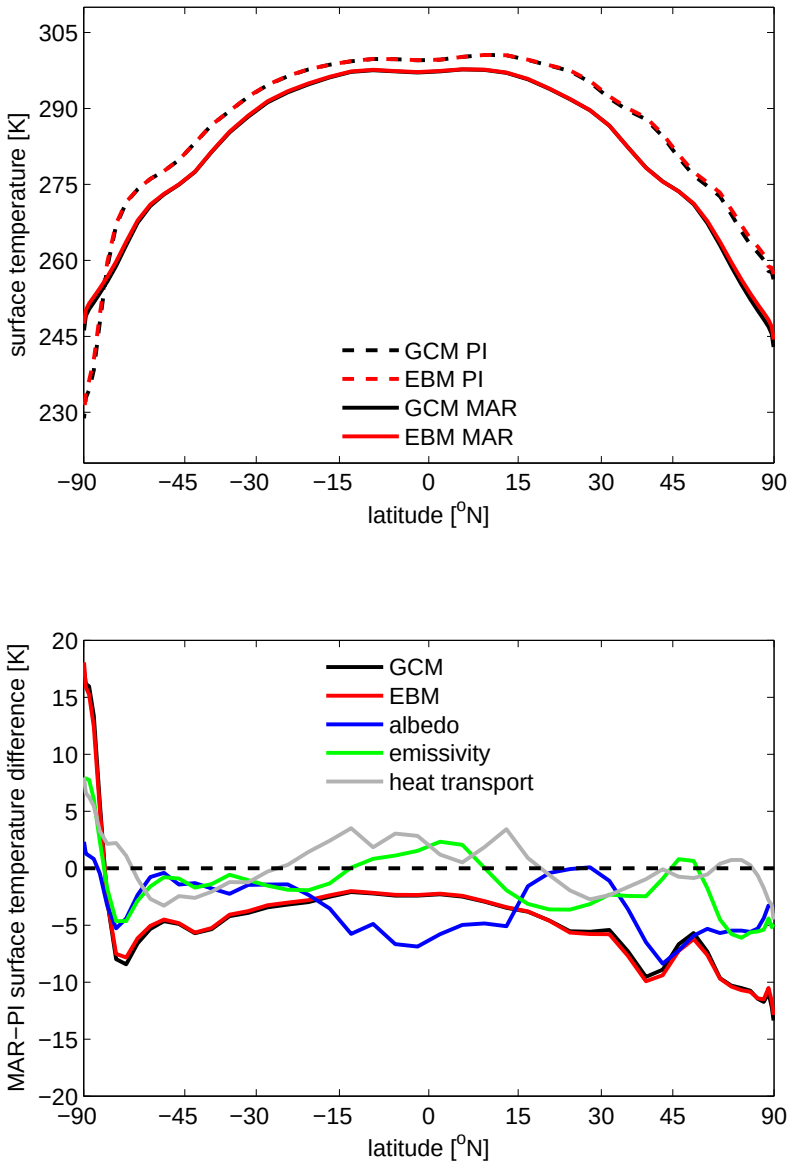

Figure 3.10: Top: Time and zonal mean surface temperature of MAR (solid) and PI (dashed) as simulated by the general circulation model (black) and diagnosed by the one-dimensional energy balance model (red). Bottom: difference of time and zonal mean surface temperature between MAR and PI as simulated by the general circulation model (black) and diagnosed by the one-dimensional energy balance model (red). The other solid lines show the MAR-PI surface temperature differences attributed to changes in planetary albedo (blue), effective emissivity (green), and heat transport (gray). The abscissa is linear in sine of latitude.

fluxes, the sensible heat flux, and the latent heat flux. With this, the meridional heat transport divergence due to the atmosphere is given by

$$\overline{H}_a = \overline{H} - \overline{V}_s,$$

and that due to the ocean (including sea-ice) by

$$\overline{H}_o = \overline{H} - \overline{H}_a = \overline{V}_s.$$

The effect of clear-sky albedo changes between MAR and PI on surface temperatures is calculated as for planetary albedo but with cloud contribution kept at its PI value, i.e.

$$\triangle\overline{\tau}\Big|_{\overline{\alpha}_{cs}} = \sqrt[4]{\frac{1}{\sigma\overline{\epsilon}_{\mathrm{PI}}}\left\{(1-\overline{\alpha}_{cs,\mathrm{MAR}}-\overline{\alpha}_{cl,\mathrm{PI}})\overline{Q}-\overline{H}_{\mathrm{PI}}\right\}} - \overline{\tau}^{\mathrm{PI}}_{\mathrm{ebm}}.$$

For the effect of planetary albedo changes due to cloud changes, we have

$$\triangle\overline{\tau}\Big|_{\overline{\alpha}_{cl}} = \sqrt[4]{\frac{1}{\sigma\overline{\epsilon}_{\mathrm{PI}}}\left\{(1-\overline{\alpha}_{cs,\mathrm{PI}}-\overline{\alpha}_{cl,\mathrm{MAR}})\overline{Q}-\overline{H}_{\mathrm{PI}}\right\}} - \overline{\tau}^{\mathrm{PI}}_{\mathrm{ebm}}.$$

The effect of changes in clear-sky effective emissivity, cloud contribution to effective emissivity, and meridional heat transport divergence due to atmosphere and ocean are computed analogously.

Changes in clear-sky planetary albedo lead to cooling in MAR everywhere except in Northern midlatitudes, where the reduced land fraction in MAR compared to PI effects a decreased surface albedo and hence decreased clear-sky planetary albedo (Fig. 3.11). The temperature effect of changes in the cloud contribution is opposite to the temperature effect of changes in clear-sky planetary albedo. At most latitudes, clouds contribute less to planetary albedo in MAR than in PI because of the increased surface albedo in MAR (see Fig. 3.4). This translates to a warming effect of the cloud contribution. In Northern midlatitudes, however, the decreased surface albedo in MAR effects that clouds can contribute more to planetary albedo in MAR than in PI. Supported by the increased cloud cover at these latitudes in MAR (see Fig. 3.4), this means that changes in the cloud contribution to planetary albedo have a cooling effect in Northern midlatitudes. This cooling is even larger than the warming due to increased clear-sky surface albedo such that also in Northern midlatitudes, planetary albedo in MAR is higher than in PI, implying a cooling effect by increased planetary albedo. For effective emissivity, clear-sky emissivity is higher in MAR than PI, consistent with the reduction in water vapor content (cf. Fig. 3.12). Clear-sky effective emissivity changes therefore have a cooling effect in MAR, except close to the South Pole. Cloud changes mainly have a warming effect, such that the overall surface temperature decrease from PI to MAR due to changing effective emissivity is smaller than that from reduced water vapor content alone. In the tropics, cloud warming even offsets the cooling by increased

clear-sky effective emissivity, showing that the tropical warming effect of changes in effective emissivity is caused by cloud changes. Surface temperature changes attributed to changes of total meridional heat transport result from strong and largely opposite changes in atmosphere and ocean heat transports. In the tropics, the warming effect is caused by less divergence of ocean heat transport, visible in a flatter shape of tropical total implied ocean heat transport in MAR compared to PI (Fig. 3.13). This seems plausible from a smaller tropical ocean fraction in MAR. The most pronounced change of surface temperature due to changes in ocean heat transport is a 17 K cooling around 35° N. This strong local cooling effect is related to a drastic change in the ocean meridional overturning circulation around 35° N in MAR compared to PI (see above). Changes of atmospheric heat transport, however, offset this cooling almost completely. That large temperature changes attributed to changes in atmosphere and ocean heat transport mainly compensate can be understood from the fact that the divergence of total meridional heat transport, or equivalently the sum of shortwave and longwave radiation at the top of atmosphere, has an as gentle shape in MAR as in PI.

Finally, we quantify the changes of planetary albedo, effective emissivity and heat transport contribute to the total change of global mean surface temperature. This is done by meridionally averaging the latitudinal contributions (Tab. 3.4). We find that two thirds of the global mean cooling of 4.6 K from PI to MAR are caused by increased planetary albedo and the remaining one third by increased effective emissivity, that is a weaker greenhouse effect. Clouds reduce the cooling that would result from the expansion of sea ice and the reduction of water vapor alone. This does not imply a positive total cloud radiative forcing in MAR, but means that total cloud radiative forcing is less negative in MAR than in PI (see Tab. 3.3). The global mean temperature change due to changes in the divergence of heat transport is negligible.

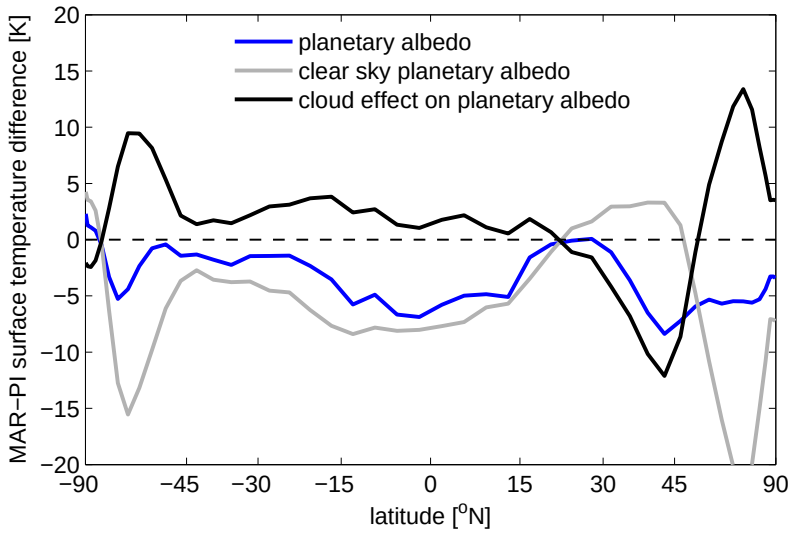

Figure 3.11: MAR-PI surface temperature differences attributed to changes in planetary albedo (blue), clear-sky planetary albedo (gray), and the effect of clouds on planetary albedo (black). The abscissa is linear in sine of latitude.

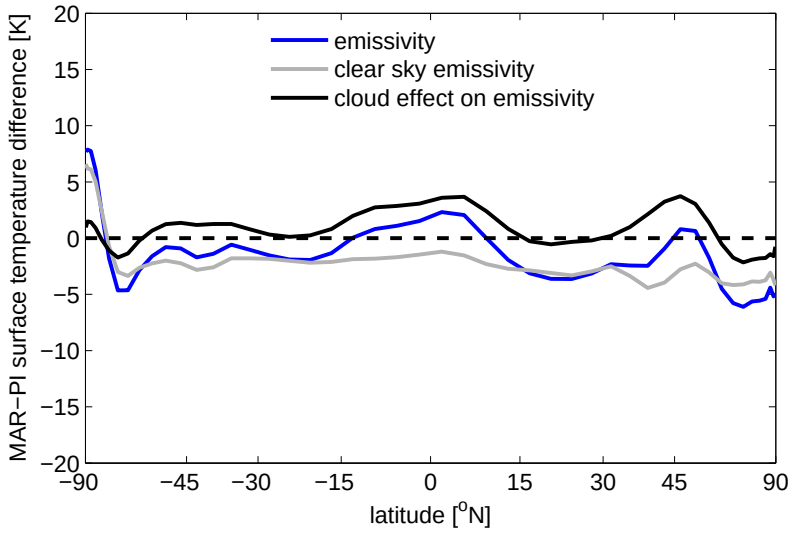

Figure 3.12: MAR-PI surface temperature differences attributed to changes in effective emissivity (blue), clear-sky effective emissivity (gray), and the effect of clouds on effective emissivity (black). The abscissa is linear in sine of latitude.

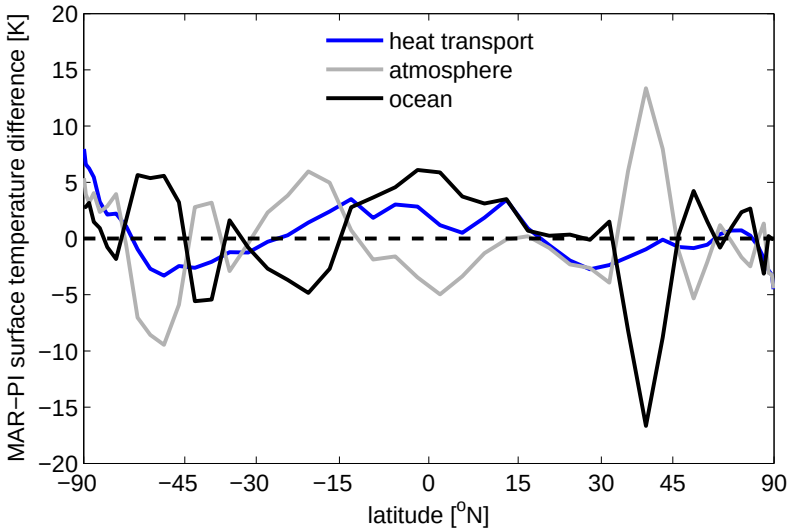

Figure 3.13: MAR-PI surface temperature differences attributed to changes in the divergence of total meridional heat transport (blue), atmospheric meridional heat transport (gray), and oceanic meridional heat transport including sea ice (black). The abscissa is linear in sine of latitude.

Table 3.4: Global mean surface temperature difference between the Marinoan (MAR) and pre-industrial (PI) control simulation as diagnosed by the one-dimensional energy balance model.

		$\triangle\tau$
global		-4.6 K
planetary albedo	total	-3.5 K
	clear sky	-5.5 K
	cloud effect	1.6 K
effective emissivity	total	-1.3 K
	clear sky	-2.3 K
	cloud effect	1.0 K
heat transport	total	0.2 K
	atmosphere	-0.2 K
	ocean (incl. sea ice)	0.2 K

3.4 Snowball Earth bifurcation point and maximum stable sea-ice cover

This sections reports on the effect of an abrupt decrease of total solar irradiance and, for some simulations, simultaneous increase of atmospheric carbon dioxide. These simulations enable us to find the Snowball Earth bifurcation point as well as the maximum stable sea-ice cover.

Virtually switching off the sun results in global sea-ice cover within 9 years (simulation TSI00, not shown). A reduction of TSI to 94% of its present-day value leads to a Snowball Earth within 354 years (simulation TSI94, see Fig. 3.14). In TSI94, the sea-ice line is nearly symmetric about the equator during the entire transition, and snow accumulates in the Southern but not in the Northern Hemisphere. While surface albedo increases in the Northern Hemisphere are hence solely due to the conversion of open ocean areas to sea ice, snow accumulation on land contributes to surface albedo increases in the Southern Hemisphere. The surface albedo of the Southern Hemisphere consequently increases at the same rate as the Northern Hemisphere surface albedo, and meridional heat transports stay symmetric about the equator during the entire transition (not shown). This is in contrast to the initiation of a modern Snowball Earth (Voigt and Marotzke 2009), where the asymmetric distribution of continents between the Northern and Southern Hemisphere, combined with virtually zero snow-accumulation on land, caused a much faster increase of surface albedo in the Southern Hemisphere than in the Northern Hemisphere, and by this strong heat transport toward the more water-covered Southern hemisphere as sea ice spread towards the equator.

In contrast to a reduction of TSI to 94%, decreasing TSI to 96% does not effect global sea-ice cover (simulation TSI96). Sea-ice expansion in this simulation is initially almost as fast as for a TSI reduction to 94%, but decelerates 250 years after the TSI decrease. A further 1000 years later, sea-ice area stabilizes at $20{\cdot}10^{13}$ m^2, equivalent to 55% of the Marinoan ocean surface area. To further pin down the Marinoan Snowball Earth bifurcation point, we branch off simulation TSI-955 from year 5799 of TSI96. In this simulation, total solar irradiance is additionally decreased by 6.8 Wm^{-2} to 95.5% of its present-day value. This small additional TSI reduction is sufficient to induce global sea-ice cover within 200 years. The Snowball Earth bifurcation point, for pre-industrial levels of carbon dioxide, therefore is between 95.5 and 96% of the present-day total solar irradiance.

That we are able to fix the Snowball Earth bifurcation within an uncertainty of 0.5% of the present-day TSI also enables us to infer the maximum stable sea-ice area. As shown by TSI96, sea ice can cover 55% of the ocean surface area without triggering a climate instability. At the end of TSI96, the sea-ice line has stabilized at 30° N and around 25° S, respectively (Fig. 3.15), with sea-ice being snow-covered except very close to the sea-ice edge, and snow on land restricted to largely thin snow cover in the

southernmost parts of Gondwana. The strong sensitivity of this sea-ice line to the small reduction in TSI demonstrates that equilibrium solutions with sea-ice cover above 55% are highly unlikely, or if they occur, highly unstable.

Falling into a Snowball Earth when TSI is reduced to 94% is prevented by an appropriate increase in atmospheric carbon dioxide. Combining a reduction of TSI to 94% with a quadrupling of atmospheric carbon dioxide with respect to its pre-industrial level results in an increase of the sea-ice area to $14{\cdot}10^{13}$ m^2, corresponding to 37% of the Marinoan ocean surface area (simulation TSI94-4CO2). Therefore, for total solar irradiance at 94% of its present-day value, i.e. the value commonly assumed for the Marinoan, the Snowball Earth bifurcation is between one and four times the pre-industrial concentration of carbon dioxide. Increasing carbon dioxide even further to 6 times its pre-industrial level almost compensates for the decrease of TSI to 94% (simulation TSI94-6CO2). After 1000 years, sea-ice area in this case is only slightly higher than in the control simulation MAR though ocean potential temperatures still decline.

Reducing TSI to 94% and quadrupling carbon dioxide has almost the same effect on sea-ice area as reducing TSI to 98%. This is consistent with the fact that the radiative forcing of increasing TSI by 4% and assuming a planetary albedo of 0.353 as simulated for MAR,

$$\mathrm{RF}(4\%\mathrm{TSI}_0) = (1 - 0.353) \cdot 0.04 \frac{1367}{4}\,\mathrm{Wm}^{-2} = 8.8\,\mathrm{Wm}^{-2},$$

is close to the radiative forcing of quadrupling carbon dioxide (Myhre et al. 1998),

$$\mathrm{RF}(4 \times \mathrm{CO}_2) = 5.35 \ln 4\ \mathrm{Wm}^{-2} = 7.4\ \mathrm{Wm}^{-2}.$$

Note that if we took into account that the planetary albedo increases in the course of TSI98 and TSI94-4CO2, we would obtain a slightly lower radiative forcing estimate for the 4% reduction in TSI, bringing the two estimates closer together. Moreover, the factor of 5.35 used in the radiative forcing estimate of quadrupling carbon dioxide is valid for present-day conditions but might be different for the Marinoan.

Simulation TSI100 is started from year 3999 of TSI94 with TSI set back to 100%. As one expects, this 6% increase does not lead to Snowball Earth deglaciation and sea-ice cover remains global in TSI100 (not shown). This establishes that, akin to present-day conditions (Marotzke and Botzet 2007), ECHAM5/MPI-OM exhibits bistability for TSI at its present-day value also in the Marinoan setup.

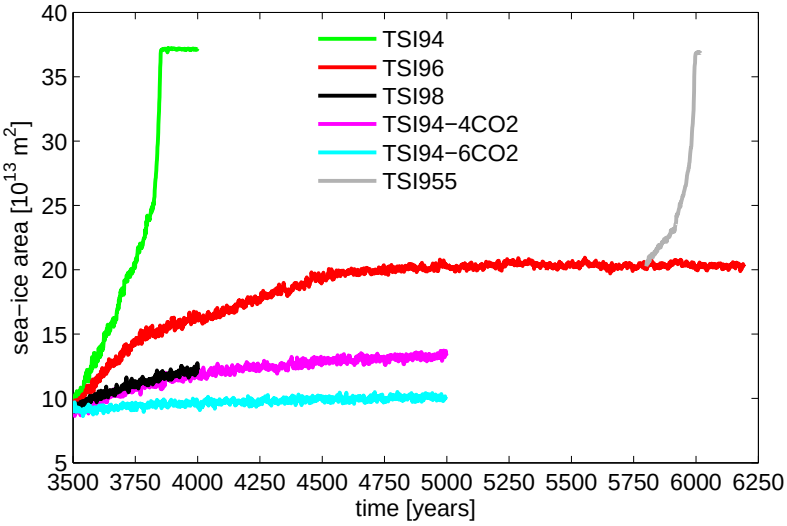

Figure 3.14: Time evolution of annual mean global sea-ice area as a response to an abrupt decrease of total solar irradiance (TSI) and, for some simulations, simultaneous increase of atmospheric carbon dioxide.

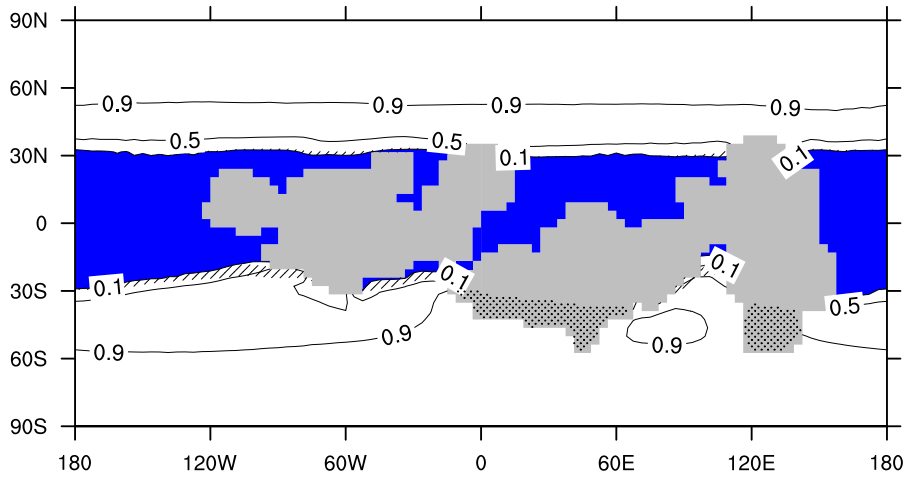

Figure 3.15: Sea-ice fraction of simulation TSI96 averaged over years 6000 to 6199. Contour spacing is 0.4. Open water, defined by sea-ice fraction below 0.1 for this plot, is shown in blue. Areas with snow cover on sea-ice below 0.01 m water equivalent depth are shaded. Snow cover on land with depth above 0.01 m water equivalent are stippled.

3.5 Prediction of the Snowball Earth bifurcation point and transition times by a zero-dimensional energy balance model

For the initiation of a modern Snowball Earth, Voigt and Marotzke (2009) showed that the Snowball Earth bifurcation point estimated with the atmosphere-ocean general circulation model and the transition times are well reproduced by a zero-dimensional energy balance model (EBM) of global mean ocean potential temperature. In Voigt and Marotzke (2009), however, the Snowball Earth bifurcation point was only established within an accuracy of 3% of the present-day total solar irradiance. This raises the question if this EBM still agrees with the here much more precise estimate of the bifurcation point for Marinoan surface boundary conditions.

We start with a review of the EBM described in Voigt and Marotzke (2009), including the details of solving the model and determining its parameters. The latter were not given in Voigt and Marotzke (2009). By neglecting atmosphere and land and considering the ocean to be perfectly mixed, the EBM predicts the evolution of mean ocean potential temperature θ in response to a decrease in total solar irradiance according to

$$c\frac{d\theta}{dt} = \frac{(1-\alpha)}{4}\mathrm{TSI} - \epsilon\sigma\theta^4. \tag{3.5}$$

Here, $c = 1.52 \cdot 10^{10}\,\mathrm{JK^{-1}m^{-2}}$ denotes the ocean heat capcity per unit surface area, and $\sigma = 5.67 \cdot 10^{-8}$ the Stefan-Boltzmann constant. The parameter α can be thought of as the global mean planetary albedo while ϵ takes into account the greenhouse effect. Eq. (3.5) can be integrated by separation of variables and the help of an integral table (Bronstein 1996) to yield an implicit equation for θ at time t after the abrupt reduction of solar irradiance from TSI_0=1367 $\mathrm{Wm^{-2}}$ to TSI<TSI_0 at $t = 0$,

$$\frac{1}{4(\beta\,\mathrm{TSI})^{3/4}}\ln\left|\frac{(\beta\,\mathrm{TSI})^{1/4}+\theta(t,\mathrm{TSI})}{(\beta\,\mathrm{TSI})^{1/4}-\theta(t,\mathrm{TSI})}\right| + \frac{1}{2(\beta\,\mathrm{TSI})^{3/4}}\arctan\left\{\frac{\theta(t,\mathrm{TSI})}{(\beta\,\mathrm{TSI})^{1/4}}\right\} = \gamma(t+\delta)$$

The transition to a Snowball Earth in the EBM is accomplished as soon as θ drops to the freezing temperature of sea water, $\theta_f = 271.25\,\mathrm{K}$. The transition time to a Snowball Earth is therefore given by the time $t_f(\mathrm{TSI})$ at which $\theta = \theta_f$,

$$t_f(\mathrm{TSI}) = \frac{1}{4\gamma(\beta\,\mathrm{TSI})^{3/4}}\ln\left|\frac{(\beta\,\mathrm{TSI})^{1/4}+\theta_f}{(\beta\,\mathrm{TSI})^{1/4}-\theta_f}\right| + \frac{1}{2\gamma(\beta\,\mathrm{TSI})^{3/4}}\arctan\left\{\frac{\theta_f}{(\beta\,\mathrm{TSI})^{1/4}}\right\} - \delta. \tag{3.6}$$

To apply (3.6) in practice, we need to determine the parameters β, γ, and δ. The latter, δ, is defined by the initial condition that at the instant of TSI reduction, $t = 0$, the ocean potential temperature equals the equilibrium ocean potential temperature

for today's total solar irradiance, i.e. $\theta(0, \mathrm{TSI}) = \theta_{\mathrm{MAR}} = 274.3\,\mathrm{K}$. This yields

$$\delta(\mathrm{TSI}) = \frac{1}{\gamma}\left\{\frac{1}{4(\beta\,\mathrm{TSI})^{3/4}}\ln\left|\frac{(\beta\,\mathrm{TSI})^{1/4}+\theta_{\mathrm{MAR}}}{(\beta\,\mathrm{TSI})^{1/4}-\theta_{\mathrm{MAR}}}\right| + \frac{1}{2(\beta\,\mathrm{TSI})^{3/4}}\arctan\left\{\frac{\theta_{\mathrm{MAR}}}{(\beta\,\mathrm{TSI})^{1/4}}\right\}\right\}.$$

The parameter β abbreviates

$$\beta = \frac{1-\alpha}{4\sigma\epsilon}$$

and is determined by the tuneable ratio of $1-\alpha$ and ϵ. This ratio is fixed by requiring that the Marinoan control climate is an equilibrium solution of (3.5),

$$\frac{1-\alpha}{\epsilon} = 4\sigma\frac{\theta_{\mathrm{MAR}}^4}{\mathrm{TSI}_0} \simeq 0.9392. \tag{3.7}$$

For the parameter γ, which is an abbreviation for

$$\gamma = \frac{\sigma\epsilon}{c},$$

we need to evaluate ϵ. This is done by demanding that the EBM reproduces the 9 year transition time of the atmosphere-ocean general circulation model for virtually switching off the sun (simulation TSI00). In this case, the TSI term drops out of (3.5) and, after some algebra, we obtain

$$\epsilon = \frac{c}{3\sigma t_f(\mathrm{TSI00})}\left\{\frac{1}{\theta_f^3} - \frac{1}{\theta_{\mathrm{MAR}}^3}\right\} = 0.5200,$$

where $t_f(\mathrm{TSI00}) = 9\,\mathrm{a}$.

By construction, the transition time of the EBM agrees with that of the general circulation model for TSI set to virtually zero (Fig. 3.16). For TSI set to 94% of its present-day value the EBM slightly underestimates the transition time; the EBM gives 264 years instead of the 354 years found with the atmosphere-ocean general circulation model (simulation TSI94). For $\mathrm{TSI} \geq 1307\,\mathrm{Wm}^{-2} = 95.63\%\,\mathrm{TSI}_0$ global mean ocean potential temperature in the EBM never falls below the freezing point of sea water. The EBM therefore estimates the Snowball Earth bifurcation point to $95.63\%\,\mathrm{TSI}_0$. This is in intriguing agreement with the 95.5 to 96% range found with the atmosphere-ocean general circulation model.

Since the estimate of the Snowball Earth bifurcation point is defined as the total solar irradiance TSI_c needed to cool θ to θ_f in the limit $t \to \infty$, examining the individual terms of the r.h.s. of (3.6) gives a formula for the EBM's estimate of the Snowball Earth bifurcation point. Obeying that $\beta, \gamma, \delta, \mathrm{TSI}, \theta_f$, and the arctan-term are all finite, we see that the only way to generate an infinity on the r.h.s. of (3.6) is through

$$(\beta\,\mathrm{TSI}_c)^{1/4} - \theta_f = 0. \tag{3.8}$$

The EBM's estimate of the Snowball Earth bifurcation point is therefore determined by

$$\mathrm{TSI}_c = \frac{\theta_f^4}{\beta} = \left(\frac{\theta_f}{\theta_{\mathrm{MAR}}}\right)^4 \mathrm{TSI}_0. \tag{3.9}$$

TSI_c is completely fixed by the equilibrium global mean ocean potential temperature for today's total solar irradiance. The warmer the control climate for TSI_0, the larger the TSI reduction needed for Snowball Earth initiation. This was already mentioned by Voigt and Marotzke (2009), but we here demonstrate this fact explicitly.

Estimating the Snowball Earth bifurcation point actually does not require to calculate the time-evolution of $\theta(t, \mathrm{TSI})$. Since in the limit $t \to \infty$ the EBM approaches equilibrium, TSI_c is constrained by

$$\frac{(1-\alpha)}{4}\mathrm{TSI}_c = \epsilon\sigma\theta_f^4 \tag{3.10}$$

This again yields

$$\mathrm{TSI}_c = \frac{4\epsilon\sigma}{(1-\alpha)}\theta_f^4 = \left(\frac{\theta_f}{\theta_{\mathrm{MAR}}}\right)^4 \mathrm{TSI}_0.$$

What ultimately only is important for the EBM's estimate of the Snowball Earth bifurcation point is the assumption that the ratio $(1-\alpha)/\epsilon$ is the same for TSI_0 and TSI_c, and all TSI values in between. Since a TSI reduction triggers sea-ice expansion and by this an increased planetary albedo, this assumption implies a decrease of ϵ with reduced TSI. At first glance, the latter seems incompatible with decreased atmospheric water-vapor in a colder climate. However, this conflict is dissolved by acknowledging that in order to compare the EBM parameter ϵ with the effective emissivity ϵ_{gcm} that is diagnosed from the atmosphere-ocean general circulation model, we need to incorporate the formfactor $(\mathrm{SST}/\theta)^4$ (Voigt and Marotzke 2009). This factor takes into account that the EBM parameterizes longwave radiation energy loss through the global mean ocean potential temperature instead of global mean sea surface temperature SST. This yields

$$\epsilon = \epsilon_{\mathrm{gcm}} \left(\frac{\mathrm{SST}}{\theta}\right)^4.$$

While the effective emissivity ϵ_{gcm} increases with decreased TSI, the EBM parameter ϵ can still decrease because decreased TSI also reduces ocean stratification (Voigt and Marotzke 2009). This justifies the assumption that the ratio $(1-\alpha)/\epsilon$ stays constant when TSI is reduced to or above the Snowball Earth bifurcation point TSI_c.

Finally, the fact that the considered values of θ are close to θ_f suggests to linearize (3.5) at θ_f. Doing so allows us to derive a much simpler but essentially as good estimate for the transition times as obtained by solving the non-linear equation (3.5). If we write

$$\theta(t, \mathrm{TSI}) = \theta_f + T(t, \mathrm{TSI}),$$

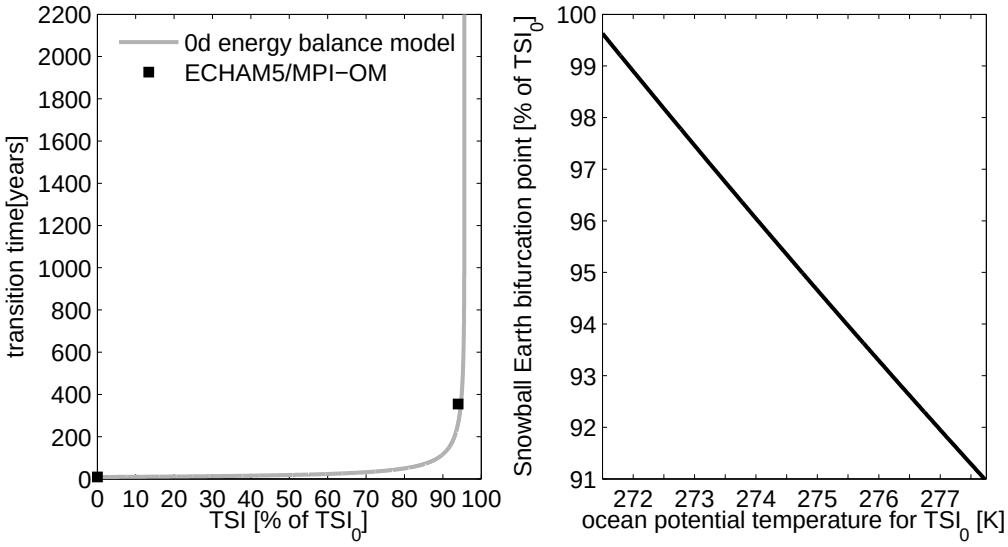

Figure 3.16: Left: transition time to a Snowball Earth in dependence of total solar irradiance as estimated with the zero-dimensional energy balance model of mean ocean potential temperature (gray) and found with ECHAM5/MPI-OM (black squares). Total solar irradiance is given in percentage of its present-day value TSI_0. Right: prediction of the Snowball Earth bifurcation point by the zero-dimensional energy balance model in dependence of equilibrium mean ocean potential temperature for present-day TSI.

where T denotes the deviation of global mean ocean potential temperature from the freezing point of sea water, (3.5) becomes an ordinary linear differential equation in T,

$$\tau \frac{dT}{dt}(t, \mathrm{TSI}) = T_r(\mathrm{TSI}) - T(t, \mathrm{TSI}), \tag{3.11}$$

with

$$\tau = \frac{c}{4\sigma\epsilon\theta_f^3}$$

and

$$T_r(\mathrm{TSI}) = \frac{1-\alpha}{16\sigma\epsilon\theta_f^3}\mathrm{TSI} - \frac{\theta_f}{4}.$$

We fix T_r by (3.7). This means that $T_{\mathrm{MAR}} = \theta_{MAR} - \theta_f$ is not a strict equilibrium solution of the linearized EBM (3.11) for TSI_0. However, it is readily shown that $dT_{\mathrm{MAR}}/dt(t, \mathrm{TSI}_0)$ with this choice of T_r only contains terms that are of quadratic or higher order in T_{MAR}, making clear that T_{MAR} is an equilibrium solution of the linearized EBM within the validity of the linear approximation. τ is fixed by setting ϵ to the effective emissivity of MAR, $\epsilon_{\mathrm{MAR}} = 0.594$. Incorporating the initial condition

$T(t = 0, \mathrm{TSI}) = T_{\mathrm{MAR}}$, (3.11) is solved by

$$T(t, \mathrm{TSI}) = T_r(\mathrm{TSI}) + \{T_{\mathrm{MAR}} - T_r(\mathrm{TSI})\} \exp(-t/\tau).$$

The transition time to a Snowball Earth estimated with the linearized EBM, $t_f^{lin}(\mathrm{TSI})$, is defined by $T(t_f, \mathrm{TSI}) = 0$. We obtain

$$t_f^{lin}(\mathrm{TSI}) = \tau \ln \frac{T_r(\mathrm{TSI}) - T_{\mathrm{MAR}}}{T_r(\mathrm{TSI})}.$$

For switched-off sun, the linearised EBM gives a transition time of 8 years. This is in very good agreement with the GCM, in particular since no explicit tuning of ϵ is applied for the linear EBM. The transition time for TSI=94% TSI_0 is 232 years, slightly less than the estimate of 264 years of the non-linear EBM. When plotted in Fig. 3.16, the transition time of the linear EBM would be indistinguishable from that of the non-linear EBM.

3.6 Energy fluxes at the top of atmosphere and at the surface

For an atmosphere in equilibrium, energy conservation requires that the global mean energy flux at the top of atmosphere, F_{toa}, given by the sum of net incoming shortwave radiation and outgoing longwave radiation, equals the global mean energy flux at the surface F_{sfc}, the latter given by the sum of surface shortwave and longwave radiation and latent and sensible heat fluxes.

We have checked to which degree this is fullfilled in our simulations. For the Marinoan control simulation MAR, the top of atmosphere energy flux is $0.7\,\mathrm{Wm}^{-2}$ larger than the surface energy flux (Fig. 3.17). This imbalance is close to the $0.5\,\mathrm{Wm}^{-2}$ imbalance that we find for the pre-industrial control simulation PI.

In contrast, the top of atmosphere and the surface energy fluxes differ much more in an equilibrium Snowball Earth state. For example, when total solar irradiance is set to 94% of its today's value, the imbalance amounts to -5 Wm^{-2} (Fig. 3.17). Now, the atmosphere loses more energy at the top of atmosphere than it gains at the surface, suggesting that an artificial energy source exists in the atmosphere model. If we use the global integral of atmospheric energy content of today's atmosphere, $H_{\mathrm{atm}} = 256 \cdot 10^7\,\mathrm{Jm}^{-2}$ (Peixoto and Oort 1992), as an estimate for atmospheric energy content of the equilibrium Snowball Earth atmosphere, we find that this imbalance accumulates to the total atmospheric energy content within

$$\frac{H_{\mathrm{atm}}}{F_{\mathrm{toa}} - F_{\mathrm{sfc}}} \simeq 16\,\mathrm{a}.$$

The reason for the much larger imbalance in an equilibrium Snowball Earth is obscure to us, as well as the reason why the imbalance changes sign from the control simulations MAR and PI to the equilibrium simulation of a Snowball Earth.

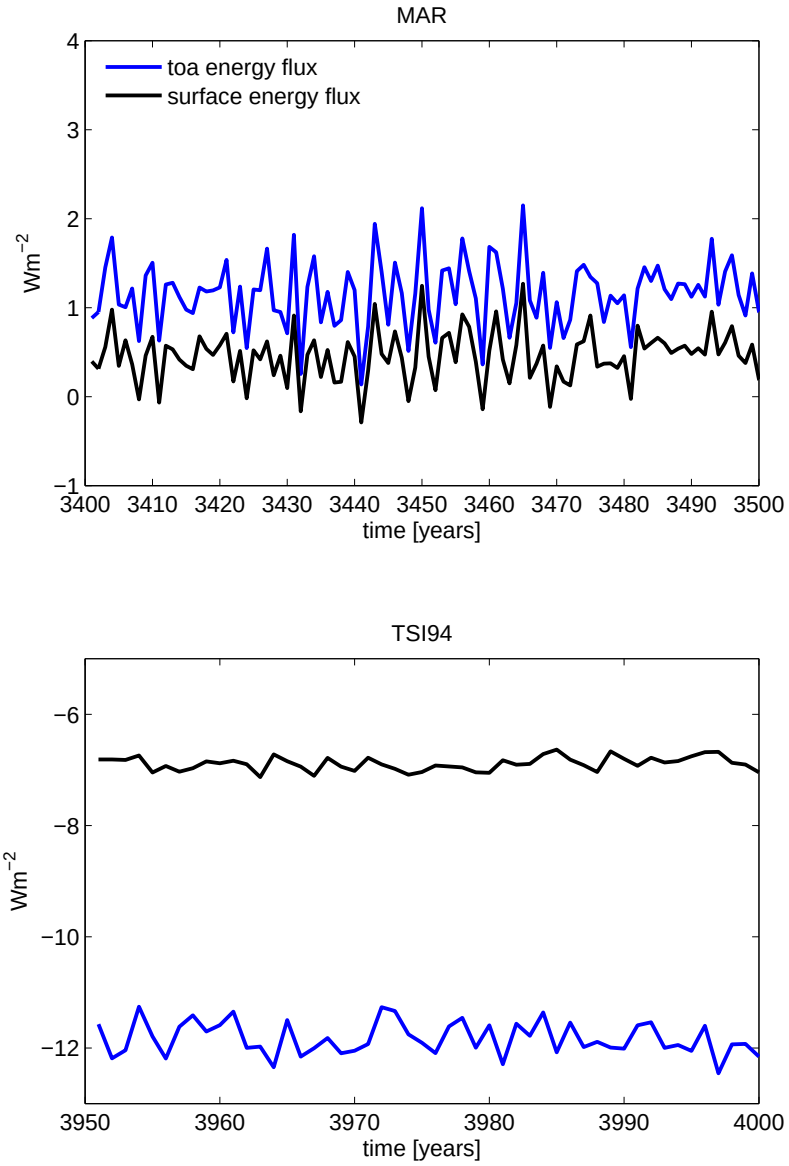

Figure 3.17: Global and annual mean top of atmosphere energy flux (blue) and surface energy flux (black) for the Marinoan control climate MAR (top), and in an equilibrium Snowball Earth for TSI set to 94% of its present-day value, provided by years 3950 to 3999 of simulation TSI94 (bottom). Positive values mean that the flux is downward, negative values that the flux is upward.

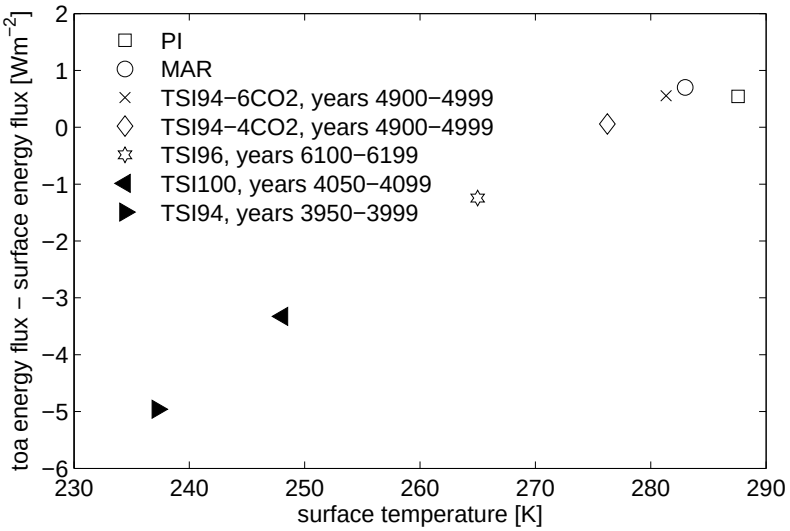

Figure 3.18: Difference between the top of atmosphere energy flux and the surface energy flux in dependence of global mean surface temperature. Positive values suggest the existence of an artificial energy sink in the atmosphere model, negative values the existence of an artificial energy source.

Moreover, the imbalance between the top of atmosphere and the surface energy fluxes exhibits a linear dependence on global mean surface temperature (Figure 3.18). Because the Snowball Earth climate differs fundamentally from the present-day climate, we suspect that the increase of imbalance with lower surface temperature is caused by ECHAM5's physics parameterizations, which are tuned to the present-day climate. We can, however, not utterly exclude that the imbalance is an artefact of the way the energy fluxes are diagnosed in ECHAM5.

A similar imbalance was found for the equilibrium Snowball Earth atmosphere under present-day surface boundary conditions with ECHAM5/MPI-OM, but it was not mentioned in Voigt and Marotzke (2009). Moreover, Romanova et al. (2006) reported that the present-day control climate of the atmosphere general circulation model of intermediate complexity PUMA shows an imbalance of 3.5 Wm^{-2}, but Romanova et al. (2006) did not analyse the reasons for this.

3.7 Discussion

In the state-of-the-art atmosphere-ocean general circulation model ECHAM5/MPI-OM, changing the surface boundary conditions from present-day to Marinoan ($\sim$ 635 Ma) induces a global mean cooling of 4.6 K for present-day total solar irradiance and pre-

industrial greenhouse gas concentrations. Although the Marinoan surface boundary conditions are distinct from the present-day surface boundary conditions in more aspects than the location of continents, we consider the latter as the primary difference between the two setups. The movement of continents from high to low latitudes according to the Marinoan reconstruction results in a redistribution of background surface albedo across the globe, with higher low latitude surface albedo in the Marinoan than today. By virtue of the larger incoming shortwave radiation in low latitudes, this implies a cooling of the climate.

This cooling entails that a Snowball Earth is much easier generated for Marinoan than for present-day surface boundary conditions. For the latter a reduction of TSI to 94% did not result in a Snowball Earth (Voigt and Marotzke 2009), whereas we find it to be sufficient for the Marinoan setup. Our simulations hence support the notion that low-latitude continents facilitate global glaciation (Kirschvink 1992). This confirms the result of Lewis et al. (2003), but is in disagreement with the opposite conclusion of Poulsen et al. (2002). In the latter study with the Fast Ocean Atmosphere Model (FOAM), changing continents from a Southern Hemisphere preponderance to equatorial supercontinent(s) effected a global warming of about 5 K.

A zero-dimensional energy balance model successfully predicts the Snowball Earth bifurcation point in terms of total solar irradiance by only knowing the equilibrium global mean ocean potential temperature for present-day total solar irradiance and pre-industrial greenhouse gases. The model has shown this ability before for present-day conditions and here confirms it in an intriguing manner. It would be interesting to see if the model in simulations with different continental setups or climate models performs equally well. However, the energy balance model in its current form does not predict the Snowball Earth bifurcation point in terms of carbon dioxide.

Sea-ice advance during the transition to a Marinoan Snowball Earth is symmetric about the equator, in contrast to the transition to a modern Snowball Earth with present-day geography (Voigt and Marotzke 2009). This confirms that continents via their albedo effect play an important role for heat transports and sea-ice advance during the transition, and underscores that the asymmetric distribution of present-day continents betwen the two hemispheres is the main reason for asymmetric heat transports and sea-ice advance during the transition to a modern Snowball Earth (Voigt and Marotzke 2009).

ECHAM5/MPI-OM does not exhibit states with near complete sea-ice cover but open equatorial water as the climate system becomes unstable for sea-ice cover above 55% of the ocean area. Note that this is consistent with FOAM (Poulsen and Jacob 2004). A possible explanation why Chandler and Sohl (2000) and Micheels and Montenari (2008) found such solutions is that their models neglected ocean dynamics. For the maximum stable sea-ice extent most parts of the continents are still too warm do allow perennial snow cover (Fig. 3.15). Even if snow cover is possible, it mainly stays at

depth below 0.1 m water equivalent. We therefore do not find indications for Slushball Earth solutions although our simulations do not allow us to exclude their existence categorically. Moreover, we find that the dominant portion of sea ice is covered by snow. This suggests that the albedo of snow-covered sea ice is more important for Snowball Earth initiation than the bare sea-ice albedo.

Despite the importance of ocean dynamics, the only coupled atmosphere-ocean general circulation model subjected to Snowball Earth initiation before our study is FOAM. To simulate globally sea-ice covered oceans in FOAM, TSI had to be decreased to 91% for carbon dioxide at 140 ppm (Poulsen and Jacob 2004). This shows that Snowball Earth initiation in FOAM clearly requires a much stronger forcing than in ECHAM5/MPI-OM, and implies that the notion that including ocean dynamics requires "extreme" radiative forcings for Snowball Earth initiation (Poulsen 2003) needs to be rethought. We also refute the statement that atmosphere-ocean general circulation models do not exhibit a runaway ice-albedo feedback in the Neoproterozoic (Poulsen 2003) since we here explicitly demonstrate that a runaway ice-albedo feedback occurs for Marinoan, and hence for Neoproterozoic boundary conditions in general, in a state-of-the-art atmosphere-ocean general circulation model.

There are no serious doubts that total solar irradiance in the Marinoan was around 94% of its present-day value (Pierrehumbert 2010; Gough 1981). In contrast, Marinoan atmospheric carbon dioxide values appear to be highly uncertain (Peltier 2003). Moreover, the comparison of the Snowball Earth bifurcation point between models is rendered difficult by the use of different geographies and albedo values. Despite these issues, our study demonstrates that Snowball Earth initiation for Marinoan total solar irradiance (94% of the present-day value) in the arguably best climate model hitherto applied is possible at similar or even higher carbon dioxide levels than in simpler models (Donnadieu et al. 2004b; Micheels and Montenari 2008; Chandler and Sohl 2000). We therefore conclude that from the perspective of Snowball Earth initiation, there is no conflict between climate modelling and the Snowball Earth hypothesis. This rebuts previous statements that relied on models neglecting ocean dynamics but also on the FOAM model, which includes a dynamic ocean (see Sec. 3.1).

3.8 Conclusion

Using the state-of-the-art atmosphere-ocean general circulation model ECHAM5/MPI-OM to study the initiation of a Marinoan Snowball Earth and comparing these simulations with a previous study with present-day surface boundary conditions (Voigt and Marotzke 2009), we conclude the following:

1. Changing surface boundary conditions from present-day to Marinonan induces a global mean cooling of 4.6 K. Our study supports the notion that low-latitude

continents facilitate Snowball Earth initiation, in contrast to a previous study with the atmosphere-ocean general circulation model FOAM.

2. For pre-industrial atmospheric carbon dioxide, the Snowball Earth bifurcation points is between 95.5 and 96% of the present-day value of total solar irradiance. For total solar irradiance set to its Marinoan value, i.e., 94% of the present-day total solar irradiance, a Snowball Earth is prevented by quadrupling atmospheric carbon with respect to its pre-industrial concentration. We rebut previous conclusions that Snowball Earth initiation would require "extreme" forcings.

3. The Marinoan Snowball Earth bifurcation point in terms of total solar irradiance can be predicted by a zero-dimensional energy balance given the equilibrium mean ocean potential temperature for the present-day total solar irradiance.

4. Sea-ice cover of more than 55% of the ocean surface area is unstable, akin to what was found for present-day surface boundary conditions. ECHAM5/MPI-OM therefore does not exhibit states with near-complete sea-ice cover but open equatorial waters. This is in contrast to modelling studies that neglected ocean dynamics.

3.A Sensitivity to vertical mixing parameters of the ocean model

In this study, we inadvertently apply smaller Pacanowski-Philander (PP) vertical viscosity and diffusivity parameters than for the transition to a modern Snowball Earth (Voigt and Marotzke 2009) and the pre-industrial control run PI (cf. Sect. 3.2). This study uses $0.2 \cdot 10^{-2}\,\mathrm{m^2 s^{-1}}$ instead of the five times larger value $1.0 \cdot 10^{-2}\,\mathrm{m^2 s^{-1}}$ of Voigt and Marotzke (2009) and PI. We stress that both choices are in the range of "accepted" values and that here is no physical reason to prefer one over the other. Also, the PP vertical viscosity and diffusivity parameters must be distinguished from the vertical viscosity and diffusivity that is actually applied in the model; for details on how the PP vertical viscosity and diffusivity parameters enter, among others, the calculation of vertical viscosity and diffusivity we refer to Marsland et al. (2003).

One might nevertheless suspect that this parameter change might vitiate our comparison of the Marinoan and pre-industrial control climates, MAR and PI, or our result for the Snowball Earth bifurcation point and maximum stable sea-ice cover. That none of this is the case is demonstrated by the following simulations (see Table 3.5).

For the Marinoan control climate, quintupling PP vertical viscosity and diffusivity parameters (simulation MAR-PP5) does not affect sea-ice area and surface temperature; both quantities agree in MAR and MAR-PP5 within their interannual variabilities. Mean ocean potential temperature is increased by less than 0.04 K in MAR-PP5.

Table 3.5: ECHAM5/MPI-OM simulations performed with Pacanowski-Philander (PP) vertical viscosity and diffusivity parameters multiplied by five. The applied total solar irradiance is given in percentage of the present-day value 1367 Wm^{-2}. All simulations use pre-industrial carbon dioxide.

simulation	TSI	sim. years	remark
MAR-5PP	100%	3300-3799	started from year 3299 of SPINUP
TSI96-5PP	96%	5600-6199	started from year 5599 of TSI96, ocean time step of 3600 s
TSI955-5PP	95.5%	6200-6599	started from year 6199 of TSI96-5PP, ocean time step of 3600 s

Time and zonal mean surface temperature, full and clear-sky radiative fluxes at the top of atmosphere and surface, and turbulent surface fluxes are virtually unaltered in MAR-PP5 compared to MAR. We therefore conclude that the difference in PP vertical viscosity and diffusivity parameters between MAR and PI is of no consequence for our comparison of the Marinoan and pre-industrial control climate, in particular including the analysis with the one-dimensional energy balance model.

For the Snowball Earth bifurcation point and maximum stable sea-ice cover, quintupling PP vertical viscosity and diffusivity parameters for TSI decreased to 96% (TSI96-PP5) causes a decrease in annual mean sea-ice area by 2% of the ocean surface area, as well as an increase of annual and global mean surface temperature by 1 K and an increase of annual and global mean ocean potential temperature by 0.05 K after 600 years compared to TSI96. Altough this demonstrates some sensitivity to the vertical mixing parameterization, our conclusion that a TSI reduction to 96% of its present-day value does not trigger a Snowball Earth remains valid. A further reduction of TSI by 0.5% of its present-day value at year 6200 of TSI96-PP5 leads to global sea-ice cover within 360 years, akin to our results for smaller PP viscosity and diffusivity parameters. Our result that the Snowball Earth bifurcation point is located between 95.5 and 96% of the present-day total solar irradiance is therefore robust with respect to quintupling PP viscosity and diffusivity parameters. Moreover, also for quintupled PP vertical viscosity and diffusivity parameters, sea-ice cover above 55% is unstable.

Chapter 4

Equinox Hadley cell dynamics in a Snowball Earth atmosphere

We use the state-of-the-art atmospheric general circulation model ECHAM5 to investigate a cold and virtually dry Snowball Earth atmosphere that results from specifying sea ice as the surface boundary condition everywhere, corresponding to a frozen aquaplanet, while keeping total solar irradiance at its present-day value. The aim of this study is the investigation of the meridional circulation of a Snowball Earth atmosphere, which, due to missing moisture, might constitute an ideal though yet unexplored testbed for theories of atmospheric dynamics. The meridional circulation consists of a thermally direct cell extending from the equator to 45° N/S with ascent close to the equator, and a weak thermally indirect cell with descent between 45 and 65° N/S and ascent near the poles. The thermally direct cell is subdivided into a weak deep cell reaching well into the stratosphere and a strong Hadley cell that is confined to the troposphere. The dynamics of the Snowball Earth Hadley cell differ substantially from the dynamics of the present-day Hadley cell. In the upper branch of the Snowball Earth Hadley cell, mean meridional advection of mean absolute vorticity is not only balanced by eddy momentum fluxes but also by vertical diffusion. Vertical diffusion also contributes to the meridional momentum balance as it decelerates the Hadley cell by downgradient momentum mixing between its upper and lower branches. Suppressing vertical momentum diffusion above 870 hPa results in an increase of the Hadley cell strength by a factor of about 2, depending on the treatment of turbulent kinetic energy. Simulations where we only suppress either vertical diffusion of zonal or meridional momentum show that this increase can be understood from the decelerating effect of vertical diffusion in the meridional momentum balance. Comparing our simulations with theories, we conclude that neither axisymmetric Hadley cell models based on angular momentum conservation nor eddy-permitting Hadley cell models that neglect vertical diffusion of momentum are applicable to a Snowball Earth atmosphere under equinox insolation since both assume an inviscid upper Hadley cell branch. Moreover, our results suggest that dry atmospheres should not be considered as a-priori simpler testcases for Hadley cell theories than moist atmospheres.

4.1 Introduction

Developing a closed theory for the meridional circulation of the atmosphere remains one of the main challenges in atmospheric dynamics. From the very beginning, a particular focus has been laid on the Hadley cell, a synonym for the tropical overturning circulation. In this study, we confront existing Hadley cell theories with a Snowball Earth atmosphere simulated by a state-of-the-art atmosphere general circulation model, and investigate if the assumptions made to derive these theories and hence the theories themselves hold in this cold and virtually dry climate. To ease comparison with theories, insolation follows equinox conditions with disabled diurnal cycle.

The challenge of atmospheric dynamics, in contrast to most natural science disciplines, is not in ascertaining the underlying dynamical equations. These are essentially known. The art is in fact to distill, for a given problem, the primal terms of this coupled set of non-linear and multi-scale partial differential equations, and to neglect the others. One of the most prominent examples for this approach of theory building is the Hadley circulation (see Lorenz (1967) for a historic review, and Schneider (2006) for a summary of recent progress).

One important branch of Hadley cell theories, pioneered by Schneider (1977) and Held and Hou (1980) and recently extended by Caballero et al. (2008), has emerged from the postulate that the upper Hadley cell branch conserves angular momentum. This assumption, combined with thermal wind balance and the requirement that no energy is exported from the Hadley cell region, allows one to derive a closed Hadley cell theory that predicts Hadley cell strength and width in dependence of only external parameters like rotation rate and radiative-equilibrium pole-to-equator temperature contrast (e.g., Held 2000).

One criticism of these models is that they produce too strong subtropical jets. The latter is, at least partly, a consequence of neglecting non-axisymmetric motions, i.e. eddies, and their momentum transport. As eddy effects were found to be non-negligible in the upper Hadley cell branch of today's atmosphere on Earth (Walker and Schneider 2006), one needs to account for them. Including their influence by dropping the axisymmetric assumption leads to the second important branch of Hadley cell theories as described in Schneider (2006). These theories do not posses the neat feature of being analytically solvable since eddy momentum fluxes are a-priori unknown and depend on the mean circulation, but simulations with idealized general circulation models allow to derive scaling laws for the Hadley cell strength and width (Walker and Schneider 2006; Korty and Schneider 2008).

Despite large progress made in understanding Hadley cell dynamics (see Schneider (2006) for a review), an investigation of the Hadley cell of a Snowball Earth atmosphere is missing. The latter might constitute an ideal testbed for atmospheric dynamics because the near absence of water eliminates the hitherto unsolved problems of incorpo-

rating the effect of latent heat and moist convection into a moist Hadley cell theory. By offering a distinct realization of a dry atmosphere, the Snowball Earth therefore should allow us to test the much further developed dry Hadley cell theories.

Taking a first step towards closing this gap, we apply the state-of-the-art atmosphere general circulation model ECHAM5 (Roeckner et al. 2003). ECHAM5's comprehensive suite of physical parameterizations, including a full radiation code and dry convection scheme, represents a major difference between our work and previous studies (Walker and Schneider 2006; Korty and Schneider 2008) with an idealized general circulation model. The latter model resolves the three-dimensional large-scale flow but only crudely accounts for subgrid-scale processes. In particular, turbulent momentum mixing, modelled by vertical diffusion, is restricted to the lowest part of the atmosphere (see Schneider and Walker (2006) for details of this model).

This study investigates the dynamics of a Snowball Earth Hadley cell by analyzing the zonal and meridional momentum balances. We do not focus on how the atmospheric circulation might ease or hinder the deglaciation of a Snowball Earth. However, we will be able to assess the importance of Hadley cell strength on equatorial surface temperature.

The paper is organized as follows. Section 2 describes the atmosphere general circulation model ECHAM5 and setup of the simulations. Section 3 summarizes main features of the meridional circulation of a Snowball Earth atmosphere before a detailed analysis of the zonal and meridional momentum balance is given in Sect. 4. Section 5 discusses the effect of vertical diffusion on the Hadley cell strength and presents corresponding simulations. In Section 6, we investigate the sensitivity of our results to the diurnal cycle in insolation and to the model's formulation of vertical diffusion. Section 7 gives a general discussion of the results, section 8 follows with conclusions.

4.2 Model and simulation setup

We use the Max Planck Institute for Meteorology atmosphere general circulation model ECHAM5.4.01 (labelled ECHAM5 in the following). ECHAM5 (Roeckner et al. 2003) is the fifth generation of the ECHAM model series that originally evolved from the weather prediction model of the European Centre for Medium Range Weather Forecasts. The dynamical core of ECHAM5 employs the spectral transform method with triangular truncation to numerically solve the hydrostatic primitive equations of the atmosphere. The prognostic variables are vorticity, divergence, temperature, and logarithm of surface pressure. A semi-implicit leapfrog scheme is used for time integration, with the growth of spurious computational modes inhibited by an Asselin filter. ECHAM5 contains state-of-the-art physics parameterizations that are solved in grid-point space on a Gaussian grid. The radiation scheme comprises 6 spectral bands for shortwave radiation and 16 bands for longwave radiation, the latter is calculated by the

Rapid Radiative Transfer Model (Mlawer et al. 1997). ECHAM5 contains a full turbulence, or dry convection, scheme. Turbulent surface fluxes of momentum and heat are calculated from a bulk aerodynamic formula. Transfer coefficients are obtained from Monin-Obukhov similarity theory and depend on stability through the bulk Richardson number. Above the surface layer, vertical turbulent fluxes follow the eddy diffusion method. Eddy viscosity and diffusivity depend on mixing length, Richardson number and turbulent kinetic energy (TKE). The dependence on Richardson number is implemented via stability functions similar to Louis (1979). TKE is calculated by a simplified prognostic TKE equation that neglects advection of TKE by the resolved flow and uses eddy viscosity for all turbulent fluxes (Roeckner et al. 2003; Brinkop and Roeckner 1995). The top of the boundary layer is diagnosed as the maximum of two heights; one based on the friction velocity, the other defined as the highest level with smaller dry static energy than the surface level.

ECHAM5 also contains parameterizations for stratiform clouds and cumulus convection (Tiedtke 1989; Nordeng 1994). These are only of little importance for the cold and virtually dry Snowball Earth atmosphere investigated in this study. Similarly, the scheme for gravity wave drag due to subgrid scale orography does not act here because of the flat sea-ice surface (see below).

ECHAM5 has been successfully evaluated against observations (Roeckner et al. 2006; Wild and Roeckner 2006) and, coupled to the Max Planck Institute for Meteorology ocean general circulation model MPI-OM (Marsland et al. 2003), was used for the integrations for the fourth assessment report of the Intergovernmental Panel on Climate Change (e.g., Brasseur and Roeckner 2005; Bengtsson et al. 2006; Landerer et al. 2007).

In this study, we use ECHAM5 with idealized Snowball Earth boundary conditions. The surface is specified as sea ice everywhere, corresponding to a frozen aqua planet (Neale and Hoskins 2000a,b). Sea-ice thickness is nominally set to 10^{10} m to effectively eliminate the conductive heat flux through sea ice from the surface energy balance. Sea-ice surface temperature is calculated by the balance of surface radiative and turbulent fluxes and assuming a specific heat capacity that corresponds to a sea-ice thickness of 0.1 m. This implies a small thermal inertia of the surface. According to the sea-ice surface, roughness length is set to 10^{-3} m. Total solar irradiance is set to its present-day value of 1365 Wm^{-2}. The only atmospheric greenhouse gas apart from prognostic water vapor is CO_2 at a concentration of 300 ppm. The atmospheric concentration of all other radiatively active trace gases (CH_4,N_2O,CFCs) is set to zero, and ozone as well as aerosols are not accounted for in the radiation code. Solar insolation follows permanent equinox conditions resulting from a circular orbit with zero obliquity and disabled diurnal cycle (see Fig. 4.1).

We employ the medium-resolution version of ECHAM5 with spectral truncation T63 in the horizontal and 31 unevenly spaced hybrid σ-levels. In a comparison to ERA-40 data, this resolution was found to be only slightly inferior to higher resolution versions

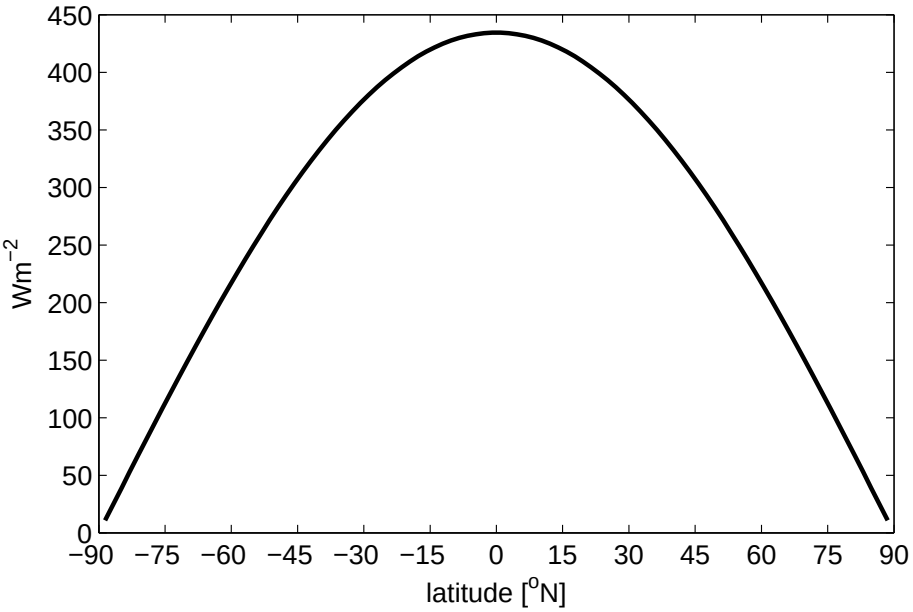

Figure 4.1: Incoming shortwave radiation at the top of atmosphere as applied in this study. The orbit is circular with zero obliquity, the diurnal cycle is disabled.

while requiring much less computational time (Roeckner et al. 2006). Nevertheless, to check the robustness of our results with respect to vertical resolution, we also conduct one simulation with 62 instead of 31 levels.

Two changes to the ECHAM5 model were necessary to adapt the model to our Snowball Earth simulations. For uncoupled simulations, ECHAM5 limits sea-ice cover to 99% and sea-ice thickness is fixed to 2 m in the Northern and 1 m in the Southern Hemisphere. We removed these restrictions such that in our simulations, sea-ice cover attains 100% and sea-ice thickness is set to 10^{10} m on the entire globe (see above).

After initialization, we integrate the model for 20 years. Statistics are taken from the last 5 years. As Northern and Southern Hemisphere are statistically identical in our simulations, we only present averages over the Northern and the Southern Hemispheres. Table 4.1 summarizes the simulations performed in this study.

4.3 Meridional structure of the Snowball Earth atmosphere

We begin with an analysis of the time and zonal mean structure of potential temperature, mass stream function, and zonal wind that result from the idealized Snowball Earth boundary conditions (simulation STD).

The Snowball Earth surface temperature is 220 K at the equator and 133 K at 85° N/S

Table 4.1: Summary of ECHAM5 simulations. Labels indicate whether vertical diffusion of zonal momentum (U), meridional momentum (V) and turbulent kinetic energy (T) follows the standard setup of ECHAM5 (on=1) or is suppressed above 870 hPa (off=0). TKE abbreviates turbulent kinetic energy. Hadley cell strength is measured by the absolute maximum of the mass stream function and given in units of 10^9 kgs^{-1}. $T_{\mathrm{sfc}}^{\mathrm{eq}}$ denotes the time and zonal mean surface temperature averaged over the two latitudes that are closest to the equator.

simulation	vertical diffusion of			Hadley cell strength	$T_{\mathrm{sfc}}^{\mathrm{eq}}$
	zonal mom.	meridional mom.	TKE		
STD	on	on	on	76	220.3 K
U0V1T1	off	on	on	70	221.1 K
U0V1T0	off	on	off	60	220.4 K
U1V0T1	on	off	on	214	220.8 K
U1V0T0	on	off	off	164	221.2 K
U0V0T1	off	off	on	172	220.5 K
U0V0T0	off	off	off	121	220.5 K

resulting in a strong equator-to-pole surface temperature contrast of 87 K (Fig. 4.2). This is more than twice as large as the annual mean equator-to-pole surface temperature contrast for the present-day Northern Hemisphere (Peixoto and Oort 1992). Equatorward of 15° N/S, potential temperature decreases with height in the immediate vicinity to the surface, a manifestation of persistent static instability resulting from high insolation, and is uniform in the lower atmosphere. Strong vertical gradients above 550 hPa imply a stable stratification in the upper equatorial atmosphere. Isentropes around 550 hPa show a trough around 25° N/S, a feature similar to today's lower stratosphere (Holton 2004). Meridional potential temperature gradients in the lower atmosphere increase rapidly towards the poles and are accompanied by steep vertical gradients poleward of 45° N/S, indicating a temperature inversion and corresponding high static stability poleward of 45° N/S in the lowest part of the atmosphere.

The thermal tropopause, here defined as the lowest level at which the lapse rate falls below 4 Kkm^{-1}, is located at around 550 hPa in the tropics (Fig. 4.2). After a slow decrease from 20° N/S to 40° N/S, the tropopause drops rapidly to the surface at 45° N/S, a consequence of the temperature inversion there. We note that this tropopause definition works well equatorwards of 10° N/S and polewards 45° N/S, where it only weakly depends on the particular lapse rate criterion, but is sensitive to the lapse rate criterion between 10° N/S and 45° N/S; between 15 and 35° N/S the lapse rate does not even

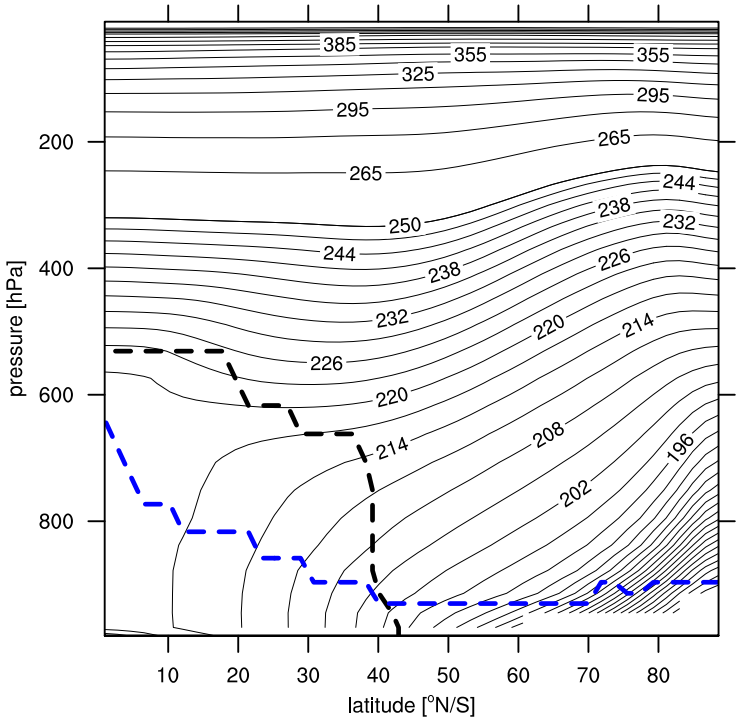

Figure 4.2: Time and zonal mean potential temperature in K for simulation STD. Contour interval is 3 K below 250 K and 15 K above. The black dashed line depicts the thermal tropopause as defined by a 4 Kkm^{-1} lapse rate criterion. The blue line depicts the time and zonal mean top of the planetary boundary layer.

drop to 2 Kkm^{-1} below 50 hPa. The planetary boundary layer in the time and zonal mean stretches up to 650 hPa ($\sim$2700 m) at the equator. This is only 100 hPa lower than the tropopause. Between 5° N/S and 40° N/S, the mean planetary boundary layer ends about 200 hPa below the tropopause, again much less than in the present-day atmosphere. Poleward of 45° N/S the top of the boundary layer is not set by the vertical profile of dry static energy but the friction velocity, resulting in an extension of the planetary boundary layer beyond the tropopause.

The meridional circulation, measured by the mass stream function, consists of a thermally direct clockwise cell extending from the equator to 45° N/S, and a weak thermally indirect counterclockwise cell with descent between 45 and 65° N/S and ascent in the polar region (Figure 4.3). The direct cell is subdivided into a weak deep stratospheric cell and a much stronger tropospheric cell. In the remainder of this paper we will refer to this tropospheric cell as Hadley cell. In contrast to today's atmosphere, the polar cell is missing in the Snowball Earth atmosphere. Just below the tropopause at the upper poleward edge of the Hadley cell, a faint counterclockwise cell appears.

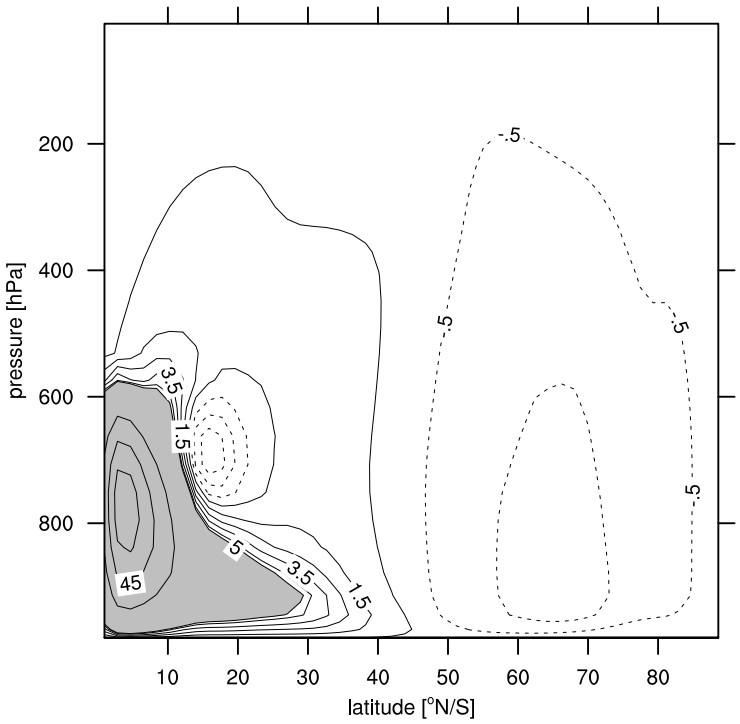

Figure 4.3: Mass stream function in $10^9\,\mathrm{kgs}^{-1}$ for simulation STD. Solid lines mean clockwise circulation, dashed lines counterclockwise circulation. Contour interval is $20 \cdot 10^9\,\mathrm{kgs}^{-1}$ above $5 \cdot 10^9\,\mathrm{kgs}^{-1}$ (grey filling), and $1 \cdot 10^9\,\mathrm{kgs}^{-1}$ below $5 \cdot 10^9\,\mathrm{kgs}^{-1}$.

The surface zonal wind has, going from the equator to the pole, an easterly-westerly-easterly-westerly pattern, with the maximum surface wind being westerly of almost $2\,\mathrm{ms}^{-1}$ at 70° N/S (Figure 4.4). This pattern is different from today's pattern of easterlies-westerlies-easterlies (Vallis 2006). The zonal wind is easterly at the equator at all altitudes, except close to the model's upper boundary. At 16° N/S and 650 hPa, below the tropopause and right at the location of the aforementioned weak counterclockwise cell, a jet of $5\,\mathrm{ms}^{-1}$ forms. Poleward of 45° N/S, strong vertical shears of zonal wind, accompanied by corresponding meridional potential temperature gradients, indicate high baroclinicity and hence eddy activity, and a second and much stronger jet appears at 65° N/S and 50 hPa. In the upper Hadley cell branch, the local Rossby number $-\overline{\zeta}/f$ ($\overline{\zeta}$ denotes mean relative vorticity, f the Coriolis parameter) does not exceed 0.5 at the latitude of the Hadley cell maximum at 4.6° N/S and is below 0.4 poleward thereof (Fig. 4.4), indicating that mean angular momentum is not horizontally uniform there (see Schneider (2006)). This is partly because streamlines are not purely horizontal, but also because eddies and vertical diffusion act as mean angular momentum sinks in the upper Hadley cell branch as is analyzed in the following section.

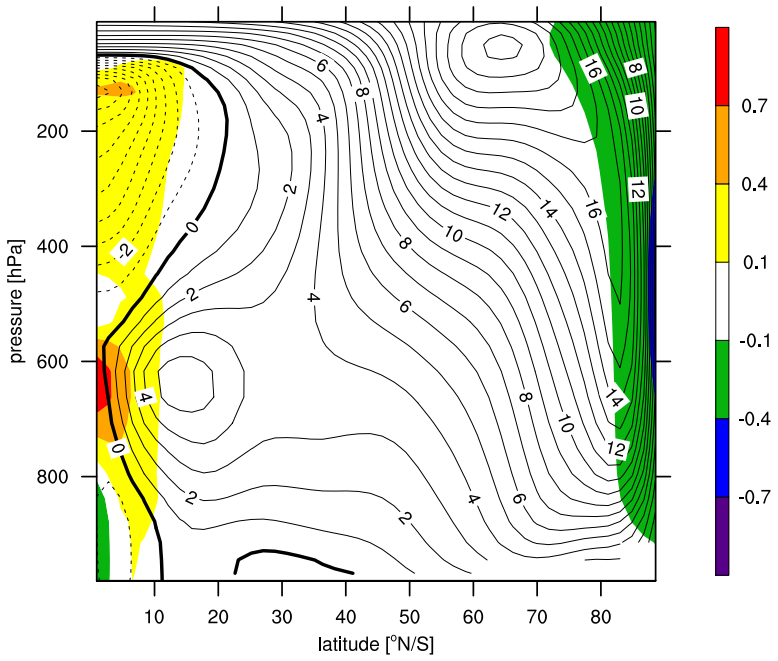

Figure 4.4: Time and zonal mean zonal wind in $\mathrm{m\,s^{-1}}$ for simulation STD. Contour interval is $1\,\mathrm{m\,s^{-1}}$, with zero contour bold. Overlaid colors show the local Rossby number.

4.4 Dynamics of the Snowball Earth Hadley cell

We proceed to the analysis of the time and zonal mean zonal and meridional momentum balances. This will allow us to gain insight into the dynamics of the Hadley cell and the dependence of the Hadley cell strength on vertical diffusion.

4.4.1 Zonal momentum balance

In spherical pressure coordinates and after taking the time and zonal mean, the steady-state primitive zonal momentum equation reads

$$0 = (f + \overline{\zeta})\overline{v} - \overline{\omega}\frac{\partial \overline{u}}{\partial p} - \frac{1}{a\cos^2\varphi}\frac{\partial(\overline{u'v'}\cos^2\varphi)}{\partial\varphi} - \frac{\partial\overline{u'w'}}{\partial p} + \overline{F}^u. \tag{4.1}$$

Here, (u, v, ω) label the zonal, meridional and pressure velocities; ζ is the relative vorticity, a is Earth's radius, φ is latitude, and p is pressure. Overbars denote a time and zonal mean, and primes deviations thereof. $\overline{F}^u = \overline{F}^u_{\mathrm{vdiff}} + \overline{F}^u_{\mathrm{cfr}} + \overline{F}^u_{\mathrm{hdiff}}$ summarizes mean zonal momentum stresses by parametrized processes, in this order, vertical diffusion of zonal momentum including surface drag, cumulus friction, and horizontal diffusion. For our analysis, we calculate mean and eddy terms based on (u, v, ω, ζ) interpolated to

31 pressure levels that are close to the models 31 hybrid sigma-levels. Tendencies due to the parameterized processes are diagnosed during the model run for each grid point (λ, φ), hybrid sigma-level, and time step, interpolated to pressure levels using the same interpolation algorithm as for wind field and relative vorticity, and finally averaged over time and longitude.

Everywhere below 900 hPa, we find a primary balance between mean meridional advection of mean absolute vorticity, $(f + \overline{\zeta})\overline{v}$, which away from the equator reduces to the mean Coriolis force (cf. the low local Rossby number in Fig. 4.4), and vertical diffusion of zonal momentum, $\overline{F}^u_{\text{vdiff}}$ (Fig. 4.5). Above 900 hPa and poleward of 45° N/S, the mean Coriolis force is balanced by meridional eddy momentum fluxes, consistent with quasi-geostrophic scaling (Holton 2004) and the picture of the Ferrel cell in today's atmosphere (Vallis 2006). In contrast, the tropical circulation in a Snowball Earth atmosphere differs substantially from that in today's atmosphere. For today's atmosphere, the poleward branch of the Hadley cell shows a balance between mean meridional advection of mean absolute vorticity and eddy momentum flux divergence S (Walker and Schneider 2006),

$$(f + \overline{\zeta})\overline{v} = f(1 - Ro)\overline{v} \approx S, \tag{4.2}$$

In our Snowball Earth atmosphere, this balance carries over for the deep weak cell above 550 hPa (not visible in Fig. 4.5 because of the chosen contour spacing), but does not hold in the upper branch of the Hadley cell. From the equator to 12° N/S in the upper branch of the Snowball Earth Hadley cell, mean meridional advection of mean absolute vorticity is balanced by eddy momentum fluxes as well as vertical diffusion of zonal momentum,

$$(f + \overline{\zeta})\overline{v} = f(1 - Ro)\overline{v} \approx S + \overline{F}^u_{\text{vdiff}}, \tag{4.3}$$

with eddies being more important in the higher part of the upper branch and vertical diffusion being more important in the lower part. Around 20° N/S, eddies are not important in the poleward branch and local Rossby numbers are close to zero, implying that the upper Snowball Earth Hadley cell branch is close to Ekman balance at these latitudes,

$$f\overline{v} \approx \overline{F}^u_{\text{vdiff}}. \tag{4.4}$$

4.4.2 Meridional momentum budget

The steady-state primitive meridional momentum equation in spherical pressure coordinates and averaged over time and longitude reads

$$0 = -f\overline{u} - \overline{v}\overline{d} - (\overline{u}^2 + \overline{v}^2)\frac{\tan\varphi}{a} - \overline{\omega}\frac{\partial\overline{v}}{\partial p} - \frac{1}{a}\frac{\partial\overline{v'v'}}{\partial\varphi} - \frac{\partial\overline{v'w'}}{\partial p} - (\overline{u'^2} - \overline{v'^2})\frac{\tan\varphi}{a} - \frac{1}{a}\frac{\partial\overline{\Phi}}{\partial\varphi} + \overline{F}^v$$

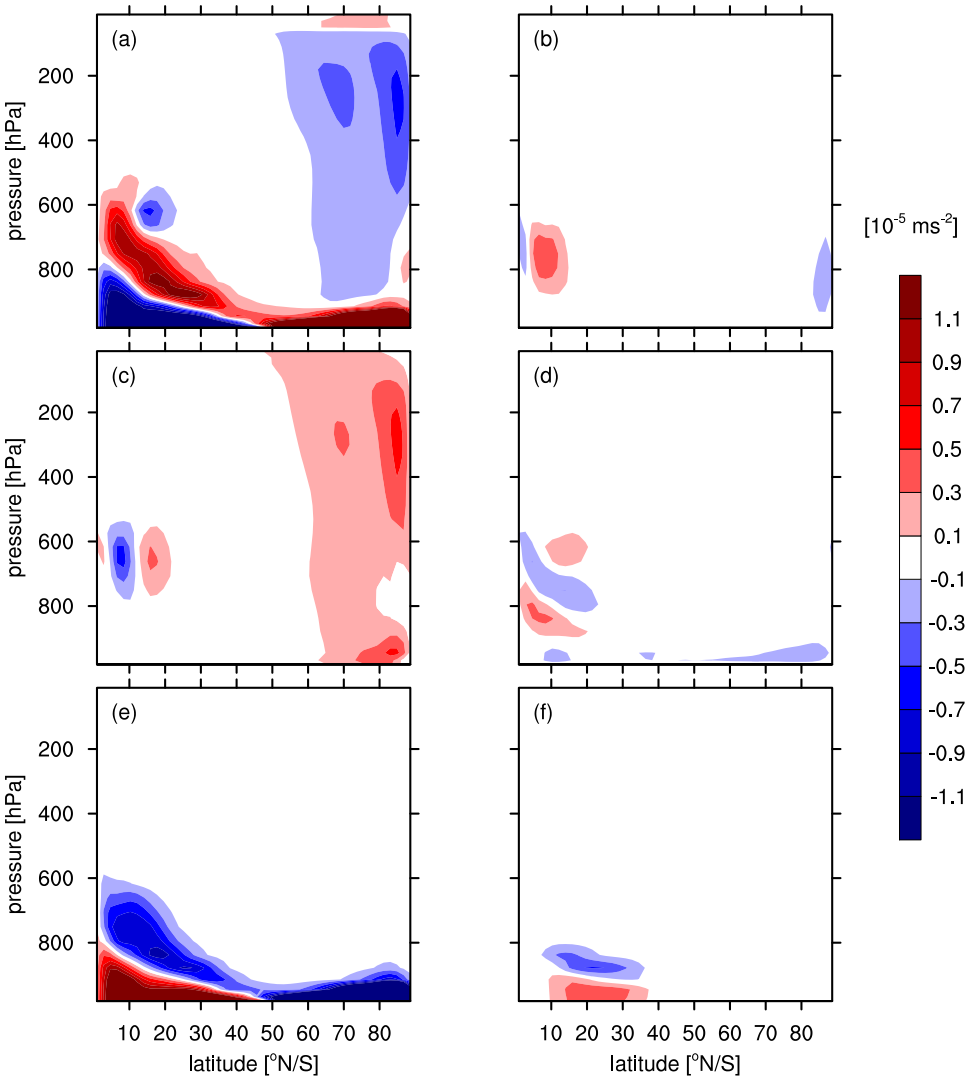

Figure 4.5: Terms of the mean zonal momentum balance in 10^{-5} ms^{-2} for simulation STD: (a) mean meridional advection of mean absolute vorticity, (b) negative of mean flow vertical advection of mean zonal momentum, (c) horizontal contribution to eddy momentum flux convergence, (d) vertical contribution to eddy momentum flux convergence, (e) vertical diffusion, and (f) cumulus friction. The magnitude of the zonal momentum tendency due to horizontal diffusion is much smaller than $0.1 \cdot 10^{-5}$ ms^{-2} except close to the models' upper boundary and hence not included in this plot.

with symbols having the same meaning as in Eq. (4.1); d denotes the divergence of horizontal wind, Φ geopotential height, $\overline{F}^v$ mean meridional momentum stresses by parameterized processes. In contrast to the mean zonal momentum balance, the geopotential gradient term survives the zonal average. As a consequence, $f\overline{u}$ and $\frac{1}{a}\frac{\partial\overline{\Phi}}{\partial\varphi}$ dominate the mean meridional momentum balance in most regions of the atmosphere, implying that zonal winds are in thermal wind balance there. In the Snowball Earth Hadley cell, however, vertical diffusion of meridional momentum is important. Vertical diffusion decelerates the meridional wind in the upper branch and accelerates the meridional wind in the lower branch (Fig. 4.6). Vertical diffusion hence reduces the vertical shear of meridional momentum by downgradient momentum mixing and causes the zonal wind to deviate from thermal wind balance in the Hadley cell. Within 6 degrees of the equator, vertical diffusion of meridional momentum is even of the same order as $f\overline{u}$ and $\frac{1}{a}\frac{\partial\overline{\Phi}}{\partial\varphi}$, and the meridional momentum budget there reads

$$0 = -f\overline{u} - \frac{1}{a}\frac{\partial\overline{\Phi}}{\partial\varphi} + \overline{F}^v_{\text{vdiff}}(p,\varphi). \tag{4.5}$$

Doubling the number of vertical levels from 31 to 62 does neither affect the influence of vertical diffusion in the zonal momentum balance nor in the meridional momentum balance (not shown). These results therefore appear to be robust to vertical resolution.

4.5 Influence of vertical momentum diffusion on Hadley cell strength

We have found that vertical diffusion of momentum is important in both the zonal and the meridional momentum balances. We now investigate how this influences the Hadley cell strength.

4.5.1 Hypothetical Hadley cell strength in an inviscid atmosphere

One gains quite some insight on the connection between vertical momentum diffusion and Hadley cell strength by the following two thought experiments. In these thought experiments we estimate how the strength of the Snowball Earth Hadley cell would change if we set vertical diffusion of one horizontal momentum component to zero while keeping it fully active for the other.

The first thought experiment makes use of the zonal momentum balance. By virtue of the latter, we decompose the mass stream function into a circulation driven by vertical diffusion of zonal momentum,

$$\tilde{\psi}(p,\varphi) = -\frac{2\pi a\cos\varphi}{fg}\int_0^p \overline{F}^u_{\text{vdiff}}(p',\varphi)dp',$$

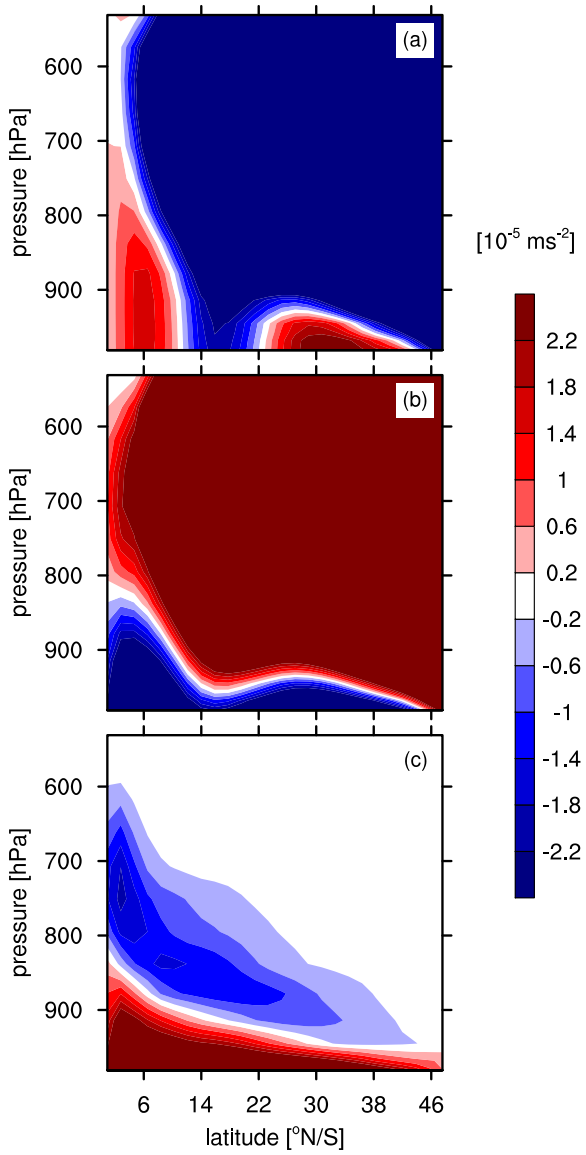

Figure 4.6: Selected terms of the meridional momentum balance in the Hadley cell region for simulation STD in $10^{-5}\,\mathrm{ms}^{-2}$: (a) Coriolis force, (b) negative of meridional gradient of geopotential height, (c) vertical diffusion of meridional momentum.

and an inviscid part ψ^* that is driven by the sum of mean and eddy momentum fluxes and all parametrised processes apart from vertical diffusion,

$$\psi^*(p,\varphi) = \psi(p,\varphi) - \tilde{\psi}(p,\varphi).$$

If we assume that removal of vertical diffusion from the zonal momentum balance would

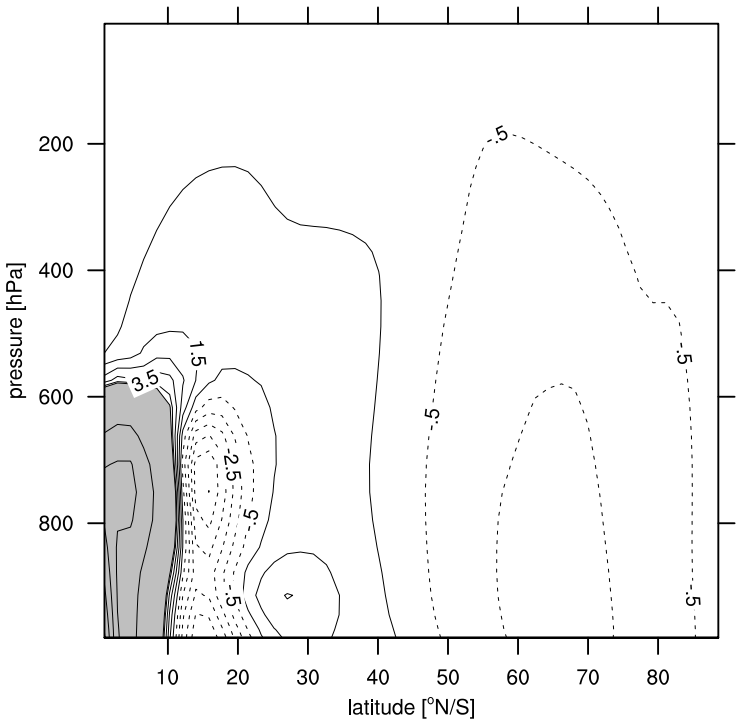

Figure 4.7: Inviscid part of the mass stream function of simulation STD in $10^9\,\mathrm{kgs}^{-1}$. Solid lines mean clockwise circulation, dashed lines counterclockwise circulation. Contour interval is $20 \cdot 10^9\,\mathrm{kgs}^{-1}$ above $5 \cdot 10^9\,\mathrm{kgs}^{-1}$ (grey filling), and $1 \cdot 10^9\,\mathrm{kgs}^{-1}$ below $5 \cdot 10^9\,\mathrm{kgs}^{-1}$.

be entirely compensated by the mean Coriolis force, and hence the mass stream function, ψ^* constitutes our first-order estimate for the mean circulation of an atmosphere that did not diffuse zonal momentum in the vertical. We find that eliminating vertical diffusion of zonal momentum should weaken the Hadley cell maximum from 76 to $47 \cdot 10^9\,\mathrm{kgs}^{-1}$ (see Fig. 4.7).

Our second thought experiment draws on the meridional momentum balance, which we, for the current purpose, approximate by the geostrophic-order terms and vertical diffusion (cf. (4.5)). We suppose that any change in the vertical diffusion of meridional momentum is completely offset by the Coriolis force, and that the geopotential gradient is not affected by the change of vertical diffusion of meridional momentum; the latter is equivalent to postulate that temperature and surface pressure remain the same. With these assumptions, we calculate the mean zonal wind that would result if vertical diffusion was eliminated in the meridional momentum balance,

$$\overline{u}^{\dagger} = -\frac{1}{af}\frac{\partial\overline{\Phi}}{\partial\varphi},$$

and from this the corresponding mean relative vorticity (Vallis 2006),

$$\overline{\zeta}^{\dagger} = -\frac{1}{a\cos\varphi}\frac{\partial}{\partial\varphi}\left(\overline{u}^{\dagger}\cos\varphi\right) = \frac{1}{a^2\cos\varphi}\frac{\partial}{\partial\varphi}\left(\frac{\cos\varphi}{f}\frac{\partial\overline{\Phi}}{\partial\varphi}\right).$$

Replacing mean relative vorticity by $\overline{\zeta}^{\dagger}$ and demanding that the mean meridional velocity will adapt such that the mean meridional advection of mean absolute vorticity remains the same,

$$(f+\overline{\zeta})\overline{v} = (f+\overline{\zeta}^{\dagger})\overline{v}^{\dagger}, \tag{4.6}$$

we arrive at our first-oder estimate for the mass stream function in an atmosphere free of vertical diffusion of meridional momentum,

$$\psi^{\dagger}(p,\varphi) = \frac{2\pi a\cos\varphi}{fg}\int_0^p \frac{f+\overline{\zeta}}{f+\overline{\zeta}^{\dagger}}\overline{v}dp'. \tag{4.7}$$

At the Hadley cell maximum, the mass stream function is predicted to increase from 76 to $114\cdot10^9$ kgs^{-1}. An increase in the Hadley cell strength when vertical diffusion of meridional momentum is suppressed is consistent with the decelerating effect of vertical diffusion on the Hadley cell.

Our thought experiments suggest that removing vertical diffusion of zonal momentum should weaken the Hadley cell by the same amount as suppressing vertical diffusion of meridional momentum should strengthen it. We now test both ideas in our state-of-the-art atmospheric general circulation model.

4.5.2 Simulations with suppressed vertical diffusion of horizontal momentum

We now report on simulations where we suppress vertical diffusion of horizontal momentum above 870 hPa. This is achieved by changing eddy viscosity in the following way. Additional to the eddy viscosity K_m computed by ECHAM5's turbulence scheme, we introduce a restricted eddy viscosity $K_m^{'}$ that equals K_m for the lowest 4 model levels (surface to $\simeq$ 945 hPa) and is set to 10^{-8}m^{2}s^{-1} above model level 26 ($\simeq$ 870 hPa). At model level 27 ($\simeq$ 910 hPa), we set $K_m^{'} = 0.5\cdot K_m$ for a somewhat smoother shape of the restricted eddy viscosity. If we apply $K_m^{'}$ instead of K_m, we effectively suppress vertical momentum diffusion above 870 hPa and hence restrict it to the lowest part of the atmosphere.

This approach allows us to test the effect of individually suppressing vertical diffusion of either zonal or meridional momentum by applying the restricted eddy viscosity $K_m^{'}$ to one of the horizontal momentum components while applying the full eddy viscosity K_m to the other component. Implementing this approach is straightforward but introduces a potentially important ambiguity in the treatment of turbulent kinetic energy (TKE).

Recall that eddy viscosity depends on the square root of TKE, and that TKE itself is calculated by a simplified prognostic TKE equation that neglects horizontal TKE advection (Roeckner et al. 2003). The numerical technique to solve the TKE equation involves vertical TKE diffusion with eddy viscosity used as diffusion coefficient (Brinkop and Roeckner 1995). Altering vertical diffusion of horizontal momentum therefore also requires to decide whether we apply the full or restricted eddy viscosity for vertical TKE diffusion. We stress that the eddy diffusivity used for the vertical diffusion of dry static energy is not changed by this procedure in any part of the atmosphere. Changes in the flow and temperature field resulting from suppressing vertical momentum diffusion may lead to changes in eddy diffusivity and viscosity compared to STD, however.

In total, we perform six simulations spanning the six combinations of choosing full or restricted eddy viscosity for zonal momentum, meridional momentum, and turbulent kinetic energy (Table 4.1).

In line with the results of our thought experiments, suppressing vertical diffusion of zonal momentum weakens the Hadley cell while suppressing vertical diffusion of meridional momentum strengthens it (Figure 4.8 and Table 4.1). The exact magnitudes differ from our first-order estimates, however. Suppressing vertical diffusion of zonal momentum only moderately reduces the Hadley cell strength to 60 to 70 $\cdot 10^9$ kgs^{-1}, depending on vertical TKE diffusion (simulations U0V1T0 and U0V1T1). In contrast, suppressing vertical diffusion of meridional momentum strongly increases the Hadley cell to 164 to 214 $\cdot 10^9$ kgs^{-1} (simulations U1V0T0 and U1V0T1). This is much higher than our estimate. The increase of Hadley cell strength resulting from suppressing vertical diffusion of both horizontal momentum components is similar to the average of the individual responses (U0V0T0 and U0V0T1). Simulations with full TKE diffusion have stronger Hadley cells than their counterparts with suppressed TKE diffusion, showing that the treatment of vertical TKE diffusion systemattically influences the Hadley cell strength. The same holds for the shape of the Hadley cell. For example, the Hadley cell extends higher up for full TKE diffusion. Moreover, the weak counterclockwise cell at 15° N/S extends closer to the surface when suppressed vertical diffusion of zonal momentum meets suppressed (U0V1T0,U0V0T0) instead of full (U0V1T1,U0V0T1) vertical TKE diffusion.

Despite the influence of the treatment of TKE on the exact Hadley cell strength, we find a robust response of the Hadley cell strength. Suppressing vertical diffusion of zonal momentum moderately weakens the Hadley cell while suppressing vertical diffusion of meridional momentum strongly strengthens the Hadley cell. The zonal momentum balance that results from suppressing vertical diffusion of zonal and meridional momentum exhibits two features that are worth noting (Fig. 4.9). First, horizontal eddies now converge zonal momentum to the equator, which is associated with weak equatorial superrotation between 530 and 750 hPa. Second, vertical eddies become much stronger and compensate, at least partly, for the loss of vertical diffusion of zonal momentum.

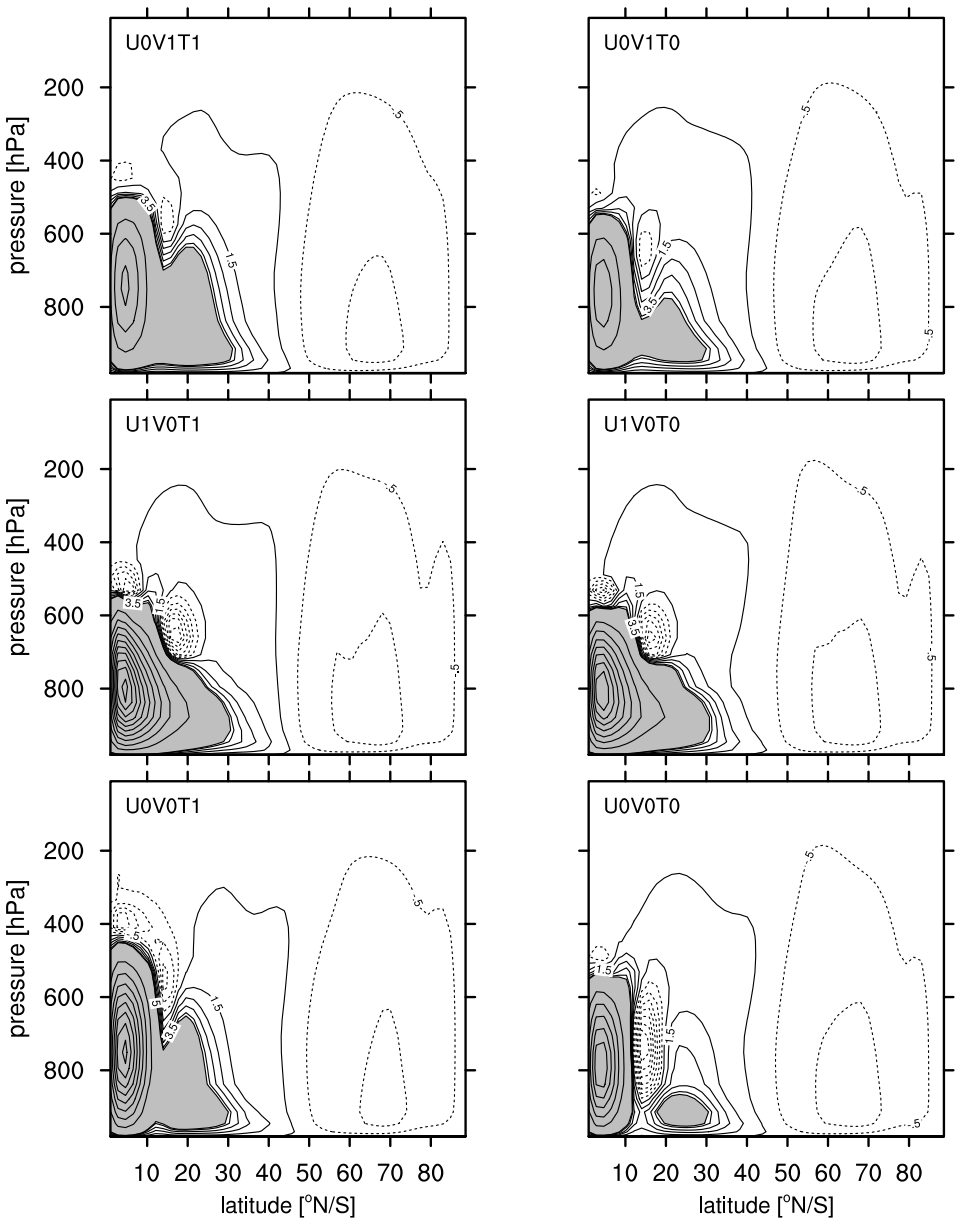

Figure 4.8: Mass stream functions of simulations with suppressed vertical momentum diffusion above 870 hPa in $10^9\,\mathrm{kgs}^{-1}$. Rows show simulations with suppressed vertical diffusion of zonal momentum (top), of meridional momentum (middle), and of zonal and meridional momentum (bottom). The left column contains simulations with full diffusion of turbulent kinetic energy, the right column simulations with suppressed vertical diffusion of turbulent kinetic energy. Solid lines mean clockwise circulation, dashed lines counterclockwise circulation. Contour interval is $20 \cdot 10^9\,\mathrm{kgs}^{-1}$ above $5 \cdot 10^9\,\mathrm{kgs}^{-1}$ (grey filling), and $1 \cdot 10^9\,\mathrm{kgs}^{-1}$ below $5 \cdot 10^9\,\mathrm{kgs}^{-1}$.

Moreover, suppressing vertical momentum diffusion leads to a vertical zigzag structure of meridional wind in the upper branch of the Hadley cell, resulting in strong meridional wind shear there. This suggests that vertical momentum diffusion would develop if it was allowed to do so.

4.6 Influence of the diurnal cycle and the parameterization of eddy viscosity

There are two issues that are of potential importance for our results. First, it is known that atmosphere general circulation models used for numerical weather prediction or climate applications tend to generate too strong vertical mixing in stable boundary layers, compared to turbulence theory and observations. The strong mixing is a consequence of choosing "long-tail" stability functions that do not drop to zero above the critical Richardson number, $Ri_c = 0.2$, as suggested by Monin-Obukhov theory, but fall to zero only slowly. This choice is motivated by improving simulation of the present-day climate (see Savijarvi 2009, and references therein). The stability function applied in ECHAM5 are of this long-tail type.

Second, climate model studies have shown that the planetary boundary layer (PBL) depth over deserts exhibits a strong diurnal cycle (Medeiros et al. 2005; Randall et al. 1985). Despite a deep PBL during the day with maximum depth near sunset, the strong shrinking of the PBL during the night effects that the mean PBL depth in simulations with diurnal cycle of insolation is smaller than in simulation using diurnally averaged insolation. Since the Snowball Earth, like desert regions, has a surface with low thermal intertia and dry air above, including the diurnal cycle might push down the mean PBL and therefore effect vertical diffusion.

Because both the choice of a long-tail stability function and the exclusion of the diurnal cycle might explain the importance of vertical momentum diffusion for the Snowball Earth Hadley cell, we additionally perform simulations with enabled diurnal cycle and using a short-tail stability function for stable and neutral conditions (Table 4.2). This stability function follows the slight modification of Zilitinkevich et al. (2002) suggested by Savijarvi (2009) and is given by

$$f_{\mathrm{SHORT}}(Ri) = (1 + 5Ri + 44Ri^2)^{-2},$$

with Ri denoting the Richardson number. This function is considerably lower than ECHAM5's standard stability function and the same for momentum and dry static energy (Figure 4.10). In all other aspects, the simulations of this section are identical to STD.

None of these simulations generates a fundamentally different shape of the Hadley cell; as in STD, the bulk of the mass stream function is concentrated within 10° N/S

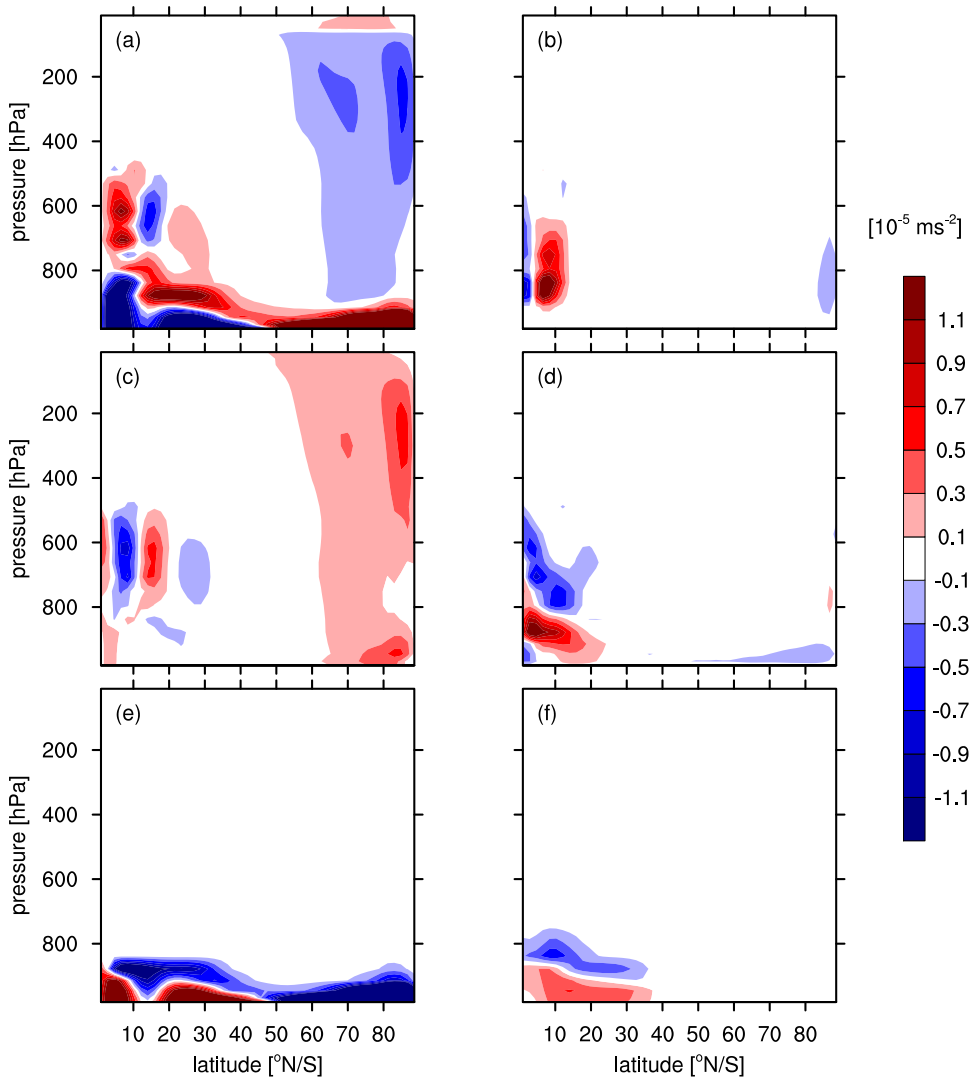

Figure 4.9: Terms of the mean zonal momentum budget in 10^{-5} ms^{-2} for suppressing vertical diffusion of zonal and meridional momentum and turbulent kinetic energy above 870 hPa (simulation U0V0T0): (a) mean meridional advection of mean absolute vorticity, (b) negative of mean flow vertical advection of mean zonal momentum, (c) horizontal contribution to eddy momentum flux convergence, (d) vertical contribution to eddy momentum flux convergence, (e) vertical diffusion, and (f) cumulus friction. The magnitude of the zonal momentum tendency due to horizontal diffusion is much smaller than $0.1 \cdot 10^{-5}$ ms^{-2} except close to the models' upper boundary and hence not included in this plot.

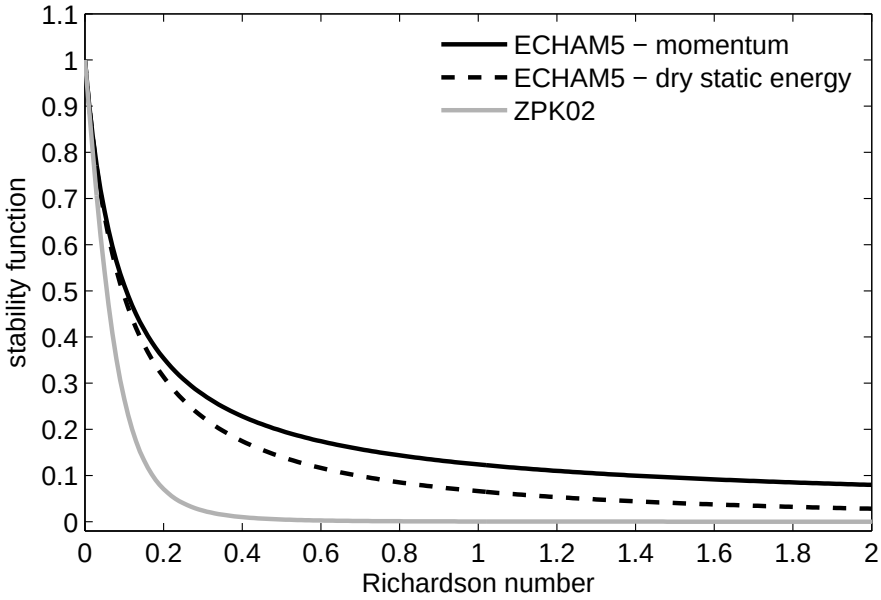

Figure 4.10: The Louis-type long-tail stability functions of the standard version of ECHAM5 (black for momentum, black dashed for dry static energy) and the newly implemented short-tail stability function that falls rapidly to zero above the critical Richardson number of 0.2 (ZPK02).

and a low level extension of the cell of about $5 \cdot 10^{10}$ kgs^{-1} to 45° N/S is always present, with a faint counterclockwise cell above. The Hadley cell strength does, however, depend on the diurnal cycle, whose inclusion effects a 50% increase compared to STD (see Table 4.2). For disabled diurnal cycle, choosing the short-tail stability function results in a slight weakening of the Hadley cell strength by 15%. In all simulations, vertical diffusion of meridional momentum decelerates the Hadley cell by downgradient momentum mixing between upper and lower branches as in STD though at decreased magnitude (not shown). For the zonal momentum balance, including the diurnal cycle (STD-DIUR) does little to the importance of vertical diffusion in the upper Hadley cell branch (Fig. 4.11). Using the short-tail stability functions with disabled diurnal cycle (SHORT) effects a reduction of vertical diffusion of zonal momentum in the upper Hadley cell branch. Enabling the diurnal cycle for the short-tail stability function (SHORT-DIUR), however, strengthens the influence of vertical diffusion of zonal momentum again. These simulations show that to correctly describe the zonal momentum balance in the upper branch of the Snowball Earth cell, one needs to account simultaneously for mean meridional advection of relative vorticity, eddy momentum fluxes and vertical diffusion, the latter appearing to be the dominant of these three terms below

Table 4.2: Summary of additional ECHAM5 simulations with enabled diurnal cycle (DIUR) in insolation and/or short-tail stability functions for stable and neutral conditions (SHORT). Hadley cell strength is measured by the absolute maximum of the mass stream function and given in units of 10^9 kgs^{-1}.

Simulation	diurnal cycle	stability functions	Hadley cell strength
STD-DIUR	on	ECHAM5	104
SHORT	off	ZPK02	66
SHORT-DIUR	on	ZPK02	103

the altitude of the maximum meridional wind.

For completeness, we note that switching on the diurnal cycle lowers the mean PBL depth as expected (not shown).

4.7 Discussion

We have found that in a state-of-the-art atmosphere general circulation model, vertical diffusion of momentum plays a major role for the dynamics of the Snowball Earth Hadley cell. When comparing this result with axisymmetric Hadley cell theories based on conservation of mean angular momentum (e.g., Held and Hou 1980; Caballero et al. 2008), this means that the latter are not applicable to a Snowball Earth atmosphere. In particular, the influence of vertical diffusion on the Hadley cell strength differs between our model and simulations with axisymmetric models. While suppressing vertical diffusion of momentum above 870 hPa in our model results in a doubling of the Hadley cell strength, axisymmetric simulations exhibit a weakening of the Hadley cell when viscosity is decreased (e.g., Held and Hou 1980; Kim and Lee 2001). This behaviour of axisymmetric models is in line with what one expects from the zonal momentum balance, but we have shown that vertical diffusion of meridional momentum is more important in setting the Hadley cell strength. Moreover, vertical eddies tend to compensate for the loss of vertical diffusion of zonal momentum. This compensation weakens the influence of vertical diffusion of zonal momentum on the Hadley cell strength, but is, of course, not possible in axisymmetric simulations. Concerning the structure of the tropical overturning circulation, the latter is subdivided into a weak deep cell and a much stronger tropospheric cell, similar to Caballero et al. (2008). However, the deep cell in our simulations does not conserve angular momentum.

Strong vertical momentum diffusion moreover means that the upper Snowball Earth Hadley cell branch is not, in contrast to the modern atmosphere, dominated by a

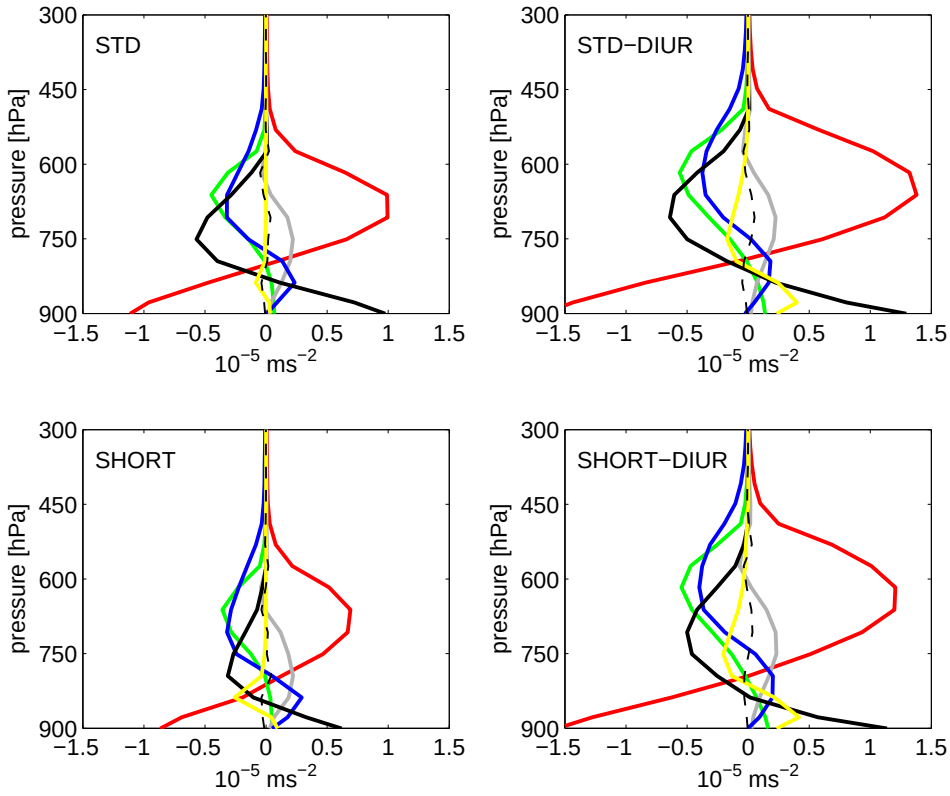

Figure 4.11: The zonal momentum balance averaged within 10° N/S for the standard simulation STD with disabled diurnal cycle (top left) and for simulations with enabled diurnal cycle (right column) and/or short-tail stability function (lower row). Simulation labels are according to Table 4.2. The color coding is as follows: red-mean Coriolis force, green-mean meridional advection of mean relative vorticity, gray-negative of mean vertical advection of mean zonal momentum, blue-eddy momentum flux convergence, black-vertical diffusion of zonal momentum, yellow-cumulus friction, black dashed-total sum.

balance between mean flow advection and eddy momentum fluxes. Since the Snowball Earth is an example of a dry atmosphere, this calls for reconsideration of the studies of dry Hadley cells with the idealized atmosphere general circulation model of Schneider and Walker (2006). This model has three features that distinguish it from our state-of-the-art atmospheric general circulation model. First, vertical diffusion of heat and momentum is restricted to the planetary boundary layer whose height is fixed to 2.5 km ($\simeq$ 850 hPa). Second, radiation is parameterized as Newtonian cooling towards a radiative equilibrium state that is statically unstable below 400 hPa (Schneider 2004). Third, convection is mimicked by relaxation towards a profile with lapse rate $\gamma\,\Gamma_d$,

where Γ_d denotes the dry adiabatic lapse rate (Walker and Schneider 2006). In the dry case $\gamma = 1$ relevant for Snowball Earth, the statically unstable radiative temperature profile suggests that dry convection in this model is active up to 400 hPa, but that it has no influence on momentum above 850 hPa. This is in fundamental contrast to our model, in which dry convection, modelled by vertical diffusion, acts on temperature and momentum. In the light of the importance of vertical diffusion on the Snowball Earth Hadley cell, the exclusion of convective momentum mixing in the idealized model appears too strong a simplification. This simplification does have a large effect on the Hadley cell strength and shape as shown by our simulations. The Hadley cell strength increases by about a factor of 2 when we suppress vertical diffusion of zonal and meridional momentum above 870 hPa but allow for vertical diffusion of dry static energy, similar to how dry convection works in the idealized model. In total, this casts doubts on the scaling laws for dry Hadley cells predicted by such an idealized model (Walker and Schneider 2006). We also note that observations of today's atmosphere have shown that the planetary boundary layer can reach several kilometers over deserts, leading to strong dry convection there (Gamo 1996).

The Snowball Earth atmosphere is very different from today's atmosphere because of its low temperatures and near-zero moisture content. This has two consequences. First, tropopause and boundary layer are maximally separated by 250 hPa in a Snowball Earth atmosphere and are hence much closer than today. The low tropopause is consistent with the low surface temperatures, while the comparably high boundary layer appears as a consequence of missing latent heat release. Second, the upper and lower branches of the Snowball Earth Hadley cell are not separated by a region of nearly vanishing meridional flow. This leads to strong meridional wind shear, making meridional momentum transfer between upper and lower branches possible. Our results therefore do not imply that vertical momentum diffusion is also of importance in today's atmosphere.

In optically thin atmospheres that are nearly transparent to solar radiation, longwave cooling destabilizes the troposphere (Pierrehumbert 2010). Because the effect of latent heat release is missing in dry atmospheres, the necessary stabilization can be achieved either by vertical diffusion or temperature advection. This implies that the intensity of vertical diffusion is intimately connected to the influence of the circulation on temperature. We have bypassed this issue here, but our results show that understanding the dynamics of dry Hadley cells requires not only to consider the horizontal momentum equation, but also the thermodynamic equation.

Our results have two important implications for building a Hadley cell theory. First, the strengthening of the Hadley cell with enabled diurnal cycle makes clear that the latter has to be included in the theory, at least in cases with low thermal inertia of the surface. We do not know of any Hadley cell model that accounts for the diurnal cycle. Second, the vital role of vertical diffusion for dry Hadley cells, requiring that dry

convection and boundary layer dynamics must be taken into account, points out that dry atmospheres in general should not be considered as a-priori simpler testcases for Hadley cell theories than moist atmospheres. Idealized atmospheric general circulation models that do not include momentum transfer by dry convection should not be viewed as models for dry atmospheres but as models that highlight the interaction of mean flow and eddies in the absence of subgrid-scale processes.

We have not analyzed the Snowball Earth Hadley cell extent in detail, partly because defining the latter seems ambiguous given the shape of the Hadley cell. Moreover, we have only studied equinox insolation. Repeating this study for solstice insolation might reveal that vertical momentum diffusion is of less importance when the heating is displaced from the equator, similar to what was found for the influence of eddies (Walker and Schneider 2005, 2006).

Despite the large differences in Hadley cell strength and shape among our set of simulations, equatorial surface temperature is close to 220 K in all simulations (Table 4.1). This suggests that the equatorial surface temperature is largely set by radiation in our idealized Snowball Earth atmosphere, with virtually no influence of the Hadley cell.

4.8 Conclusions

Using the state-of-the-art atmosphere general circulation model ECHAM5 to study the tropical circulation of an idealized Snowball Earth atmosphere subject to equinox insolation, we conclude the following

- The upper branch of the equinox Snowball Earth Hadley cell is strongly influenced by vertical momentum diffusion. This is in contrast to todays's atmosphere.
- Vertical diffusion of meridional momentum exhibits a stronger control on the Snowball Earth Hadley cell than vertical diffusion of zonal momentum.
- Neither axisymmetric Hadley cell models based on angular momentum conservation nor eddy-permitting Hadley cell models that neglect vertical diffusion of momentum are applicable to a Snowball Earth atmosphere since both assume an inviscid upper Hadley cell branch.
- Because vertical diffusion is important for a virtually dry Snowball Earth Hadley cell, dry atmospheres in general should not be considered as a-priori simpler testcases for Hadley cell theories than moist atmospheres.

Chapter 5

Conclusions and Outlook

5.1 Conclusions

I conclude my thesis by revisiting the research question brought up in the introduction.

1. Initiation of a Snowball Earth

- Is the location of continents important for Snowball Earth initiation?

Yes. I answer this question by comparing Snowball Earth initiation under present-day and Marinoan surface boundary conditions. The main difference between the two setups is the location of continents. I find that shifting continents from present-day location to low-latitudes while keeping the global mean background surface albedo fixed induces a global mean cooling of 4.6 K. Thus, the location of continents strongly influences the Snowball Earth bifurcation point (see next point). Low-latitude continents make Snowball Earth initiation easier, confirming the suggestion of Kirschvink (1992) and contradicting the findings of Poulsen et al. (2002).

- How much reduction of radiative forcing, in particular how much reduction of total solar irradiance (TSI), is needed to trigger Snowball Earth initiation? How much increase of atmospheric carbon dioxide is needed to prevent a Snowball Earth?

For present-day surface boundary conditions, I focus on the effect of decreasing TSI. I find that the critical TSI marking the Snowball Earth bifurcation point is between 91% and 94% of the present-day TSI for pre-industrial carbon dioxide. For Marinoan surface boundary conditions, I investigate the Snowball Earth bifurcation point with respect to TSI and atmospheric carbon dioxide. I demonstrate that the Snowball Earth bifurcation point for Marinoan surface boundary conditions is between 95.5% and 96% of the present-day TSI when carbon dioxide is at its pre-industrial concentration. Initiating a Marinoan Snowball Earth is therefore much easier than a modern Snowball

Earth. For TSI set to 94% of its present-day value, falling into a Snowball Earth is prevented by quadrupling atmospheric carbon dioxide with respect to its pre-industrial level. These results rebut previous conclusions that "extreme" forcings needed for Snowball Earth initiation render the Snowball Earth hypothesis implausible from the perspective of climate modelling.

- How does the climate system behave during the transition to a Snowball Earth, in particular how do atmosphere and ocean heat transports change?

The behaviour of atmosphere and ocean heat transports during the transition to a Snowball Earth depends on the location of continents. For present-day continents, the asymmetric distribution of continents between the Northern and Southern Hemispheres causes strong heat transports toward the more water-covered Southern Hemisphere as sea ice spreads towards the equator. The southern Hadley cell and the wind-driven subtropical ocean cells strengthen by a factor of 4 as sea ice approaches the equator. For Marinoan continents, which are distributed far more symmetrically between the Northern and Southern Hemispheres, meridional heat transport stay largely symmetric about the equator.

- How close can sea ice invade the tropics before global sea-ice cover is triggered?

Sea-ice cover above 56.5% is unstable for both present-day and Marinoan surface boundary conditions. This shows that independent of the location of the continents, ECHAM5/MPI-OM does not exhibit stable states with near-complete sea-ice cover but open equatorial waters. While my simulations do not provide evidence for the Slushball Earth hypothesis, they do not allow me to exclude their existence categorically. Simulations to investigate this issue are planned for the near future.

- Can we use simpler models to understand certain aspects of Snowball Earth initiation?

Yes. I back my answer on the example of the Snowball Earth bifurcation point and the transition times. I show that both are well reproduced by a zero-dimensional energy balance model of global mean ocean potential temperature. This is arguably the simplest climate model one could imagine for this problem.

2. Atmospheric dynamics of a Snowball Earth

- What characterizes the Hadley cell of a Snowball Earth atmosphere?

To ease comparison with theories, I focus on equinox insolation. I find that, in contrast to today's atmosphere, vertical momentum diffusion is an important process in the upper branch of a Snowball Earth Hadley cell. Consistent with thought experiments, suppressing vertical diffusion of zonal momentum effects a weakening of the Hadley cell whereas suppressing vertical diffusion of meridional momentum results in a strengthening of the Hadley cell. Combining both effect shows that vertical diffusion of meridional momentum exerts a stronger influence on the Snowball Earth Hadley cell strength than vertical diffusion of zonal momentum.

- How does this compare to dry Hadley cell theories?

I conclude that neither axisymmetric Hadley cell models based on angular momentum conservation nor eddy-permitting Hadley cell models that neglect vertical diffusion of momentum are applicable to a Snowball Earth atmosphere since both assume an inviscid upper Hadley cell branch. Because vertical diffusion is important for the Hadley cell of a Snowball Earth atmosphere, and because a Snowball Earth atmosphere is an example for a dry atmosphere, dry atmospheres in general should not be considered as a-priori simpler testcases for Hadley cell theories than moist atmospheres.

5.2 Outlook

In the end, I would like to propose two near-future modelling studies. The first targets the Snowball versus Slushball debate. While my simulations provide support for the Snowball Earth hypothesis, additional ECHAM5/MPI-OM simulations are needed to judge the compatibility of the Slushball Earth hypothesis with climate physics. The ultimate test of the Slushball Earth hypothesis would require to include interactive ice-sheets in our simulations. This would allow us to verify if tropical glaciers at sea-level form for some range of radiative forcing without triggering global sea-ice cover. However, this clearly represents a major modelling effort. A simpler modelling strategy that does not invoke interactive ice-sheets would be to prescribe all land as being glaciated, and to use ECHAM5/MPI-OM to test if tropical land temperatures below freezing are compatible with open equatorial oceans. If we find that this is not the case, this will provide strong evidence against the Slushball Earth hypothesis, and even more support for a Snowball Earth.

The second direction aims at the Hadley cell dynamics of dry atmospheres. I show that vertical diffusion of momentum is important for the Snowball Earth Hadley cell

under equinox insolation. Motivated by the work of Walker and Schneider (2005, 2006), who found that the influence of eddies on the Hadley cell depends on the latitude of the insolation maximum, I propose to repeat our study for solstice insolation. Moreover, the Snowball Earth atmosphere offers a straightforward testcase for dry atmospheres because its boundary conditions largely eliminate moisture from the atmosphere and therefore allowed me to apply a state-of-the art moist atmospheric general circulation model to study a dry atmosphere. In future studies, it might however turn out beneficial to transform the model into a dry model by manually switching off moist physics. This would allow us to investigate dry atmospheres beyond the range of the Snowball Earth framework.

Bibliography

Abbot, D. and I. Halevy, 2010: Dust Aerosol Important for Snowball Earth Deglaciation. *Journal of Climate*, accepted.

Abbot, D. S. and R. T. Pierrehumbert, 2010: Mudball: Surface dust and Snowball Earth deglaciation. *Journal of Geophysical Research*, **115**.

Arakawa, A. and V. R. Lamb, 1977: Computational design of the basic dynamical processes of the UCLA general circulation model. *Methods Comput. Phys.*, **17**, 173–265.

Baum, S. K. and T. J. Crowley, 2001: GCM response to late precambrian (similar to 590 Ma) ice-covered continents. *Geophysical Research Letters*, **28 (4)**, 583–586.

Bengtsson, L., K. I. Hodges, and E. Roeckner, 2006: Storm tracks and climate change. *Journal of Climate*, **19 (15)**, 3518–3543.

Berger, A. L., 1978: Long Term Variations of Daily Insolation and Quaternary Climatic Changes. *Journal of the Atmospheric Sciences*, **35 (12)**, 2362–2367.

Brasseur, G. P. and E. Roeckner, 2005: Impact of improved air quality on the future evolution of climate. *Geophysical Research Letters*, **32 (23)**, L23 704.

Bretagnon, P. and G. Francou, 1988: Planetary theories in rectangular and spherical variables - Vsop-87 solutions. *Astronomy and Astrophysics*, **202 (1-2)**, 309–315.

Brinkop, S. and E. Roeckner, 1995: Sensitivity of a general-circulation model to parameterizations of cloud-turbulence interactions in the atmospheric boundary layer. *Tellus Series A-Dynamic Meteorology and Oceanography*, **47 (2)**, 197–220.

Bronstein, I. N., 1996: *Teubner-Taschenbuch der Mathematik*. B. G. Teubner.

Budyko, M. I., 1969: Effect of solar radiation variations on climate of Earth. *Tellus*, **21 (5)**, 611–619.

Caballero, R., R. T. Pierrehumbert, and J. L. Mitchell, 2008: Axisymmetric, nearly inviscid circulations in non-condensing radiative-convective atmospheres. *Quarterly Journal of the Royal Meteorological Society*, **134 (634)**, 1269–1285.

Chandler, M. A. and L. E. Sohl, 2000: Climate forcings and the initiation of low-latitude ice sheets during the Neoproterozoic Varanger glacial interval. *Journal of Geophysical Research-Atmospheres*, **105 (D16)**, 20 737–20 756.

Crowley, T. J., W. T. Hyde, and W. R. Peltier, 2001: CO2 levels required for deglaciation of a "Near-Snowball" Earth. *Geophysical Research Letters*, **28 (2)**, 283–286.

Donnadieu, Y., Y. Godderis, G. Ramstein, A. Nedelec, and J. Meert, 2004a: A 'snowball Earth' climate triggered by continental break-up through changes in runoff. *Nature*, **428 (6980)**, 303–306.

Donnadieu, Y., G. Ramstein, F. Fluteau, D. Roche, and A. Ganopolski, 2004b: The impact of atmospheric and oceanic heat transports on the sea-ice-albedo instability during the Neoproterozoic. *Climate Dynamics*, **22 (2-3)**, 293–306.

Enderton, D. and J. Marshall, 2009: Controls on the total dynamical heat transport of the atmosphere and oceans. *to appear in Journal of Atmospheric Sciences*.

Evans, D. A. D., 2000: Stratigraphic, geochronological, and paleomagnetic constraints upon the Neoproterozoic climatic paradox. *American Journal of Science*, **300 (5)**, 347–433.

Ferreira, D., B. Rose, and J. Marshall, 2009: In preparation.

Fischer, N. and J. H. Jungclaus, 2010: Effects of orbital forcing on atmosphere and ocean heat transports in Holocene and Eemian climate simulations with a comprehensive Earth system model. *Climate of the Past*, **6 (2)**, 155–168.

Fortuin, J. P. F. and H. Kelder, 1998: An ozone climatology based on ozonesonde and satellite measurements. *Journal of Geophysical Research-Atmospheres*, **103 (D24)**, 31 709–31 734.

Fouquart, Y. and B. Bonnel, 1980: Computations of solar heating of the earth's atmosphere: A new parametrization. *Beitr. Phys. Atmos.*, **53**, 35–62.

Fraedrich, K., 1979: Catastrophes and Resilience of a zero-dimensional climate system with ice-albedo and greenhouse feedback. *Quarterly Journal of the Royal Meteorological Society*, **105 (443)**, 147–167.

Gamo, M., 1996: Thickness of the dry convection and large-scale subsidence above deserts. *Boundary-Layer Meteorology*, **79 (3)**, 265–278.

Gent, P. R., J. Willebrand, T. J. McDougall, and J. C. McWilliams, 1995: Parameterizing eddy-induced tracer transports in ocean circulation models. *Journal of Physical Oceanography*, **25 (4)**, 463–474.

Godderis, Y. and Y. Donnadieu, 2008: Carbon cycling and snowball Earth. *Nature*, **456 (7224)**.

Godderis, Y., et al., 2007: Coupled modeling of global carbon cycle and climate in the Neoproterozoic: links between Rodinia breakup and major glaciations. *Comptes Rendus Geoscience*, **339 (3-4)**, 212–222.

Goodman, J. C. and R. T. Pierrehumbert, 2003: Glacial flow of floating marine ice in "Snowball Earth". *Journal of Geophysical Research-Oceans*, **108 (C10)**, 3308.

Gough, D. O., 1981: Solar interior structure and luminosity variations. *Solar Physics*, **74 (1)**, 21–34, doi:10.1007/BF00151270.

Griffies, S. M., 1998: The Gent-McWilliams skew flux. *Journal of Physical Oceanography*, **28 (5)**, 831–841.

Hagemann, S., 2002: MPI-Report 336: An improved land surface parameter dataset for global and regional climate models. Tech. rep., Max Planck Institute for Meteorology, Hamburg, Germany.

Hagemann, S., B. Machenhauer, R. Jones, O. B. Christensen, M. Deque, D. Jacob, and P. L. Vidale, 2004: Evaluation of water and energy budgets in regional climate models applied over Europe. *Climate Dynamics*, **23 (5)**, 547–567.

Heinemann, M., J. H. Jungclaus, and J. Marotzke, 2009: Warm Paleocene/Eocene climate as simulated in ECHAM5/MPI-OM. *Climate of the Past*, **5 (3)**, 785–802.

Held, I. M., 2000: The general circulation of the atmosphere. *Proc. Prog. Geophys. Fluid. Dyn.*, Woods Hole, MA, USA, Woods Hole Oceanographic Institution, available under http://www.whoi.edu.

Held, I. M., 2001: The partitioning of the poleward energy transport between the tropical ocean and atmosphere. *Journal of the Atmospheric Sciences*, **58 (8)**, 943–948.

Held, I. M. and A. Y. Hou, 1980: Non-linear axially-symmetric circulations in a nearly inviscid atmosphere. *Journal of the Atmospheric Sciences*, **37 (3)**, 515–533.

Held, I. M. and M. J. Suarez, 1974: Simple albedo feedback models of ice-caps. *Tellus*, **26 (6)**, 613–629.

Hernandez-Deckers, D. and J. S. von Storch, 2010: Energetics responses to increases in greenhouse gas concentration. *Journal of Climate*, **(2010)**, doi: 10.1175%2F2010JCLI3176.1, in press.

Hibler, W. D., 1979: Dynamic thermodynamic sea ice model. *Journal of Physical Oceanography*, **9 (4)**, 815–846.

Hoffman, P. F., J. W. Crowley, D. T. Johnston, D. S. Jones, and D. P. Schrag, 2008: Snowball prevention questioned. *Nature*, **456 (7224)**.

Hoffman, P. F., A. J. Kaufman, G. P. Halverson, and D. P. Schrag, 1998: A Neoproterozoic snowball earth. *Science*, **281 (5381)**, 1342–1346.

Hoffman, P. F. and D. P. Schrag, 2002: The snowball Earth hypothesis: testing the limits of global change. *Terra Nova*, **14 (3)**, 129–155.

Holton, J. R., 2004: *An Introduction to Dynamical Meteorology*. Elsevier Academic Press.

Hyde, W. T., T. J. Crowley, S. K. Baum, and W. R. Peltier, 2000: Neoproterozoic 'snowball Earth' simulations with a coupled climate/ice-sheet model. *Nature*, **405 (6785)**, 425–429.

Jenkins, G. S. and L. A. Frakes, 1998: GCM sensitivity test using increased rotation rate, reduced solar forcing and orography to examine low latitude glaciation in the Neoproterozoic. *Geophysical Research Letters*, **25 (18)**, 3525–3528.

Jungclaus, J. H., et al., 2006: Ocean circulation and tropical variability in the coupled model ECHAM5/MPI-OM. *Journal of Climate*, **19 (16)**, 3952–3972.

Kaufman, A. J., 2007: Palaeoclimate: Slush find. *Nature*, **450 (7171)**, 807–808, doi: 10.1038/450807a.

Kerr, R. A., 2010: Snowball Earth has melted back to a profound wintry mix. *Science*, **327 (5970)**, 1186–, doi:10.1126/science.327.5970.1186.

Kim, H. K. and S. Lee, 2001: Hadley cell dynamics in a primitive equation model. Part I: Axisymmetric flow. *Journal of the Atmospheric Sciences*, **58 (19)**, 2845–2858.

Kirschvink, J. L., 1992: *The Proterozoic Biosphere*, chap. Late Proterozoic low-latitude global glaciation: The snowball Earth, 51–52. Cambridge University Press, New York.

Korty, R. L. and T. Schneider, 2008: Extent of Hadley circulations in dry atmospheres. *Geophysical Research Letters*, **35 (23)**, L23 803.

Landerer, F. W., J. H. Jungclaus, and J. Marotzke, 2007: Regional dynamic and steric sea level change in response to the IPCC-A1B scenario. *Journal of Physical Oceanography*, **37 (2)**, 296–312.

Le Hir, G., Y. Donnadieu, Y. Godderis, R. T. Pierrehumbert, G. R. Halverson, M. Macouin, A. Nedelec, and G. Ramstein, 2009: The snowball Earth aftermath: Exploring the limits of continental weathering processes. *Earth and Planetary Science Letters*, **277 (3-4)**, 453–463.

Le Hir, G., Y. Donnadieu, G. Krinner, and G. Ramstein, 2010: Toward the snowball earth deglaciation. *Climate Dynamics*, doi:10.1007/s00382-010-0748-8.

Le Hir, G., G. Ramstein, Y. Donnadieu, and R. T. Pierrehumbert, 2007: Investigating plausible mechanisms to trigger a deglaciation from a hard snowball Earth. *Comptes Rendus Geoscience*, **339 (3-4)**, 274–287.

Lewis, J. P., A. J. Weaver, and M. Eby, 2007: Snowball versus slushball Earth: Dynamic versus nondynamic sea ice? *Journal of Geophysical Research-Oceans*, **112 (C11)**, C11 014, doi:10.1029/2006JC004037.

Lewis, J. P., A. J. Weaver, S. T. Johnston, and M. Eby, 2003: Neoproterozoic "snowball Earth": Dynamic sea ice over a quiescent ocean. *Paleoceanography*, **18 (4)**, 1092.

Lin, S. J. and R. B. Rood, 1996: Multidimensional flux-form semi-Lagrangian transport schemes. *Monthly Weather Review*, **124 (9)**, 2046–2070.

Lohmann, U. and E. Roeckner, 1996: Design and performance of a new cloud microphysics scheme developed for the ECHAM general circulation model. *Climate Dynamics*, **12 (8)**, 557–572.

Lorenz, E. N., 1967: *The Nature and Theory of the General Circulation of the Atmosphere*. World Meteorological Organization.

Lott, F. and M. J. Miller, 1997: A new subgrid-scale orographic drag parametrization: Its formulation and testing. *Quarterly Journal of the Royal Meteorological Society*, **123 (537)**, 101–127.

Louis, J. F., 1979: Parametric model of vertical eddy fluxes in the atmosphere. *Boundary-Layer Meteorology*, **17 (2)**, 187–202.

Lubick, N., 2002: Palaeoclimatology: Snowball fights. *Nature*, **417 (6884)**, 12–13, doi:10.1038/417012a.

Luo, J. J., S. Masson, E. Roeckner, G. Madec, and T. Yamagata, 2005: Reducing climatology bias in an ocean-atmosphere CGCM with improved coupling physics. *Journal of Climate*, **18 (13)**, 2344–2360.

Macdonald, F. A., et al., 2010: Calibrating the Cryogenian. *Science*, **327 (5970)**, 1241–1243, doi:10.1126/science.1183325.

Marotzke, J. and M. Botzet, 2007: Present-day and ice-covered equilibrium states in a comprehensive climate model. *Geophysical Research Letters*, **34 (16)**, doi: 10.1029/2006GL028880.

Marshall, J., D. Ferreira, J. M. Campin, and D. Enderton, 2007: Mean climate and variability of the atmosphere and ocean on an aquaplanet. *Journal of the Atmospheric Sciences*, **64 (12)**, 4270–4286.

Marsland, S. J., H. Haak, J. H. Jungclaus, M. Latif, and F. Roske, 2003: The Max-Planck-Institute global ocean/sea ice model with orthogonal curvilinear coordinates. *Ocean Modelling*, **5 (2)**, 91–127.

Medeiros, B., A. Hall, and B. Stevens, 2005: What controls the mean depth of the PBL? *Journal of Climate*, **18 (16)**, 3157–3172.

Micheels, A. and M. Montenari, 2008: A snowball Earth versus a slushball Earth: Results from Neoproterozoic climate modeling sensitivity experiments. *Geosphere*, **4 (2)**, 401–410.

Mlawer, E. J., S. J. Taubman, P. D. Brown, M. J. Iacono, and S. A. Clough, 1997: Radiative transfer for inhomogeneous atmospheres: RRTM, a validated correlated-k model for the longwave. *Journal of Geophysical Research-Atmospheres*, **102 (D14)**, 16 663–16 682.

Myhre, G., E. J. Highwood, K. P. Shine, and F. Stordal, 1998: New estimates of radiative forcing due to well mixed greenhouse gases. *Geophysical Research Letters*, **25 (14)**, 2715–2718, doi:10.1029/98GL01908.

Neale, R. B. and B. J. Hoskins, 2000a: A standard test for AGCMs and their physical parameterizations. I: The proposal. *Atmos. Sci. Letters*, **1**, 101–107.

Neale, R. B. and B. J. Hoskins, 2000b: A standard test for AGCMs and their physical parameterizations. II: Results for The Met. Office Model. *Atmos. Sci. Letters*, **1**, 108–114.

Nordeng, T. E., 1994: Extended versions of the convective parametrization scheme at ECMWF and their impact on the mean and transient activity of the model in the tropics. Technical memorandum 206, ECMWF, Reading, UK.

North, G. R., 1975: Analytical Solution to a simple climate model with diffusive heat transport. *Journal of the Atmospheric Sciences*, **32 (7)**, 1301–1307.

Pacanowski, R. C. and S. G. H. Philander, 1981: Parameterization of vertical mixing in numerical models of tropical oceans. *Journal of Physical Oceanography*, **11 (11)**, 1443–1451.

Peixoto, J. P. and A. H. Oort, 1992: *Physics of Climate*. American Institute of Physics.

Peltier, W. R., 2003: Earth System History. *Encyclopedia of Global Environmental Change, Volume 1, The Earth System: Physical and Chemical Dimensions of Global Environmental Change*, M. C. MacCracken and J. S. Perry, Eds., John Wiley & Sons, 31–60.

Peltier, W. R. and Y. G. Liu, 2008: Carbon cycling and snowball Earth Reply. *Nature*, **456 (7224)**.

Peltier, W. R., Y. G. Liu, and J. W. Crowley, 2007: Snowball Earth prevention by dissolved organic carbon remineralization. *Nature*, **450 (7171)**, 813–U1.

Peltier, W. R., L. Tarasov, G. Vettoretti, and L. P. Solheim, 2004: Climate dynamics in deep time: Modeling the "Snowball bifurcation" and assessing the plausibility of its occurrence. *Extreme Proterozoic Geology, Geochemistry and Climate*, **146**, 107–124.

Pierrehumbert, R. T., 2002: The hydrologic cycle in deep-time climate problems. *Nature*, **419 (6903)**, 191–198.

Pierrehumbert, R. T., 2005: Climate dynamics of a hard snowball Earth. *Journal of Geophysical Research-Atmospheres*, **110 (D1)**, D01 111.

Pierrehumbert, R. T., 2010: *Planetary climates*. Cambridge University Press.

Pollard, D. and J. F. Kasting, 2005: Snowball Earth: A thin-ice solution with flowing sea glaciers. *Journal of Geophysical Research-Oceans*, **110 (C7)**, C07 010.

Poulsen, C. J., 2003: Absence of a runaway ice-albedo feedback in the Neoproterozoic. *Geology*, **31 (6)**, 473–476.

Poulsen, C. J. and R. L. Jacob, 2004: Factors that inhibit snowball Earth simulation. *Paleoceanography*, **19 (4)**, PA4021.

Poulsen, C. J., R. L. Jacob, R. T. Pierrehumbert, and T. T. Huynh, 2002: Testing paleogeographic controls on a Neoproterozoic snowball Earth. *Geophysical Research Letters*, **29 (11)**, 1515, doi:10.1029/2001GL014352.

Poulsen, C. J., R. T. Pierrehumbert, and R. L. Jacob, 2001: Impact of ocean dynamics on the simulation of the Neoproterozoic "snowball Earth". *Geophysical Research Letters*, **28 (8)**, 1575–1578.

Randall, D. A., J. A. Abeles, and T. G. Corsetti, 1985: Seasonal simulations of the planetary boundary layer and boundary layer stratocumulus clouds with a general circulation model. *Journal of the Atmospheric Sciences*, **42 (7)**, 641–676.

Raval, A. and V. Ramanathan, 1989: Observational determination of the greenhouse effect. *Nature*, **342 (6251)**, 758–761.

Roeckner, 2007: EH5-T31L19_MPIOM-GR3.0L40 PIcntrl. World Data Center for Climate. CERA-DB "EH5-T31L19_OM-GR3.0L40_CTL". http://cera-www.dkrz.de/WDCC/ui/Compact.jsp?acronym=EH5-T31L19_OM-GR3.0L40_CTL.

Roeckner, E., et al., 2003: The atmospheric general circulation model ECHAM5, part I: Model description. Tech. rep., Max Planck Institute for Meteorology, Hamburg, Germany.

Roeckner, E., et al., 2006: Sensitivity of simulated climate to horizontal and vertical resolution in the ECHAM5 atmosphere model. *Journal of Climate*, **19 (16)**, 3771–3791.

Romanova, V., G. Lohmann, and K. Grosfeld, 2006: Effect of land albedo, CO2, orography, and oceanic heat transport on extreme climates. *Climate of the Past*, **2 (1)**, 31–42.

Rose, B. E. J. and J. Marshall, 2009: Ocean heat transport, sea ice, and multiple climate states: insights from energy balance models. *accepted for publication in Journal of the Atmospheric Sciences*.

Rothman, D. H., J. M. Hayes, and R. E. Summons, 2003: Dynamics of the Neoproterozoic carbon cycle. *Proceedings of the National Academy of Sciences of the United States of America*, **100 (14)**, 8124–8129.

Savijarvi, H., 2009: Stable boundary layer: Parametrizations for local and larger scales. *Quarterly Journal of the Royal Meteorological Society*, **135 (641)**, 914–921.

Schneider, E. K., 1977: Axially-symmetric steady-state models of basic state for instability and climate studies. Part II. Nonlinear calculations. *Journal of the Atmospheric Sciences*, **34 (2)**, 280–296.

Schneider, T., 2004: The tropopause and the thermal stratification in the extratropics of a dry atmosphere. *Journal of the Atmospheric Sciences*, **61 (12)**, 1317–1340.

Schneider, T., 2006: The general circulation of the atmosphere. *Annual Review of Earth and Planetary Sciences*, **34**, 655–688.

Schneider, T. and C. C. Walker, 2006: Self-organization of atmospheric macroturbulence into critical states of weak nonlinear eddy-eddy interactions. *Journal of the Atmospheric Sciences*, **63 (6)**, 1569–1586.

Sellers, W. D., 1969: A global climate model based on the energy balance of the Earth-atmosphere system. *Journal of Applied Meteorology*, **8**, 392–400.

Semtner, A. J., 1976: Model for thermodynamic growth of sea ice in numerical investigations of climate. *Journal of Physical Oceanography*, **6 (3)**, 379–389.

Smith, R. S., C. Dubois, and J. Marotzke, 2006: Global climate and ocean circulation on an aquaplanet ocean-atmosphere general circulation model. *Journal of Climate*, **19 (18)**, 4719–4737.

Solomon, S., D. Qin, M. Manning, Z. Chen, M. Marquis, K. B. Averyt, T. M., and H. L. Miller, (Eds.) , 2007: *Contribution of Working Group I to the Fourth Assessment Report of the Intergovernmental Panel on Climate Change, 2007*. Cambridge Univ. Press, Cambridge, U. K.

Stone, P. H., 1978: Constraints on dynamical transports of energy on a spherical planet. *Dynamics of Atmospheres and Oceans*, **2 (2)**, 123–139.

Stone, P. H. and M. S. Yao, 2004: The ice-covered Earth instability in a model of intermediate complexity. *Climate Dynamics*, **22 (8)**, 815–822.

Tanré, D., J. F. Geleyn, and J. Slingo, 1984: *First results of the introduction of an advanced aerosol-radiation interaction in ECMWF low resolution global model*, 133–177. Deepak Publishing, Hampton, VA.

Tiedtke, M., 1989: A comprehensive mass flux scheme for cumulus parameterization in large-scale models. *Monthly Weather Review*, **117 (8)**, 1779–1800.

Trindade, R. I. F. and M. Macouin, 2007: Palaeolatitude of glacial deposits and palaeogeography of Neoproterozoic ice ages. *Comptes Rendus Geoscience*, **339 (3-4)**, 200–211.

Valcke, S., A. Caubel, D. Declat, and L. Terray, 2003: OASIS Ocean Atmosphere Sea Ice Soil users's guide. Tech. rep., CERFACS Tech. Rep. TR/CMGC/03/69, Toulouse, France, 85 pp.

Vallis, G. K., 2006: *Atmosphericv and Oceanic Fluid Dynamics*. Cambridge University Press.

Voigt, A. and J. Marotzke, 2009: The transition from the present-day climate to a modern Snowball Earth. *Climate Dynamics*, doi:10.1007/s00382-009-0633-5.

Walker, C. C. and T. Schneider, 2005: Response of idealized Hadley circulations to seasonally varying heating. *Geophysical Research Letters*, **32 (6)**, L06 813.

Walker, C. C. and T. Schneider, 2006: Eddy influences on Hadley circulations: Simulations with an idealized GCM. *Journal of The Atmospheric Sciences*, **63 (12)**, 3333–3350.

Walsh, K. J. and W. D. Sellers, 1993: Response of a global climate model to a 30 percent reduction of the solar constant. *Global and Planetary Change*, **8 (4)**, 219–230.

Washington, W. M. and C. L. Parkinson, 2005: *An Introduction to Three-Dimensional Climate Modeling*. 2d ed., University Science Books.

Wild, M. and E. Roeckner, 2006: Radiative fluxes in the ECHAM5 general circulation model. *Journal of Climate*, **19 (16)**, 3792–3809.

Wolff, J. O., E. Maier-Reimer, and S. Legutke, 1997: The Hamburg Ocean Primitive Equation Model HOPE. Tech. Rep. 13. Tech. rep., German Climate Computer Center (DKRZ), Hamburg, Germany.

Zilitinkevich, S. S., V. L. Perov, and J. C. King, 2002: Near-surface turbulent fluxes in stable stratification: Calculation techniques for use in general-circulation models. *Quarterly Journal of the Royal Meteorological Society*, **128 (583)**, 1571–1587.

Acknowledgements

First and foremost, I wish to thank Prof. Dr. Jochem Marotzke for being an excellent supervisor. He granted scientific freedom as much as possible but pulled me back on track whenever I needed it. I especially thank him for teaching me how to think simple to understand the complex, and for opening doors that would otherwise have remained closed. I would like to thank my co-advisor Dr. Erich Roeckner for numerous discussions and help with ECHAM5. Thanks to Prof. Dr. Hans von Storch for chairing my panel and for driving me to focus my floating thoughts.

I would like to thank the IMPRS-ESM for providing an outstanding PhD environment. Special thanks to Dr. Antje Weitz and Cornelia Kampmann for their organisational and mental support. I also thank the ZEIT Foundation Ebelin and Gerd Bucerius for funding the IMPRS-ESM Guest and Exchange Program, which made the visit of Dr. Dorian Abbot to Hamburg possible, as well as several trips of my own. Thanks to the German Climate Computing Centre (DKRZ), and to the Central IT Services for their technical support. I thank the library staff for getting hold of whatever books I needed, and for keeping track of the drum room key.

I would like to express my gratitude to Prof. Dr. Issac M. Held for first-hand insight into the world of Hadley cells and his kind hospitality during my stay at GFDL. This paved my way into atmospheric dynamics. I wish to thank Dr. Dorian S. Abbot and Prof. Dr. Raymond T. Pierrehumbert for providing the Marinoan reconstruction and innumerous advice on the Marinoan Snowball Earth simulations. I would also like to thank Dr. Thorsten Mauritsen for suggesting the short-tail stability function, and Prof. Dr. Bjorn Stevens for help with setting up the 62-level ECHAM5 grid. Many thanks go to Michael Botzet and Dr. Helmuth Haak for help with running and analyzing the coupled model and their interest in my work. I thank the ocean group and the MPI-M in general for creating a supporting and productive atmosphere.

Thanks especially to Ilka Wantia, Dr. Malte Heinemann, Nils Fischer, Florian Rauser, Fanny Adloff, Steffen Tietsche, Mario Krapp, Ronny Petrik, Maria Paz Chidichimo,

Acknowledgements

Daniel Hernandez-Deckers, Freja Vamborg, Juliane Otto, Werner Bauer, Rosina Grimm, Jaison Ambadan, and Peter Düben for cheering me up, making me feel comfortable in Hamburg, and for braving tired jokes.

There is little more to say, but this little is so all-embracing, Gabriela, that I lacked the words until I remembered these.

I never planned in my imagination a situation so heavenly
A fairy land where no one else could enter
And in the center just you and me
My heart beat like a hammer
My arms wound around you tight
And stars fell on Taiga last night.

Die gesamten Veröffentlichungen in der Publikationsreihe des MPI-M
„Berichte zur Erdsystemforschung“,
„Reports on Earth System Science“,
ISSN 1614-1199

sind über die Internetseiten des Max-Planck-Instituts für Meteorologie erhältlich:

http://www.mpimet.mpg.de/wissenschaft/publikationen.html



ISSN 1614-1199